Elastic Scattering Of Protons From ^{40}Ca, ^{42}Ca and ^{44}Ca In The Energy Range 20 - 50 MeV, and Nuclear Matter Radii

By

Tawfik N. Nasr

A Thesis Submitted To

The Faculty of Graduate Studies

University of Manitoba

In Partial Fulfilment

Of The Requirements For The Degree

Doctor of Philosophy

June 1980

ELASTIC SCATTERING OF PROTONS FROM ^{40}Ca, ^{42}Ca AND ^{44}Ca IN THE ENERGY RANGE 20 - 50 MeV, AND NUCLEAR MATTER RADII

BY

TAWFIK NOAMAN NASR

A thesis submitted to the Faculty of Graduate Studies of the University of Manitoba in partial fulfillment of the requirements of the degree of

DOCTOR OF PHILOSOPHY

ABSTRACT

Measurements of proton elastic scattering differential cross sections have been made for the ^{40}Ca, ^{42}Ca and ^{44}Ca isotopic sequence at mean incident energies of 21.0, 25.0, 30.0, 35.0, 40.0, 45.0 and 48.4 MeV. The angular distributions cover the range 10^{o} - 170^{o} (in the laboratory) in 2.5^{o} steps at forward angles and 5^{o} steps at backward angles. The differential cross sections have relative errors of about 3.0% while the scale errors are less than 2.5%. The data have been analyzed in terms of a standard optical potential with an explicit ℓ-dependent term. Differences between the r.m.s. radii of the neutron and proton distributions have been deduced and are compared with the results of previous measurements and with various theoretical predictions. In general there is good agreement between the present results and those obtained in analyses of intermediate energy proton and alpha elastic scattering data. The Coulomb displacement energies yield smaller values while pionic atom data yield larger values than those obtained from hadronic scattering data. The predictions of Hartree-Fock calculations are in satisfactory agreement with the hadronic scattering results results whereas the shell-model predictions are too large.

ACKNOWLEDGEMENTS

I owe a special debt of gratitude to my advisor, Dr. W.T.H. van Oers, whose encouragement, guidance and sound advice were especially welcomed. His active participation in all aspects of the experiment has been a major factor in its success. His broad knowledge of nuclear physics was invaluable during the years I worked with him.

I am also indebted to Dr. J. Birchall, Dr. R.H. McCamis and Mr. P.J.T. Verheijen for their help during the experiments and their assistance in collecting the data.

I wish to acknowledge the vital assistance of Mr. D.K. Hasell by providing me with computer programs for spectra analysis. His willingness to assist at any time is greatly appreciated. The technical support of the cyclotron staff and the cooperation of the University of Manitoba Computer facility were essential during the running of this experiment.

The patience, understanding and continuous encouragement of my wife, Tahany, during all stages of this work has not gone unnoticed and cannot be sufficiently rewarded.

Finally, the financial support of the Natural Sciences and Engineering Research Council of Canada and the University of Manitoba is greatly appreciated.

CONTENTS

INTRODUCTION

The determination of nuclear sizes is one of the important problems of nuclear physics. The extent to which we are able to give precise and meaningful statements about nuclear matter and charge distributions reveals the state of our understanding of much more fundamental issues, such as the nature of the interaction between various types of particles and the role of these interactions in scattering phenomena.

It was suggested by Guth[1] in 1934 that, for fast electrons, the finite size of the nuclear charge distribution would produce large deviations from the cross section for scattering from a point charge. About twenty years after Guth's suggestion, the first attempt to determine nuclear charge radii from electron scattering measurements was made by Lyman et al.[2].

The electromagnetic and weak interactions of muons have been shown, to very great accuracy, to be identical to those of electrons, so that there are many similarities between the energy levels of muonic and 'electronic atoms'. Fitch et al.[3], performed an experiment in which negative muons were stopped in matter to form atoms. The size of the orbits of muonic atoms is reduced by the factor ($m_\mu/m_e \approx 207$) relative to ordinary (electronic) atoms so that the muonic orbits can overlap with the tail of the nuclear matter distribution. Measurements of the energies of muonic atom x-rays provide another means of determining nuclear charge distributions and radii.

Another, older method exists for the determination of differences between the nuclear charge radii for different isotopes of an element. This comes from measuring the isotopic shift of spectral lines in ordinary atoms. The term "isotopic shift" is used to denote the change in the energy of a given atomic transition when one or more neutrons are added to the nucleus. A similar shift called the isomer shift gives the change in the charge radius

when a long lived nuclear state is excited.

Although nuclear charge radii are obtained to high accuracy from electron scattering and transitions of muonic atoms, it is much more difficult to determine the nuclear matter radii, since the strong interaction is not as well understood as the electromagnetic interaction. However methods have been developed for the determination of nuclear matter radii. Then, if the charge radii are known, it is easy to obtain the point neutron and proton radii. One of the most direct methods involves proton elastic scattering and the use of an optical potential or a multiple scattering formalism that describes the scattering of nucleons by nuclei.

Proton elastic scattering data in the intermediate energy region (> 300 MeV) can be, analyzed in the framework of the Glauber multiple-scattering theory[4]. The physical interpretation of this theory is that the projectile makes succesive scatterings from **different** nucleons inside the nucleus and propagates freely between them. It should be pointed out that the scattering from a nucleon in the nucleus differs from the scattering from free nucleons in a number of respects owing to the presence of the other nucleons. For example, in the nucleus the exclusion principle acts to block a number of energetically available scattering states.

Another approach in the analysis of the intermediate energy proton elastic scattering data is to make use of the spin-dependent proton-nucleus microscopic optical potential approach of Kerman, MacManus and Thaler[5] (KMT) where the point nucleon densities are determined by fitting proton-nucleus elastic scattering differential cross section and analyzing power angular distributions. The spin-dependent nucleon-nucleon amplitudes are determined by analyzing nucleon-nucleon elastic scattering data.

It should be mentioned that throughout this thesis several radii which

are associated with various distributions in the nucleus are discussed. These are the radii of the charge, proton, neutron, nuclear matter and nuclear potential distributions. The two directly measurable radii are those of the charge and the nuclear potential, measured by means of electromagnetic and hadronic probes, respectively. If one takes the proton distribution to be that of point particles, the proton radius is obtained from the charge radius by subtraction of the finite size of the proton charge distribution. In a similar fashion, the nuclear matter radius can be determined from the proton-nucleus potential radius by subtraction of the proton-nucleon interaction radius. Since the nuclear matter distribution is the sum of the proton and neutron distributions, the neutron radius can thus be determined from the nuclear matter and proton radii.

In this thesis our ultimate aim is to study the reliability of the extraction of nuclear size information from optical model analyses of low energy proton elastic scattering data. To achieve this goal an experiment was performed using the proton beam from the University of Manitoba spiral-ridge cyclotron. Measurements were made of the proton elastic scattering differential cross section angular distributions for the ^{40}Ca, ^{42}Ca, ^{44}Ca isotopic sequence. The differential cross section angular distributions cover the range 10° to 170° in the laboratory in 2.5° steps in the forward hemisphere and 5° steps in the backward hemisphere at mean proton energies of 21.0, 25.0, 30.0, 35.0, 40.0, 45.0 and 48.4 MeV for ^{42}Ca and ^{44}Ca and of 25.0, 27.5, 30.0, 35.0, 40.0, and 45.0 MeV for ^{40}Ca. The measured differential cross sections in conjunction with analyzing power data available from the literature and the ^{40}Ca differential cross sections measured by van Oers et al.[6] at 21.0, 23.5, 26.3 and 48.0 MeV were analyzed using a standard optical model potential with an explicit ℓ-dependent term.

The calcium isotopic sequence is very interesting to study, since it offers a wide range of neutron number. In addition, there exists a large body of intermediate energy p-Ca elastic scattering data[7] as well as α-Ca elastic scattering data[8]. Furthermore, one can study the effect on the root mean square (r.m.s.) radius associated with the addition of neutron pairs in the $1f_{7/2}$ shell.

The first chapter in this thesis is a review of electromagnetic methods for nuclear charge radius determinations. Advantages and disadvantages of each method are discussed.

The second chapter gives a general description of the optical model potential and a discussion of the extraction of the nuclear matter radius from the optical potential radius.

Chapter three describes the experimental arrangements and procedures for measuring the differential cross section angular distributions.

The final chapter is divided into three sections. The first section is the reduction of the experimental data and the uncertainties associated with the experimental measurements. The second section is a description of the optical model analysis performed. The last section is a discussion of the results obtained, a comparison with other measurements and some concluding remarks. Finally, tables of the measured differential cross-sections are given in Appendix 1.

CHAPTER I

Electromagnetic Methods for the Determination of Nuclear Charge Distributions

I-1 Electron Scattering

Elastic scattering of fast electrons by nuclei is the most successful method for investigation of the charge distribution in nuclei since the electron is the best understood of all the elementary particles and the theory of its interactions with other particles is well established.

To be able to detect finite nuclear size effects it is necessary that the reduced de Broglie wavelength of the electron should be comparable with the size of the nucleus. We thus expect to begin to observe finite size effects in heavy nuclei at about 20 MeV and details of the charge distribution at about 100 MeV.

In the theory of the first Born approximation the differential electron scattering cross section is given in terms of the form factor F(q) by:

$$\left(\frac{d\sigma}{d\Omega}\right) = \left(\frac{d\sigma}{d\Omega}\right)_o |F(q)|^2 \qquad (1)$$

where $\left(\frac{d\sigma}{d\Omega}\right)_o$ is the cross section for scattering from a point nucleus and the form factor F(q), generally, consists of two components, one, $F_{ch}(q)$, caused by the nuclear charge distribution and the other, $F_M(q)$, caused by the magnetic moment of the nucleons. In principal the magnetic scattering can be separated from the charge scattering by a 180^o - scattering technique. The form factor $F_{ch}(q)$ is given by

$$F_{ch}(q) = \frac{4\pi}{q} \int_0^\infty \sin(qr)\ \rho(r)\ r\ dr \qquad (2)$$

where q is the momentum transferred to the nucleus and $\rho(r)$ is the nuclear charge distribution. $\rho(r)$ is determined by assuming a particular form for it,

and then varying its parameters until the calculated cross sections fit the experimental values.

It is seen from equation (2) that $qF_{ch}(q)$ is essentially the Fourier sine transform of $r\,\rho(r)$, so that the determination of $\rho(r)$ requires one to know $F_{ch}(q)$ for all q, i.e. the scattering cross section must be known for all energies and angles. However experimental considerations restrict our knowledge of $F_{ch}(q)$ when q is very small or very large, and consequently very little is known about $\rho(r)$ for very small or very large r[9].

If the electrons traverse the outer regions of the nucleus they are scattered effectively by the whole charge and the cross section is nearly the same as for Coulomb scattering. Further, they are scattered through small angles only. As the cross section in this case is large, small differences from pure Coulomb scattering are very difficult to detect. Conversely, electrons that probe the very center of the nucleus have to be highly energetic and are scattered through large angles. Cross sections are then very small and difficult to measure accurately.

It should be mentioned that the first Born approximation has been successful in determining the charge distribution for light nuclei. For intermediate and heavy weight nuclei the Dirac equation must be solved in order to accurately determine the nuclear charge distribution.

Frosch et al.[10] carried out an electron scattering experiment at 250 and 500 MeV to determine the charge distribution in the calcium isotopes. A phenomenological analysis of the data was performed using a three parameter charge distribution of the form

$$\rho(r) = \rho_o\left[1 + w\left(\frac{r}{c}\right)^2\right]\left[1 + \exp\left(\frac{r-c}{z}\right)\right]^{-1}$$

where the three adjustable parameters w, c and z are determined by fitting the experimental data. The parameters they obtained from the analysis are shown

in Table 1.

Table 1: Electron Scattering Parameters[10)]

Nucleus	C (fm)	Z (fm)	W	$\langle r^2 \rangle^{1/2}$ (fm)
^{40}Ca	3.68	0.59	-0.10	3.49
^{42}Ca	3.73	0.59	-0.12	3.52
^{44}Ca	3.75	0.57	-0.09	3.51
^{48}Ca	3.74	0.53	-0.03	3.48

where $\langle r^2 \rangle^{1/2}$ is the r.m.s. radius of the charge distribution. The uncertainty in the measured $\langle r^2 \rangle^{1/2}$ is claimed to be 1%. The energy range of electron scattering experiments is above the region in which appreciable deflections or energy losses are caused by collisions with the atomic electrons. Radiative and dispersion corrections (due to the emission of real photons and the emission and absorption of virtual photons by the electrons), multiple small-angle scattering (which results in a straggling correction) and vacuum polarization effects (due to the presence of virtual electron-positron pairs) are normally taken into account when analyzing electron scattering experiments.

I-2 Mu-Mesonic Atoms

The μ-meson is a better test particle than the electron because of its much greater mass ($m_\mu \approx 207\ m_e$). It has the same charge as the electron and its interaction with nuclear matter is entirely electromagnetic[11)]. Negative muons are obtained from the decay in flight of pions produced, for instance, in a Be target bombarded by an intermediate energy proton beam. The muon beam is transported to the target where the muons are captured. The muons lose most of their energy by collisions with the electrons and their energy reaches a value of 2 keV in a period of 10^{-9} sec. after the muons are stopped in the target. They are then captured into higher order Bohr orbits, from which they

cascade into lower orbits by means of radiative transitions[12]. It takes approximately 10^{-13} sec. to reach the orbit closest to the nucleus. This time is very short compared to the muon natural life time of 2.2 μsec. The radii of these Bohr orbits are about 207 times smaller than the corresponding electron orbits, and so the binding energy of the 1S level is very sensitive to the nuclear charge distribution. Higher levels are not significantly affected and thus the shift in the 1S level from its calculated position for a point nucleus to that found experimentally gives a measure of the nuclear size. This shift is determined by measurement of the energy of the x-ray emitted when the muon makes its final $2P_{3/2} - 1S_{1/2}$ transition to the ground state. In a heavier nucleus such as lead the muon in its lowest state is estimated to spend about half of its time inside the nucleus. In this case the shift in the 2P level is considered when the muon makes the 3d - 2P transition. Difficulties with this method arise for light nuclei, ($Z < 6$) where the shift of the 1S level is too small to be measured with great precision. The uncertainties in the deduced $< r^2 >^{1/2}$ for light nuclei are therefore considerable. Radiative corrections for muonic atoms are similar to those described for electron scattering. The unobserved monopole excitation of the nucleus makes it difficult to account for nuclear polarization corrections in muonic atoms. The uncertainties in this correction limit the accuracy with which one can obtain accurate information from transitions in muonic atoms.

Wohlfahrt et al.[13] measured the muonic transitions in the calcium isotopes. In their analysis of the data, as a convenient form of the charge distribution a two parameter Fermi distribution given by

$$\rho(r) = \rho_o[1 + \exp \frac{r-c}{a}]^{-1}$$

was used. The parameter a was fixed at 0.55 fm and the half-density radius, c, of the Fermi distribution adjusted to reproduce the experimental transition

energies. The parameters obtained are listed in Table 2.

Table 2: Muonic Atom Parameters[13]

Isotope	C (fm)	$< r^2 >^{1/2}$ (fm)
^{40}Ca	3.636	3.480
^{42}Ca	3.684	3.510
^{44}Ca	3.699	3.520
^{48}Ca	3.637	3.481

The uncertainty in $< r^2 >^{1/2}$ is about 0.6%.

I.3 Coulomb Energy Differences

The study of Coulomb energy differences of mirror nuclei (pairs of isobars where one member of the pair has Z protons and N neutrons and the other has N protons and Z neutrons) has been regarded as a source of information about nuclear sizes. The repulsive electrostatic forces between protons are responsible for a potential energy, E_c, which reduces the nuclear binding energy. The difference ΔE_c in Coulomb energy for mirror nuclei with charges Ze and (Z-1)e has been calculated[14] taking into account the uncertainty in the position of the proton with the charge of each proton effectively distributed over a small region of space. The result is

$$\Delta E_c = 2e^2 \, J[(Z - \tfrac{1}{2}) - \tfrac{2}{3}^{2/3} \, (Z - \tfrac{1}{2})^{1/3} \, K] \qquad (3)$$

where,

$$J = \frac{4\pi}{2(Ze)} \int_0^\infty \rho(r) \, V(r) \, r^2 \, dr \; ;$$

$\rho(r)$ is the nuclear charge density,

$$V(r) = Ze \int_r^\infty \frac{dr}{r^2} \int_0^r \rho(r') \, r'^2 \, dr'$$

and K is a constant whose exact value depends on the form of $\rho(r)$ and the geometrical shape of the charge on each proton.

The nucleus with a larger Coulomb energy in a pair of mirror nuclei decays via e^+ emission to the other member of the pair. If one assumes that the nuclear forces are the same between any pair of nucleons, then the difference in the binding energies of the two mirror nuclei is equal to the difference in their Coulomb energies, $\Delta E_c = (M_n - M_p + 2m_e)c^2 + T(e^+)$, where M_n, M_p and m_e are the neutron, proton and electron mass, respectively. As the kinetic energy $T(e^+)$ of the emitted positron can be measured with a considerable accuracy, the Coulomb energy difference can be determined experimentally. The data can be fitted with equation (3) to obtain J and K and thus nuclear radii can be extracted.

A variation of the Coulomb energy difference in mirror nuclei has been considered by Nolen, Schiffer and Williams[15]. They considered the energy difference between the parent state in the nucleus (Z,N) and the isobaric analogue state in the nucleus (Z + 1, N - 1). The basic assumption in the method is that the distribution of the extra proton in the isobaric analogue state ($\rho_p(r)$) is the same as the distribution ρ_{ne} of the excess N-Z neutrons in the parent state, which is given by

$$\rho_{ne} = N \ \rho_n(r) - Z \ \rho_{nc}(r) \qquad (4)$$

where $\rho_n(r)$ is the total neutron distribution in the parent nucleus and $\rho_{nc}(r)$ is the distribution of the core of Z neutrons. The principal contribution to the energy is then given by the interaction of the extra proton in the analogue state with the Coulomb potential due to the core of Z protons. This may be written as

$$\Delta E_c = 4\pi e \int_0^\infty \rho_p(r) \ V(r) \ r^2 \ dr \ . \qquad (5)$$

There are a number of corrections to ΔE_c arising from exchange effects due to anti-symmetrization of the nuclear wave function and from the electromagnetic spin-orbit interaction. A Fermi charge distribution determined by electron scattering experiments is used to construct the Coulomb potential, V(r), in equation (5). A Fermi distribution is assumed for ρ_{ne}, which is the same as $\rho_p(r)$ in equation (5), and its parameters are varied until the experimental value of the Coulomb energy difference is obtained. Knowing ρ_{ne}, ρ_n can be obtained from equation (4). It was found that the experimental Coulomb energy data could be reproduced only when the r.m.s. radius of the neutron excess distribution was taken only slightly larger than that of the distribution of the core. In the single-particle model, this implies that the radii of Fermi potentials which yield the required ρ_{ne} to fit the Coulomb energy differences are 10 - 20% smaller than those required to give proton distributions in agreement with electron scattering data. Alternatively, if the same Fermi potentials are used to generate both $\rho_p(r)$ and $\rho_{ne}(r)$, the calculated Coulomb energy differences are about 7% too small. This anomaly is referred at as the Nolen and Schiffer anomaly.

With this method Nolen et al.[15] obtained for the difference between the r.m.s. radii of the neutron and proton distributions, $\Delta r_{np} = \langle r_n^2 \rangle^{1/2} - \langle r_p^2 \rangle^{1/2}$ the values 0.01, 0.02 and 0.06 fm for ^{42}Ca, ^{44}Ca and ^{48}Ca, respectively.

I.4 The α-Decay Method

In α scattering experiments, deviation from the Coulomb scattering law $V(r) = \frac{ZZ'e^2}{r}$, occurs when the incident particles begin to feel the nuclear potential. Similarly, in α-decay the particle attempting to escape from the nucleus feels a Coulomb barrier, this time from the inside. Because of this barrier the α particle is repeatedly reflected back and forth within the nucleus.

According to quantum mechanics the probability p that the α particle will tunnel through the Coulomb barrier and be emitted from the nucleus is given according to the WKB approximation by[16)]

$$p \simeq \exp\left[-\frac{2}{\hbar}\int_{R}^{\frac{zZe^2}{T}} \sqrt{2M\left(\frac{zZe^2}{r} - T\right)}\, dr\right] \qquad (6)$$

where Z and z are the charge of the daughter nucleus and the α particle, respectively, M is the reduced mass of the daughter nucleus and the α particle and T is the energy of the emitted α particle. P can be written as

$$p = \lambda/f$$

where f is the frequency of collision of the α particle with the barrier ($f = \frac{v}{2R}$, where v is the velocity of the α particle inside the nucleus), and λ is the decay constant. Therefore, equation (6) can be written as

$$\lambda = \frac{v}{2R} \exp\left[\frac{-2}{\hbar^2}\int_{R}^{\frac{zZe^2}{T}} \sqrt{2M\left(\frac{zZe^2}{r} - T\right)}\, dr\right]$$

or

$$\ell n\, \lambda = \ell n \frac{v}{R} + 2.97\,(Z-2)^{1/2} R^{1/2} - 3.95\,(Z-2)\, T^{-1/2} \qquad (7)$$

The velocity v is assumed equal to the velocity of the emitted α-particle, $\sqrt{2mT}$. The quantities λ, v and T can be determined experimentally for an α emitter and the nuclear radius, R, can be determined by fitting equation (7) to the experimental results.

Kaplan[17)] determined R for a range of heavy, even-even nuclei by fitting the disintegration constants using the measured α-particle energies. He found an average value for the sharp cut-off radius given by

$$r_o = R\, A^{-1/3} = 1.570 \pm 0.015 \text{ fm},$$

where A is the mass number of the residual nucleus.

This method is of limited use in the determination of nuclear radii since it is applicable only to alpha-emitters.

In summary, the discussion in the preceding chapter has indicated that in most cases information about the charge distribution is obtained in an indirect way, namely by assuming a particular form of the distribution and then calculating the scattering cross section or atomic spectrum for comparison with experiment. At present, one has most confidence in the electron scattering results and in general these are the results used in the analysis of intermediate energy proton and alpha particle scattering data for the calcium isotopes when attempting to learn something about the neutron distributions.

CHAPTER II

The Determination of Nuclear Matter Radii

II.1 The Optical Model

It is at present impractical to deal with the nucleon-nucleus interaction in detail in the low-energy region by summing the nucleon-nucleon interactions, since one is faced with unresolved mathematical difficulties treating the complex many body problem.

One tries to reduce the many body problem to a two body problem by replacing the various interactions between the incident particle and the target nucleus by a phenomenological effective potential. The effective potential should account for elastic scattering and other possible reactions. This is satisfied if the potential is complex. The imaginary part of this potential accounts for absorptions (inelastic scattering and reactions) allowed by the Pauli principle and the law of conservation of energy. This complex potential is referred to as the optical potential because of the analogy of the elastic and inelastic interaction between nucleons and nuclei with the reflection and absorption of light by a medium with a complex refractive index.

About twenty five years ago, a square well potential was used for simplicity[18]. However it was found that this potential does not predict well the experimentally measured elastic scattering differential cross sections, and the total reaction cross sections predicted from this potential were found to be always too small compared with the measured values. It was thought that the potential should not have a sharp cut off but should go to zero gradually. A revised form of the optical potential was introduced by Woods and Saxon[19]. Its form is the same as a Fermi distribution used in electron scattering, and it has been generally used since then.

The optical model potential can be written as

$$U(r) = -V f(x_o) - iW f(x_I) \qquad (8)$$

where V and W are the depth of the real and imaginary parts respectively, $x_i = \frac{r - r_i A^{1/3}}{a_i}$, $f(x_i)$ is a radial form factor, r is the distance between the nucleon and the center of mass of the nucleus, r_i is the radius at which the nuclear potential falls to 50% of its central value and a_i is the diffuseness parameter which determines the distance over which the form factor changes from 90% to 10% of its maximum value.

The form factor $f(x_i)$ is expected to satisfy two important conditions. Firstly, it should fall exponentially with increasing radial distance, since this is a feature of the nucleon-nucleon interaction and, secondly, it should be uniform inside the nucleus, since nuclear forces are known to saturate, that is to say a nucleon is acted upon by the immediately adjacent nucleons only and thus experiences no appreciable resultant force from other nucleons. The two requirements are represented by the Woods-Saxon form factor[19] given by

$$f(x_i) = (1 + e^{x_i})^{-1} \quad .$$

For protons one must add a Coulomb potential to the nuclear potential given in equation (8). The Coulomb potential can be represented accurately enough by a potential due to a uniformly charged sphere which has the form

$$V_c(r) = \frac{Ze^2}{2R} \left[3 - \left(\frac{r}{R}\right)^2 \right] \quad , \quad r \leqslant R$$

$$= \frac{Ze^2}{r} \quad , \quad r > R$$

where R is the Coulomb radius $R = r_c A^{1/3}$, and r_c is the radius parameter as determined in electron scattering experiments.

By introducing a surface absorption term of the form $4iW_I\, a_I \frac{d}{dr} f(x_I)$ to the volume absorption term (imaginary part of equation (8)) a better fit to the experimental data was obtained. The reason for choosing this term is that the absorption of the incident nucleons by the target nucleus is opposed by the Pauli exclusion principle inside the nucleus where most shells are filled. So we expect the absorption process to take place preferentially at the surface of the nucleus and, in particular, at lower energies where the exclusion principle is more effective.

The early optical model calculations, made with central forces alone, were found to give good fits to the differential elastic cross sections, but they predicted zero polarizations. To account for the polarization of the scattered nucleons, a spin-orbit potential term was added to the optical potential. Kerman[5] indicated that the spin-orbit potential should also be complex. In analogy with the shell model potential the spin-orbit potential is chosen to be of the Thomas form and given by:

$$(V_{so} + iW_{so}) \frac{4}{r} \left[\frac{d}{dr} f(x_{so}) \right] (\vec{S}.\vec{L})$$

where $\bar{L}$ is the orbital angular momentum of the incident nucleon and $\bar{S}$ is its spin. V_{so} and W_{so} are the depths of the real and imaginary parts of the spin-orbit potential, respectively.

In analysis of elastic scattering data it was found, however, that the imaginary part of the spin-orbit potential can be neglected in the energy region of interest here.

In recent years, McKintosh and Kobos[20] showed that elastic scattering differential cross sections and polarization data can be much better fitted if deuteron channels are explicitly coupled to the elastic channel in a $p \leftrightarrow d$ coupled reaction channel formalism. In particular, the backward angles in the

elastic scattering angular distributions, which could not otherwise be fitted, appeared to be well reproduced. Since calculations involving coupled reaction channels including deuteron channels are time consuming and ill-adapted to automatic searching, a phenomenological representation of the coupling effects was studied. McKintosh and Cordero[21] found that the effects of coupled reaction channels are very similar to those seen when an explicit ℓ-dependent term is added to the standard optical potential and that this gave qualitatively similar fits to the coupled reaction channels. It should be pointed out that the ℓ-dependent feature is in analogy with that suggested by resonating-group studies of light nuclear systems[22] which use totally antisymmetrized wave functions and a central nucleon-nucleon potential.

The ℓ-dependent term was suggested to have the form[22]

$$- V_{ex} (-1)^{\ell} f(x_{ex})$$

The general form of the optical potential can thus be written in the form:

$$U(r) = V_c(r) - V f(x_o) + i 4 a_I w_I \frac{d}{dr} f(x_I) - i W f(x_I)$$

$$+ (V_{so} + iW_{so}) \frac{4}{r} \left[\frac{d}{dr} f(x_{so}) \right] (\bar{S}.\bar{L}) - V_{ex} (-1)^{\ell} f(x_{ex}) \quad (9)$$

This potential contains fourteen adjustable parameters; eight geometrical, namely r_o, a_o, r_I, a_I, r_{so}, a_{so}, r_{ex}, a_{ex} and six dynamical parameters, V, W, W_I, V_{so}, W_{so} and V_{ex}. These parameters are adjusted to give the best fit to the experimental data by minimizing the quantity (from now on $(\frac{d\sigma}{d\Omega})$ is written as σ for simplicity).

$$\chi^2 = \sum_{i=1}^{N_\sigma} \left[\frac{\sigma_{th}(\Theta_i)-\sigma_{ex}(\Theta_i)}{\Delta \sigma_{ex}(\Theta_i)} \right]^2 + \sum_{j=1}^{N_P} \left[\frac{P_{th}(\Theta_j)-P_{ex}(\Theta_j)}{\Delta P_{ex}(\Theta_j)} \right]^2 + \left[\frac{\sigma_r^{th} - \sigma_r^{ex}}{\Delta \sigma_r^{ex}} \right]^2 , \quad (10)$$

where $\sigma_{th}(\theta_i)$, $P_{th}(\theta_j)$, $\sigma_{ex}(\theta_i)$ and $P_{ex}(\theta_j)$ are the theoretical and experimental differential cross sections and polarizations at angles θ_i and θ_j, respectively, $\Delta\sigma_{ex}(\theta_i)$ is the uncertainty in the measured differential cross section at angle θ_i, while $\Delta P_{ex}(\theta_j)$ is the experimental uncertainty in the measured polarization at angle θ_j, N_σ and N_p are the number of experimental differential cross section and polarization data points, respectively. σ_r^{th} and σ_r^{ex} are respectively the calculated and measured total reaction cross section, while $\Delta\sigma_r^{ex}$ is the uncertainty in the measured total reaction cross section.

Greenlees, Pyle and Tang[23] constructed an optical model potential, called the reformulated optical model, by folding the proton density distribution $\rho_p(\bar{r})$ and the neutron density distribution $\rho_n(\bar{r})$ with the appropriate components of the nucleon-nucleon potential to obtain the real central part of the optical potential. However, the uncertainties in choosing the appropriate nucleon-nucleon potential components form one of the drawbacks of this model. Karban and Lowe[24], when analyzing 30.3 MeV proton elastic scattering data for a variety of nuclei using the standard and reformulated optical model, have concluded that the reformulated optical model gives an unsatisfactory representation of the data, the χ^2 values being 2 to 4 times greater than those of the standard optical model. This was attributed to the increased mathematical freedom present in the standard optical model because the spin-orbit and real geometries are independent. They also concluded, in conjunction with anlyses of Greenlees et al[25], that, for medium weight nuclei, the standard optical model consistently achieves a better representation of the experimental data than the reformulated optical model.

II.2 The Optical Model and Nuclear Sizes

Work during the past ten years has emphasized the primary need to find out which parameters of the optical potential are really determined by the

scattering process. Greenlees et al.[26] have carried out optical model analyses of proton scattering data with this in mind. They found that the root mean square radius of the real central potential for low-energy nucleon scattering is quite well determined. This result has been confirmed by studies of neutron scattering[27] and further studies of proton scattering[28]. These studies also indicate that the volume integral of the real central potential is also well determined, although to a lesser extent, and this is supported by many other studies of proton scattering in the range 16-50 MeV[29-31].

The nuclear matter density, $\rho_m(\bar{r})$ can be calculated from the formula:

$$\rho_m(\bar{r}) = \frac{Z}{A} \rho_p(\bar{r}) + \frac{N}{A} \rho_n(\bar{r}) \qquad (11)$$

where $\rho_p(\bar{r})$ is the proton density distribution and $\rho_n(\bar{r})$ is the neutron density distribution with the normalization conditions $\int \rho_m(\bar{r})\, d\bar{r} = \int \rho_p(\bar{r})\, d\bar{r} = \int \rho_n(\bar{r})\, d\bar{r} = 1$.

The simplest situation of equation (11) arises if the proton and neutron distributions $\rho_p(\bar{r})$ and $\rho_n(\bar{r})$ are identical. This implies that if the nuclear charge distribution is determined from electromagnetic interaction studies, the matter distribution would be known also. In many situations involving electromagnetic interactions, the nuclear charge distribution $\rho_{ch}(\bar{r})$ of the nucleus is required instead of the distribution of point protons. Since the proton is not a point charge but has a finite size, $\rho_{ch}(\bar{r})$ can be obtained from the proton distribution, $\rho_p(\bar{r})$ by folding in the charge distribution of the proton itself, i.e.

$$\rho_{ch}(\bar{r}) = \int \rho_p(\bar{r}')\, \rho_d(|\bar{r} - \bar{r}'|)\, d\bar{r}' \qquad (12)$$

where ρ_d represents the charge distribution of the proton.

From the folding integral (12) the r.m.s. radius of ρ_{ch} is increased relative to that of ρ_p according to:

$$< r^2 >_{ch} = < r^2 >_p + < r^2 >_d$$

$$< r^2 >_{ch} = < r^2 >_p + 0.64 \quad fm^2 \tag{13}$$

where the value of $< r^2 >_d$ is taken from Champers et al.[32].

Now the real central potential is of the form

$$V(r) = V_o[\, 1 + \exp(r - r_o A^{1/3})/a_o]^{-1} \quad .$$

The m.s. (mean square) radius is given by

$$< r^2 >_{op} = \frac{\int r^2 \, V(r) \, d\bar{r}}{\int V(r) \, d\bar{r}}$$

$$= \frac{\int r^4 [\, e^{r_o A^{1/3}/a_o} + e^{r/a_o}]^{-1} \, dr}{\int r^2 [\, e^{r_o A^{1/3}/a_o} + e^{r/a_o}]^{-1} \, dr} \quad .$$

$< r^2 >_{op}$ can be evaluated approximately to order $(\frac{a_o}{r_o A^{1/3}})$ and one obtains,

$$< r^2 >_{op} = \frac{3}{5} r_o^2 + \frac{7}{5} \pi^2 a_o^2 \quad , \tag{14}$$

where r_o and a_o are obtained from the best fit optical model parameters for the real central potential.

Greenlees, Pyle and Tang[23] have shown that, to a first approximation, the m.s. radius of the matter distribution and the m.s. radius of the optical potential are related by

$$< r^2 >_m = < r^2 >_{op} - < r^2 >_{2b} \quad , \tag{15}$$

where $< r^2 >_{2b}$ is the mean square radius of the nucleon-nucleon interaction.

When equations (11), (13), (14) and (15) are combined one can obtain the r.m.s. radius of the matter and neutron distributions, provided $< r^2 >_{2b}$ is determined from analysis of nucleon-nucleon data. It will be shown later how this term, $< r^2 >_{2b}$, which is not very well known, can be avoided when one

is interested instead with differences between the r.m.s. radii of the proton and neutron distributions in the calcium isotopes.

CHAPTER III

Experimental Details

III.1 Cyclotron and Beam Line

Fig. 1 is a layout of the cyclotron and the beam line. Quadrupole doublets Q1, Q2 and Q3 are used to focus the proton beam through the beam transport system. Q1 produces a horizontal waist at the first set of slits, Q2 is used to give an energy focus at the second set of slits and Q3 produces a waist in the proton beam at the center of the scattering chamber. The vertical and horizontal slits (Slit 1) define the object plane in front of the bending magnet. These slits are set at a separation of about 1.0 cm vertically and 0.5 cm horizontally. A second slit system (Slit 2) is placed at the focal plane of the bending magnet to momentum analyze the proton beam used in the experiment. These slits have the same setting as Slit 1. The slit settings correspond to an energy spread of 200 keV (FWHM) at 45.0 MeV. Screens 1,2,3 and 4 can be lowered into the beam line to monitor the beam transport by means of closed circuit television. Steering magnets S1, S2 and S3 are available to center the beam with respect to the central axis of the beam line. The bending magnet deflected the proton beam into the 45° left beam-line where the experiment was performed.

A lead collimator (10 cm long and with an aperture of 4 cm diameter) is placed in the beam line in front of the entrance of the scattering chamber, to reduce the γ-ray background produced at the second set of slits. Additional lead shielding is arranged around the entrance of the scattering chamber.

III.2 The Scattering Chamber

The scattering chamber used is made of mild steel and is about 1.20 m in diameter and 0.60 m in depth. The scattering chamber is bolted to the floor of the experimental area to avoid any shift in position. During operation the

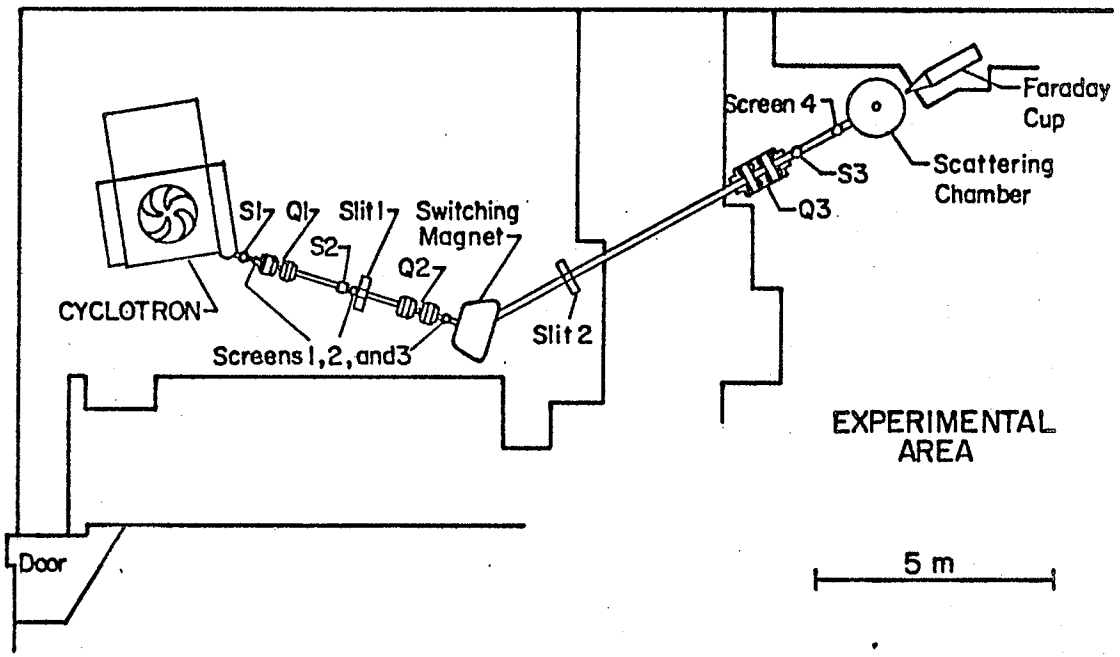

EXPERIMENTAL LAYOUT

Fig. 1

chamber is maintained at a vacuum of about 2 mPa. A rotatable turntable is mounted inside the base of the chamber. The turntable can be rotated from -180° to $+180^{\circ}$ and is driven by an external electric motor via a sprocket gear and chain. The turntable can be rotated either locally from the experimental area or remotely from the control room. A digital readout of the position of the turntable in the chamber is provided by an external decitrak shaft encoder (reading angles in hundredths of a degree).

Rigidly mounted on the turntable are two detector arrays, one containing eight NaI(Tℓ) detectors and another containing nine NaI(Tℓ) detectors. The detectors in each array are placed in special detector holders and enclosed in a vacuum tight crescent shaped aluminum housing. The latter makes it possible to have the detectors at atmospheric pressure while the scattering chamber itself is evacuated. Each detector consists of a single thallium-activated sodium iodide scintillation crystal NaI(Tℓ) (3.8 cm in diameter and 1.3 cm thick). The NaI(Tℓ) crystal is optically coupled to a photomultiplier tube (RCA 4523) via a 1.3 cm thick quartz light pipe. The two aluminum housings are separated by a fixed angle of (30.00 $\pm$ 0.03) degrees between the centers of the first collimators. On the inner arc of each housing there are windows which are covered by 50μ Kapton H-foil. The NaI(Tℓ) detectors in each detector array are set behind these windows. At the front surface of the crescent shaped boxes, interchangeable collimators are mounted in front of each window. The angular separation of the centers of any two adjacent collimators within each detector array is (10.00 $\pm$ 0.03) degrees. The distance from the center of the scattering chamber to the center of each collimator and the dimensions of each collimator aperture are accurately measured. Fig. 2 shows the arrangement of solid angle defining slits. Their dimensions are given in Table 3 together with the solid angles and their

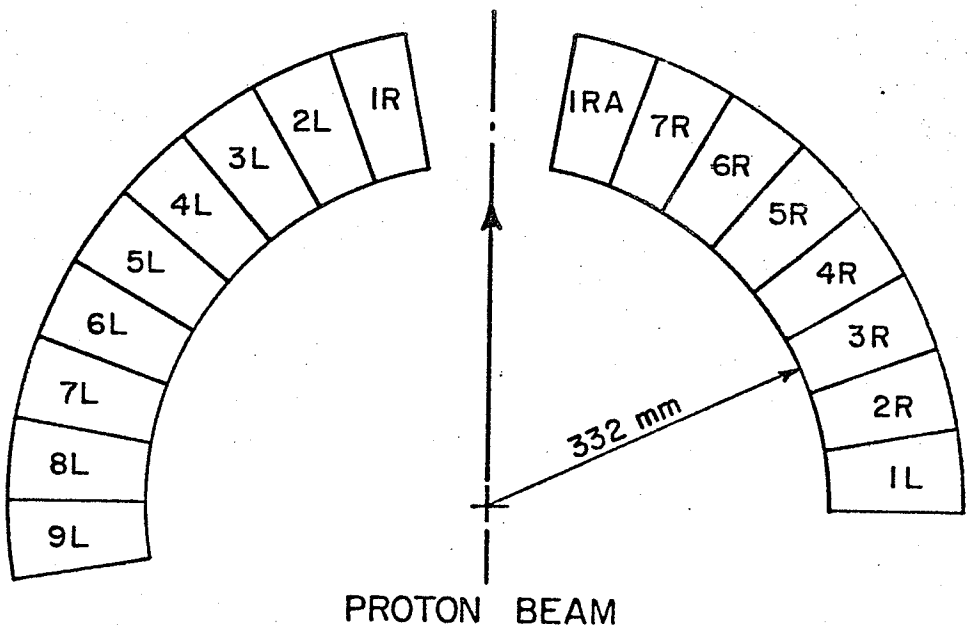

Fig.2 Arrangement of the solid angle defining slits inside the scattering chamber.

Slit No.	Width (mm)	Height (mm)	Solid Angle Ω (mSr)	$\Delta\Omega$ (mSr)
1L	4.76	12.51	0.5402	0.0051
2R	4.65	12.76	0.5383	0.0049
3R	4.64	12.60	0.5304	0.0049
4R	4.65	12.61	0.5320	0.0049
5R	4.65	12.61	0.5320	0.0049
6R	4.63	12.59	0.5288	0.0049
7R	4.65	12.61	0.5320	0.0049
1RA	3.07	12.58	0.3504	0.0033
1R	3.09	12.59	0.3529	0.0033
2L	4.70	12.70	0.5415	0.0051
3L	4.76	12.51	0.5402	0.0051
4L	4.76	12.50	0.5398	0.0051
5L	4.69	12.70	0.5404	0.0051
6L	4.76	12.48	0.5389	0.0050
7L	4.67	12.70	0.5381	0.0050
8L	4.69	12.70	0.5404	0.0051
9L	4.76	12.47	0.5385	0.0050

TABLE 3

SLIT DIMENSIONS AND SOLID ANGLES

associated uncertainties. Also mounted on the turntable between the scattering chamber center and the detector arrays is an additional set of collimating slits and two sets of antiscatter baffles. The set of slits closest to the scattering chamber center is to define the target thickness when a gas target is used. The collimator system permits simultaneous measurements to be made left and right of the beam axis at symmetric angles. Four positions of the turntable thus cover the range 10° - 170° in 5 degree steps (see Figs.3a and b).

Cubic boxes with signal and high voltage vacuum feed-throughs and poly-flo feed-throughs are connected to the lower lid of the scattering chamber. Inside the chamber signal and high voltage cables connect the detectors in each detector array with the cubic boxes. The poly-flo tubes are connected to the detector boxes so that the detectors are kept at atmospheric pressure.

A target ladder which can hold five solid targets or four solid targets and a gas target cell can be lowered into the center of the chamber via a target lock mounted on the top lid of the scattering chamber. The target ladder can be moved along and rotated around the central axis of the turntable. The target position and angle are read off scales outside the assembly. The target angle can be set with an accuracy of approximately $\pm$ 0.75°.

The detectors are carefully aligned in the chamber. A theodolite is accurately levelled and set up in such a way that it can be rotated in the vertical plane and alternatley view a pin in the center of the momentum analyzing bending magnet and a pin in the center of the scattering chamber. In this way one can make sure that the center of the bending magnet, the center of the second slit system (S2), the magnetic axis of the quadrupole doublet Q3, and the center of the scattering chamber lie on a straight line. The height of the theodolite is then adjusted so that the theodolite is level with the median plane of the bending magnet. After the theodolite is properly set each

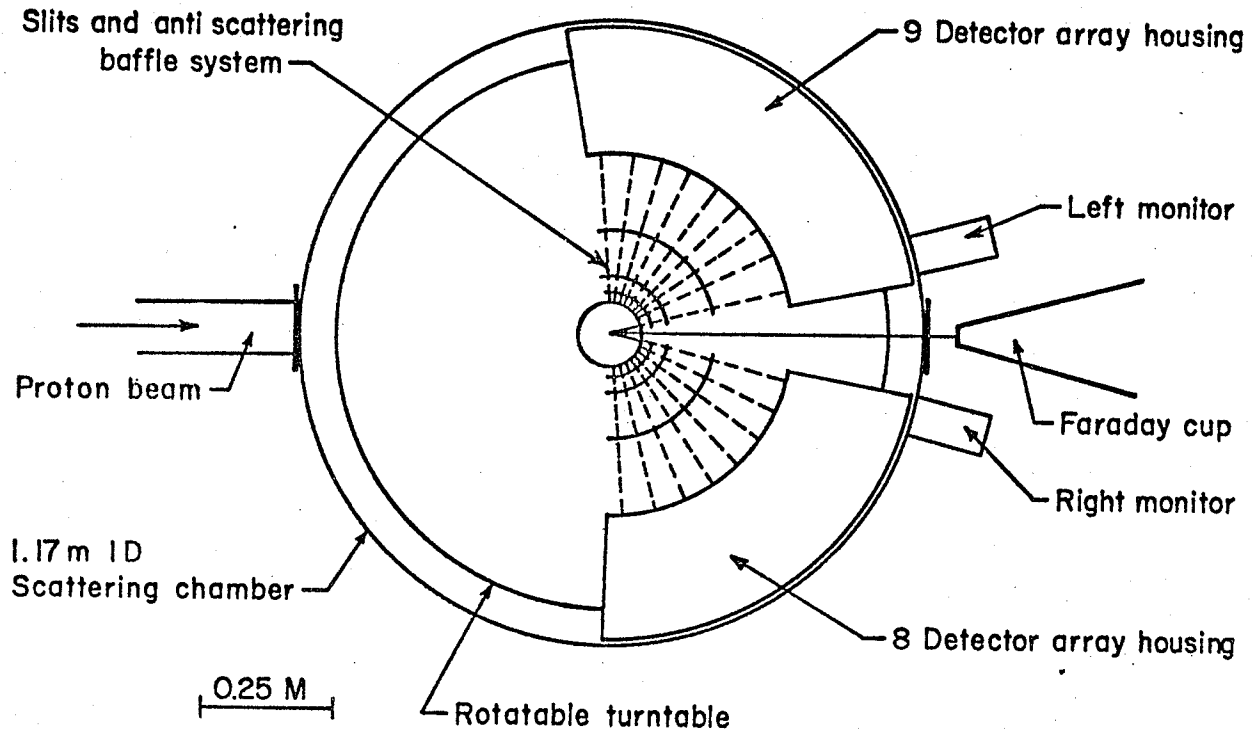

SCATTERING CHAMBER

Fig. 3-a

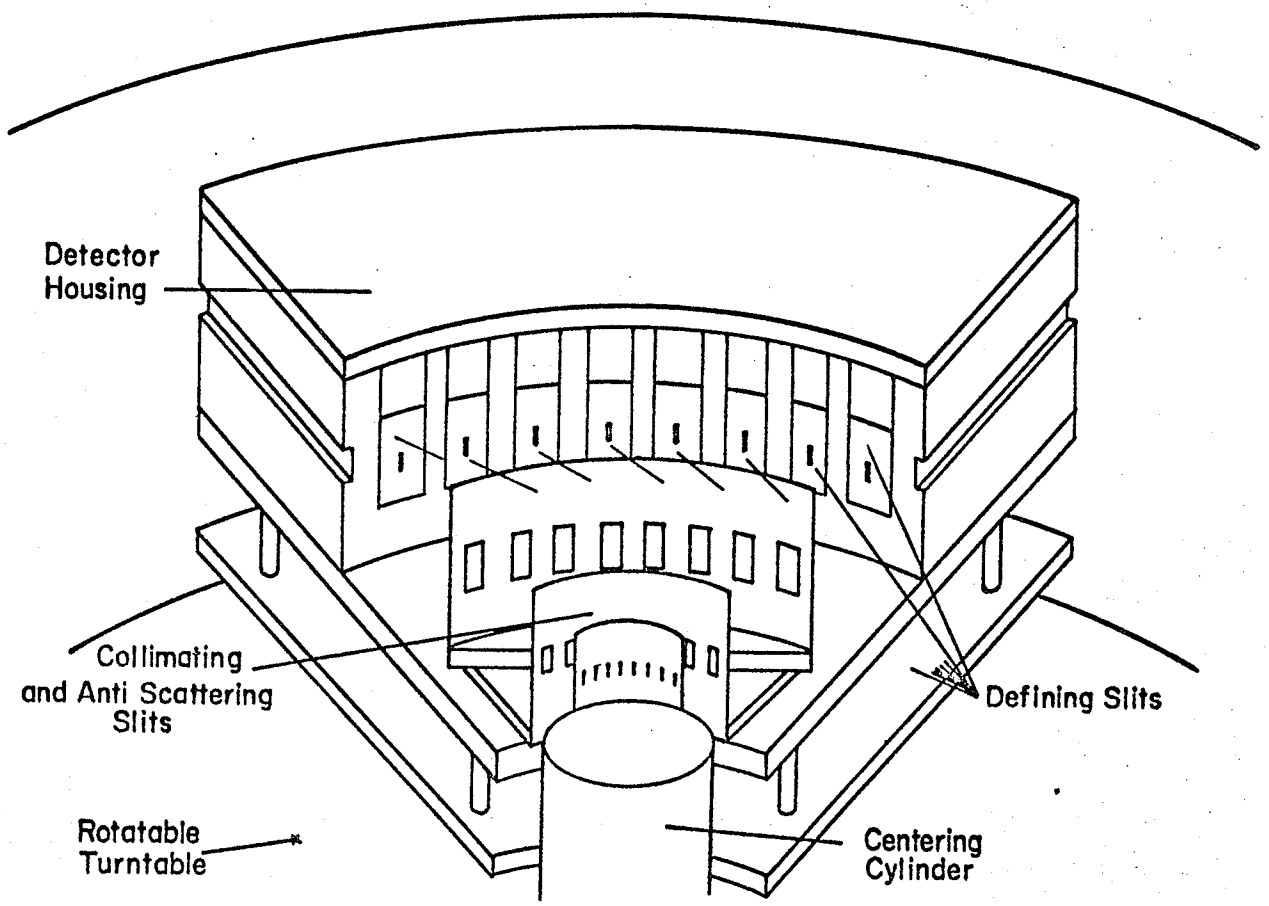

DETECTOR AND SLIT SYSTEM

Fig.3-b

detector is viewed through the theodolite by rotating the turntable until the detector is positioned at zero degrees. By aligning the cross hairs of the theodolite with alignment marks at the center of each solid angle defining slit one makes sure that the detector is properly aligned. In a similar way the gas target thickness defining slits and antiscatter baffles are aligned.

The target ladder is then lowered into the target position. The theodolite is used to check that the target ladder is centered vertically on the median plane of the scattering chamber. Under vacuum the scattering chamber lid bends slightly, thus lowering the target position. This effect is corrected for appropriately. The target angle readout is checked by setting the target at 0.00^{o} and looking through the theodolite to make sure that the face of the target is parallel to the line of sight.

The protons which traverse the scattering chamber are collected in a Faraday cup which is used to measure the proton beam incident on the target. The Faraday cup consists of a hollow carbon cylinder (1.25 m long, 0.28 m diameter and 0.03 m wall thickness) with a carbon disk at the end to stop charged particles (0.03 m thick) and an outer teflon cylinder for insulation. The Faraday cup is maintained at a vacuum of about 3 mPa and has a leakage resistance to ground greater than 10^{15} Ω. A brass electron suppressor ring at the entrance of the cup is held at -1500 volts in order to repel secondary electrons produced by stopping protons in the Faraday cup, or by ejection from upstream foils. The charge collected in the Faraday cup is measured with a charge integrator (Brookhaven Instruments, model 1000) which has an accuracy of 0.1% for its digitized output. The proton beam generally had a 'halo' structure of an undetermined dimension. Past experience has shown that the 'halo',which may not entirely be collected in the Faraday cup,represents <1% of the total proton beam intensity. An overall uncertainty of 1% was therefore

assigned to the charge integration. The charge collected is used as a normalization factor.

The Faraday cup is surrounded by steel bricks giving an enclosure approximately 1 m high by 1 m wide by 3 m long to reduce the neutron and γ-ray background. The bending magnet is used to momentum analyze the beam and to determine the incident proton beam energy. The magnetic field strength is calibrated using a cross-over technique[33]. In this technique the scattering angle at which protons elastically scattered from one kind of nucleus have the same energy as those inelastically scattered from a heavier nucleus uniquely determines the proton beam energy and zero degree axis of the scattering chamber.

A CH_2 target of thickness about 3 mg/cm^2 is used for the cross over measurement. The measurements are made at 25.6, 35.4 and 43.9 MeV. The kinematic cross-over of protons elastically scattered from hydrogen and inelastically scattered from the 4.43 MeV ^{12}C excited state is observed. Six detectors are used, three on either side of the incident proton beam axis. Spectra are collected both left and right of the beam direction, at a large number of angles in the range where the cross-over occurs. The centroids of the hydrogen, the elastic and the 4.43 MeV ^{12}C excited state peaks of each spectrum are found using centroid calculations. A gain independent ratio (the ratio, R, of the difference between the hydrogen and carbon elastic peaks to the difference between the carbon elastic and carbon first excited state peaks) is plotted as a function of angle. A quadratic fit to the data points is performed and the cross-over angle (the angle at which the separation between the hydrogen and the carbon first excited peaks is zero, or the ratio R equals unity) is found. Determining the cross-over angle, and thus the incident proton beam energy, for a number of energies, and using an nmr probe of the magnetic field of the

bending magnet in each case permits one to calibrate the proton beam energy in terms of the magnetic field strength. The values of the G-factor (a quantity proportional to the momentum of the incident proton beam) determined from the cross-over measurements were 41.470, 41.607 and 41.610 at 25.6, 35.4 and 43.9 MeV, respectively. This yielded an average value of G equal to 41.562 ± 0.080 (compared to an old G-value of 41.516 ± 0.062), which corresponds to an uncertainty in the determination of the proton beam energy of about 200 keV at 50 MeV.

III.3 Targets

Isotopically enriched self supporting targets of ^{40}Ca, ^{42}Ca and ^{44}Ca were purchased from Oak Ridge National Laboratory. Each target is rectangular in shape with dimensions of 2.54 by 1.27 cm. The targets are weighed, photographed (on a reference scale) and mounted on the target ladder in a glove box filled with argon gas to avoid oxidation of the targets. The target ladder is mounted directly through the top of the glove box for mounting the targets and transporting them to the scattering chamber.

Using the weight and measuring the area of each target from the photographs, the thickness is calculated by dividing the target weight by the area. The thickness of the targets, together with the isotopic enrichment is shown in Table 4.

Table 4

Isotope	$\rho x \pm \Delta\rho x$ mg/cm^2	Purity %
^{40}Ca	6.571 ± 0.130	99.97
^{42}Ca	5.868 ± 0.106	93.70
^{44}Ca	6.710 ± 0.102	98.55

III.4 Electronics

The electronics system used is shown in Figs. 4a and 4b. The signals from the detectors are preamplified in the experimental area, and then are sent via coaxial cables to amplifiers in the control room. The coaxial cables are of the type RG62/U (93 Ω) and pass through a grounded metal conduit between the experimental area and the control room to reduce electrical noise.

The prompt bipolar signals from the amplifiers are fed into timing single channel analyzers (TSCA's) which are used to set thresholds and provide gating signals. The outputs of the TSCA's are sent to fast scalers and are used to open linear gates operated in the "normally closed" mode. The unipolar delayed signals from the amplifiers are sent to the linear gate inputs. The delay on the linear signal from the amplifiers and the width of the gating signals from the TSCA's are adjusted so that the gating signals overlap the linear signals. Thus, when a valid event above threshold occurs, the linear signals from the linear gates are transmitted to an analog-to-digital converter (ADC). During the experiment spectra from seventeen detectors are accumulated in fourteen ADC's (six Northern Scientific NS-625 and one CAMAC AD811 ADC containing eight peak - measuring analog-to-digial converters). Eleven spectra are accumulated in single ADC's and, in addition, three pairs of detectors are formed, each pair being mixed in a dual sum and invert amplifier (DSI) and then fed into one ADC. The two spectra of each pair are then routed into separate display regions. The eight CAMAC channels are normally in a closed state, so the unit has to be triggered by an external strobe pulse to start a conversion. The strobe pulse is obtained from a coincidence unit (see Fig. 4a) and has a duration of 8 ns with the leading edge preceding the data signal ($\sim$ 500 ns duration) by at least 200 ns. The ADC's are interfaced to a PDP 15/20 computer. The spectra are stored in seventeen memory regions, each consisting of 512 channels.

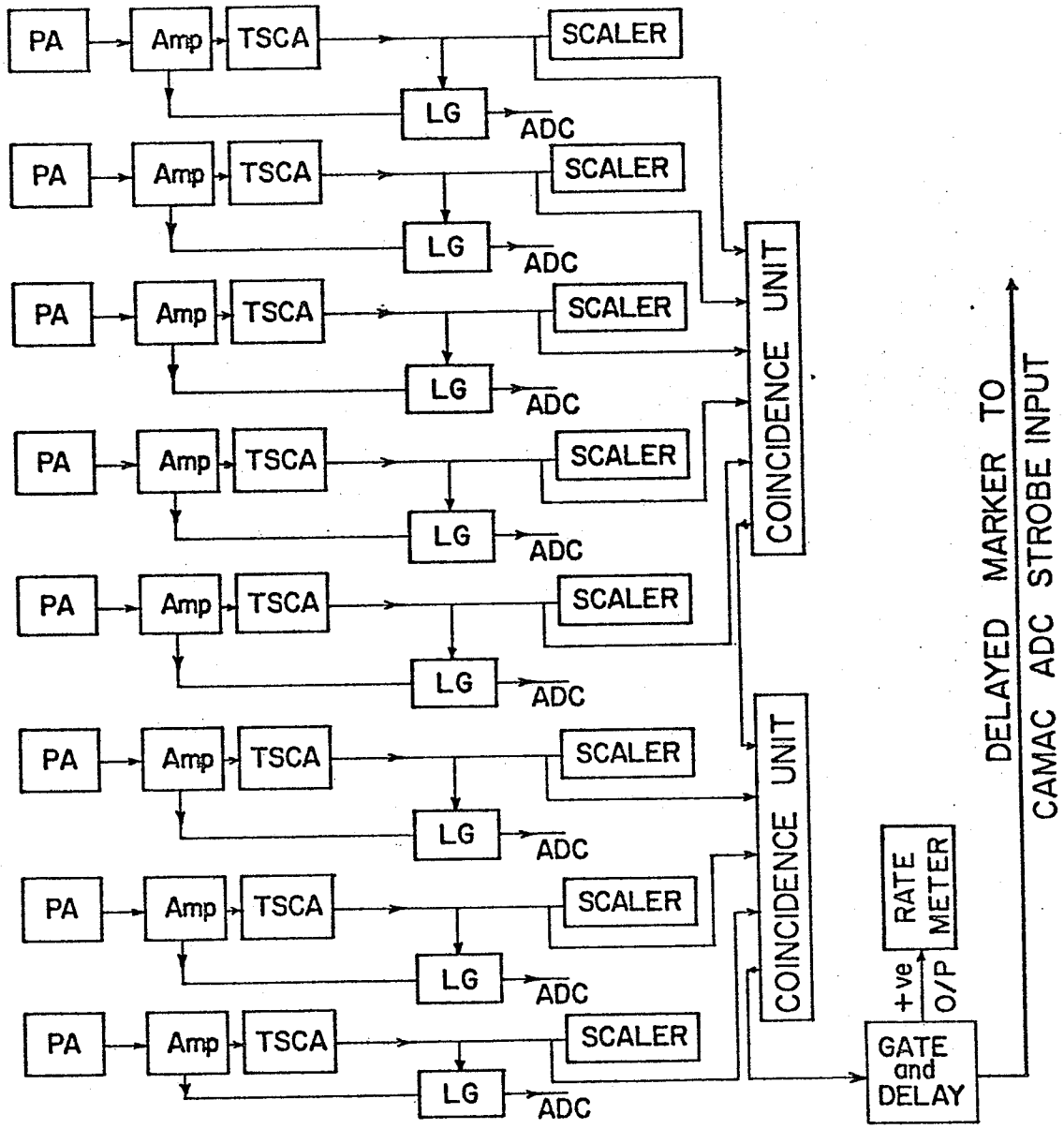

Electronics Diagram with CAMAC ADC's

Fig. 4-a

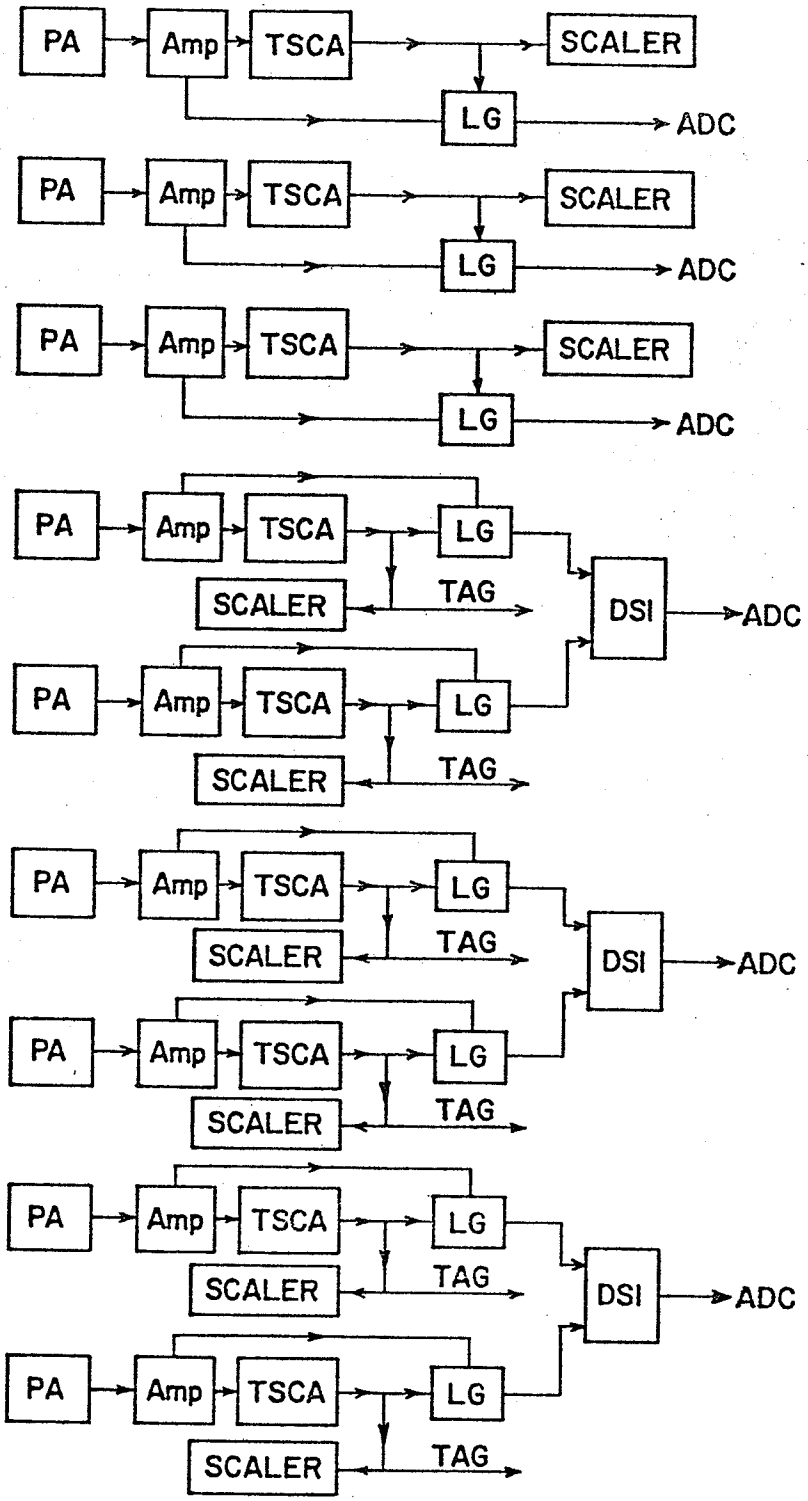

Electronics Diagram with Northern Scientific ADC's

Fig. 4-b

III.5 Experimental Procedure

In order to set up the proton beam a plastic scintillation target is mounted on the target ladder and inserted at the target position at the center of the chamber. The beam transport parameters can be adjusted to focus the beam and adjust the beam spot size at the center of the target by viewing the beam spot on the scintillator target via closed circuit televison. The beam was required to be non steering by the last quadrupole pair (Q3 in Fig. 1). A beam spot at the target was typically 3 mm wide and 6 mm high.

Two NaI(Tℓ) detectors with nearly identical geometries were mounted on the scattering chamber in the horizontal plane at equal angles (15.00°) on either side of the beam axis in order to check whether or not the proton beam is traversing the chamber on axis and to monitor any variation of the incident beam direction. Using the fact that for medium-weight and heavy target nuclei the forward scattering cross section varies rapidly with angle, the ratio of the numbers of protons elastically scattered by a Ni foil into the left and right monitor detectors gives an accurate indication of the proton beam being on or off the central axis of the chamber. Adjustments to the beam transport parameters were made until the ratio of the number of protons elastically scattered into the two monitor detectors was 1.00 ± 0.01.

After a well-defined proton beam was obtained with the desired energy, the detector arrays were set in a specified position and the run started. Simultaneous measurements were made left and right of the beam axis at eight symmetric angles. Data were accumulated in the form of spectra for the detectors. In order to have good statistics the run was considered finished when more than 5000 (10000 summed left and right) counts had been recorded in each elastic peak. The spectra were stored on magnetic tapes for later analysis. The counts recorded by the scalers and the Faraday cup were recorded.

The detector arrays were then moved to another position and the process repeated. This process was continued until satisfactory data had been collected both left and right of the beam axis for angles from 10° to 170° in 2.5° steps in the forward direction and 5° steps in the backward direction.

Data have been obtained at 21.0, 25.0, 30.0, 35.0, 40.0, 45.0 and 48.4 MeV for ^{42}Ca and ^{44}Ca and at 25.0, 27.5, 30.0, 35.0, 40.0 and 45.0 MeV for ^{40}Ca. Typical spectra resulting from the interaction of protons with the three calcium isotopes are shown in Figs. 5a, b and c.

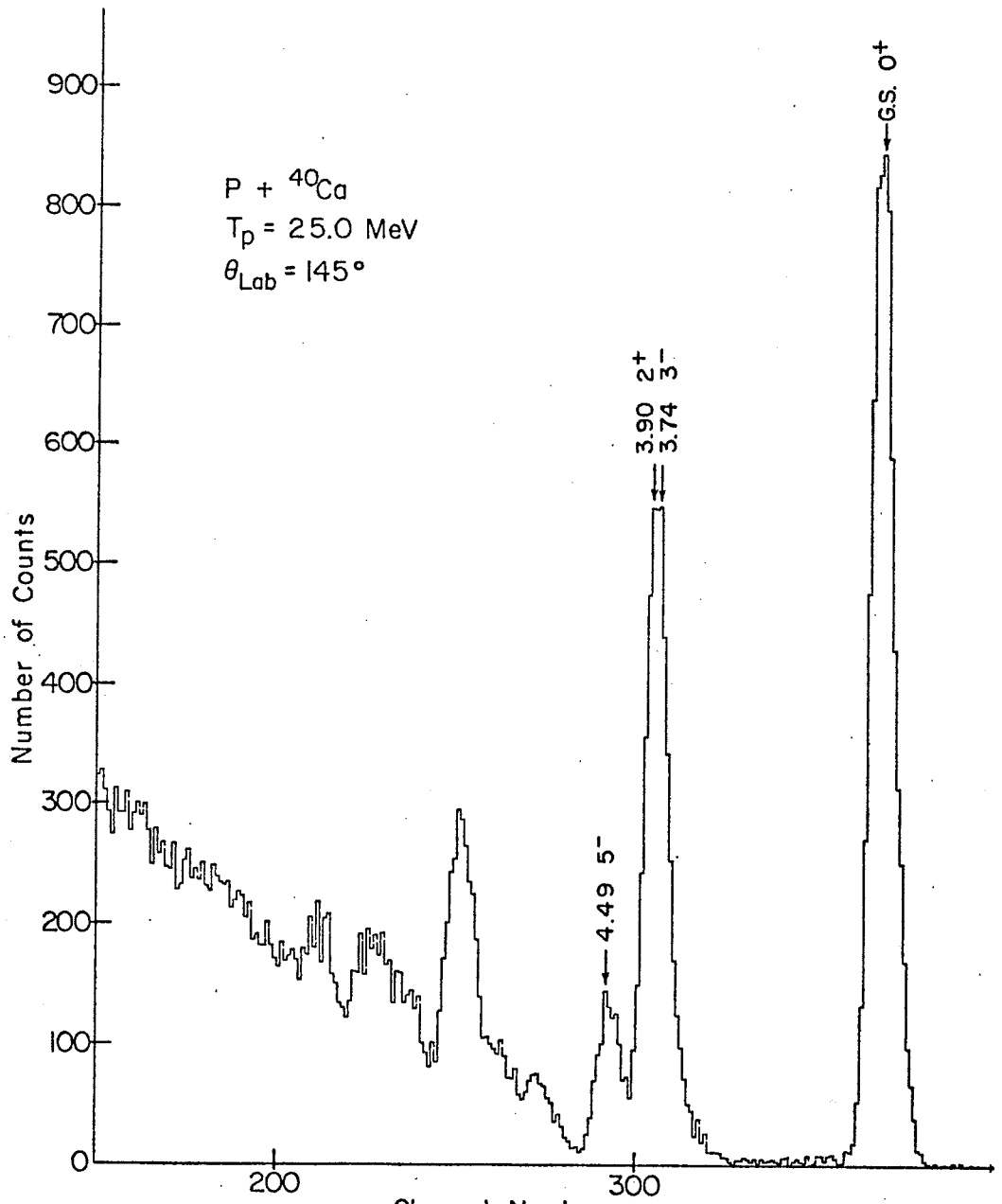
P + 40Ca
Tp = 25.0 MeV
θLab = 145°
G.S. 0+
3.90 2+
3.74 3−
4.49 5−
Number of Counts
Channel Number
0
100
200
300
400
500
600
700
800
900
200
300

Fig. 5 – a

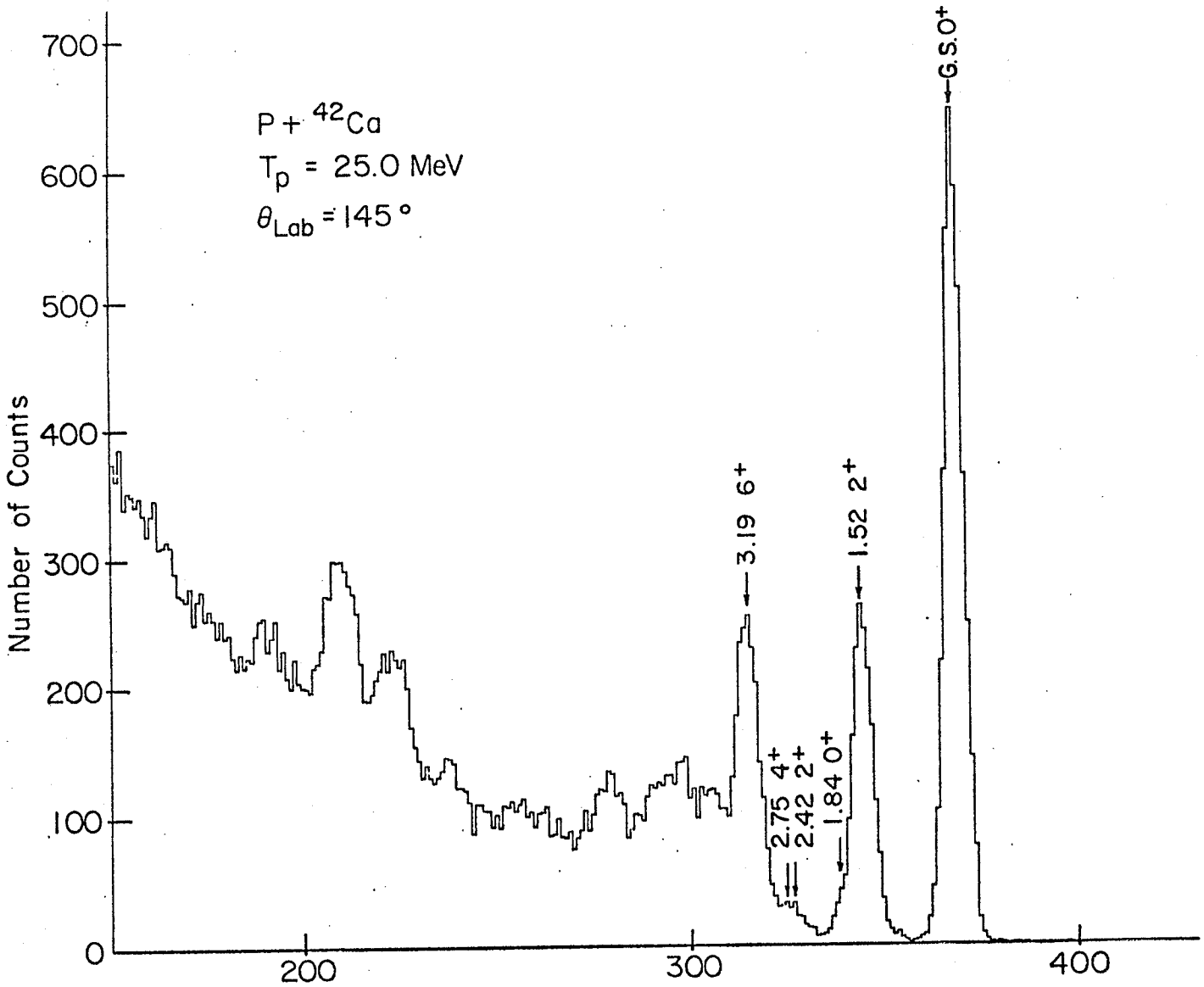
P + 42Ca
Tp = 25.0 MeV
θLab = 145°
G.S. 0+
1.52 2+
1.84 0+
2.42 2+
2.75 4+
3.19 6+
Number of Counts
Channel Number
0
100
200
300
400
500
600
700
200
300
400

Fig. 5 - b

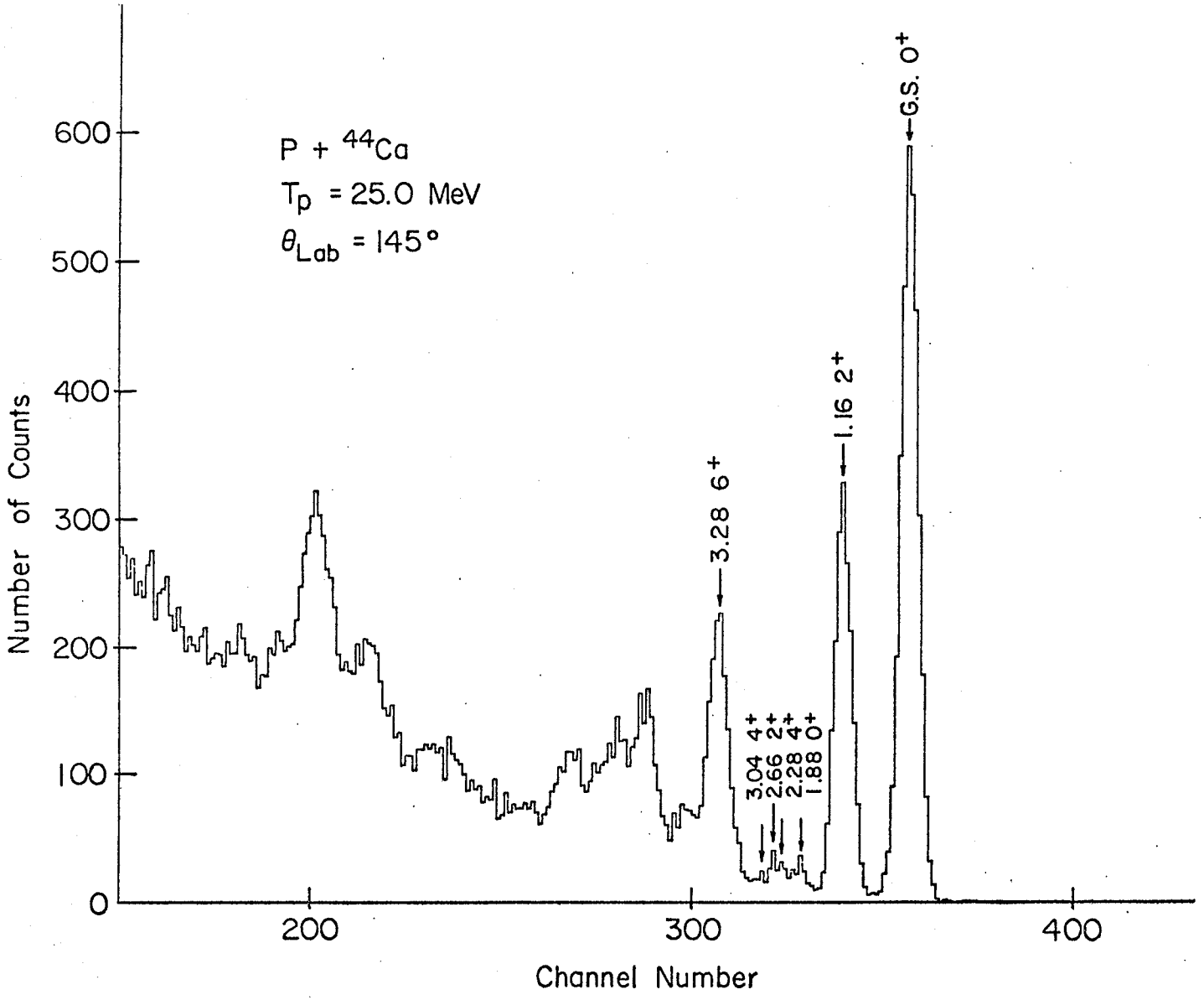
P + 44Ca
Tp = 25.0 MeV
θLab = 145°
G.S. 0+
1.16 2+
3.28 6+
3.04 4+
2.66 2+
2.28 4+
1.88 0+
Number of Counts
Channel Number
0
100
200
300
400
500
600
200
300
400

Fig. 5 - c

CHAPTER IV

IV.1 Data Reduction and Corrections

The uncorrected elastic scattering differential cross sections are calculated using the formula

$$\left(\frac{d\sigma}{d\Omega}\right) = \frac{y(\theta)\ A \cos\phi}{I_o\ N\ t\ d\Omega} \qquad (16)$$

where,

$y(\theta)$ is the number of protons elastically scattered by the target at an angle θ into the solid angle element $d\Omega$;

A is the atomic mass of the target nucleus in grams;

ϕ is the angle between the incident proton beam direction and the normal to the plane of the target;

I_o is the number of protons incident on the target as measured by the Faraday cup;

N is Avogadro's number;

t is the target thickness in gm/cm^2, and

$d\Omega$ is the solid angle subtended by the detector.

$y(\theta)$ is obtained by integrating the elastic peak in the spectrum for angle θ after the background has been subtracted.

A computer program was used to subtract the background, unfold the peaks and calculate the number of protons in the elastic peak. The background was calculated by assuming that the background at any particular channel is due to the background produced by events at higher energies. The contribution that each of these higher channels makes is assumed to be proportional to its amplitude (see Fig. 6). The program was capable of displaying the calculated background under the elastic peak on the screen of the computer for visual inspection. One could also raise or lower the calculated background by manual control of the console switches of the computer. The shape of the calculated

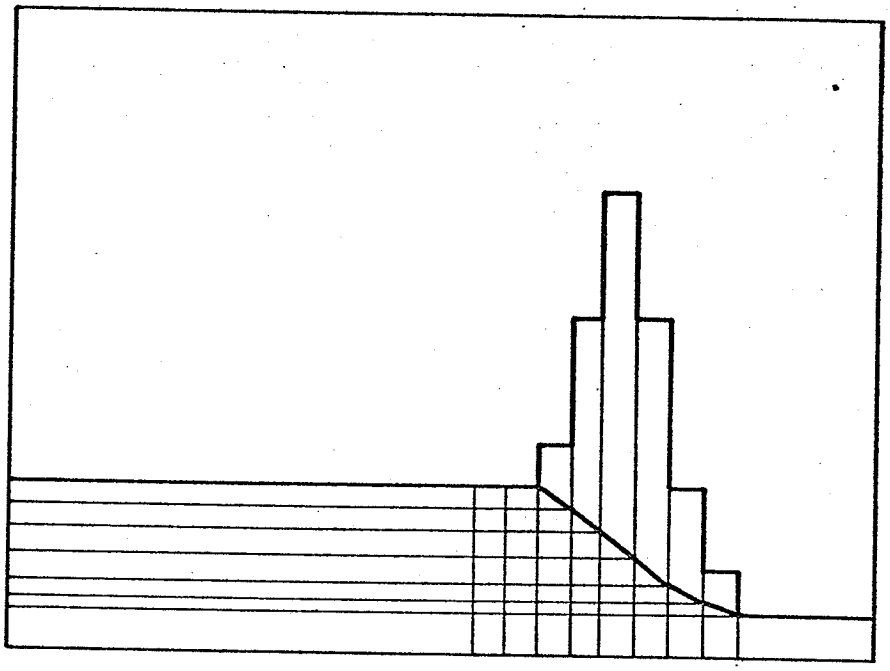

Fig. 6
Illustration of the background subtraction.

background under the elastic peaks could be approximated by a straight line as can be seen in Fig. 6. When the calculated background under the elastic peak was compared with another linear background subtraction program, the results were found to be consistent within 1%. When the first excited state and elastic scattering peaks partially overlapped, the program unfolded them by using the elastic peak as the characteristic peak shape.

Corrections have to be made to the differential cross sections calculated form equation (16). These corrections are:

1.i Dead Time Correction

This correction accounts for the fact that the yield, $y(\theta)$, in equation (16) obtained by integrating the elastic peak in the observed spectrum corresponds to events recorded by the computer and not to the total number of protons scattered into the solid angle element $d\Omega$. Corrections must be made for finite dead times of the analog to digital converters (ADC's). The dead time correction factor, τ, is taken to be the ratio of the counts sent to the ADC's (recorded by scalers) to the total number of counts in the corresponding spectrum recorded by the computer. This correction is about 10% for the most forward angles and less than 1.0% at backward angles.

1.ii Finite Beam Geometry Correction

In order to take into account that the measurements were made with finite apertures for the solid angle defining collimators and a beam of finite size and divergence at the target, a finite beam geometry formula derived by Wilmes[34] was used. The calculation of this correction required the knowledge of the first and second derivatives of the elastic scattering differential cross section with respect to the scattering angle. The derivatives are calculated from preliminary differential cross section angular distributions. This correction was found to range between 1.5 and 2.0% at the first minima of the angular

distributions and to be less than 1.0% at other angles.

1.iii Nuclear Reactions In The Detector Material

Some protons which are elastically scattered from the target into the detector are lost by undergoing nuclear reactions in the NaI(Tℓ) detector material. For each measurement the energy of the elastically scattered protons entering the detector is calculated. The percentage loss due to nuclear reactions in the detector material was found by interpolation of the results of Sourkes et al.[35]. This correction always amounted to less than 3.0%.

1.iv Corrections For Target Impurities

The ^{42}Ca target contains atomic impurities of 4.96% ^{40}Ca and 1.18% ^{44}Ca, while the ^{44}Ca target contains atomic impurities of 1.38% ^{40}Ca. Corrections for these isotopic impurities as well as any oxygen contamination of the target must be considered.

For those spectra in which the elastic peak overlapped with peaks due to impurities in the target, the following general formula was used to calculate the corrected cross section, $(\frac{d\sigma}{d\Omega})_o$:

$$(\frac{d\sigma}{d\Omega})_o = \frac{A_o Y_u}{I_o N t_o d\Omega} - \sum_i \frac{A_o t_i}{A_i t_o} (\frac{d\sigma}{d\Omega})_i , \qquad (17)$$

where A_o is the atomic weight of the target nucleus, A_i is that of the i^{th} impurity, t_o and t_i are the contributions to the target thickness of the nucleus under consideration and of the i^{th} impurity, Y_u is the uncorrected yield and $(\frac{d\sigma}{d\Omega})_i$ is the differential cross section for scattering by impurity i. The effective thickness of the target nucleus, t_o, was calculated from $t_o = t - \sum_i t_i$ where t is the measured target thickness and t_i is the target thickness of the impurity in the target. The target thicknesses of the impurities were determined for each of the targets used. This was done by choosing for each

target a number of spectra in which the peaks due to elastic scattering from the contaminants were clearly resolved from those due to elastic scattering from the main constituent. The peaks of the contaminants were then integrated and the thicknesses were calculated from the known values of the differential cross sections for the contaminants[36-39].

IV.2 Uncertainties In The Measured Cross Sections

2.i The Relative Errors

(a) Statistical error. This error is calculated as $\sqrt{y + 2B}$, where y is the number of counts in the elastic peak with the background subtracted and B is the background associated with the peak. This error was always $\leq$ 1.0%.

(b) Error in the calculation of the dead time correction factor. If τ is the dead time correction factor (as explained in 1.i), the uncertainty is taken as $\frac{\tau - 1}{\tau}$ x 10%, where the factor 10% was calculated by assuming the elastic peak represents about 5% of the total counts in the spectrum and an average dead time of 2%. This error is less than 1.0% at forward angles and about 0.2% at backward angles.

(c) Error due to the uncertainty in the scattering angle θ. This error was obtained from

$$\Delta\sigma = \left[\frac{\partial\sigma}{\partial\theta} \right]_E \cdot \Delta\theta$$

with $\Delta\theta = 0.03^{\circ}$ (determined from detector allignments as discussed in Chapter 3) and was found to be $\leq$ 1.0% in all cases.

(d) Error resulting from the uncertainty in the incident proton energy. This is obtained from

$$\Delta\sigma = \left(\frac{\partial\sigma}{\partial E}\right)_\theta \Delta E$$

with ΔE = 0.2 MeV, determined from the energy calibration method as discussed before. Note that $\left(\frac{\partial\sigma}{\partial E}\right)_\theta$ has a different value for different angles θ. Furthermore

the angular distributions were not always obtained without interruption thus requiring resetting or retunning of the beam transport parameters. This makes the quantity $(\frac{\partial\sigma}{\partial E})_\theta \Delta E$ a relative uncertainty in the measured cross sections. This error was found to be $\leq$ 1.5%.

(e) Error in the calculation of the geometrical correction factor. An uncertainty of 5% is assigned to this correction to account for uncertainties in the calculation of the first and second derivatives of the cross section with respect to angle and uncertainties in measuring the geometrical parameters of the scattering chamber. This error was found to be $\leq$ 0.3%.

(f) Error in the calculation of the number of protons undergoing nuclear reactions in the NaI(Tℓ) detector. An uncertainty of 5% in the number of protons lost is taken to account for experimental uncertainties in the measured percentage loss[35] and the uncertainty in the interpolation technique. This error is less than 0.1%.

(g) Error in the correction for target impurities. This error is calculated by taking into account the uncertainty in each term on the right hand side of equation (17). The error is about 2.0%. The relative errors are shown in Table 5.

The total relative uncertainty, $\Delta\sigma_i$, in the measured differential cross section at any angle θ is calculated by taking the square root of the sum of the squares of the individual uncertainties discussed above.

Since more than one measurement is made at the same angle for a given energy, the following formula is used to find the mean differential cross section:

$$\langle \sigma \rangle = \frac{\sum_{i=1}^{n} \frac{\sigma_i}{(\Delta\sigma_i)^2}}{\sum_{i=1}^{n} \frac{1}{(\Delta\sigma_i)^2}} ,$$

where n is the number of independent measurements at the same angle θ, σ_i is

the measured differential cross section and $\Delta\sigma_i$ is the experimental uncertainty in the i^{th} measurement.

The mean square of the uncertainty in the mean value, $< \sigma >$, is then calculated using

$$\frac{\sum_{i=1}^{n} \left(\frac{\sigma_i - < \sigma >}{\Delta\sigma_i}\right)^2}{(n-1)\sum_{i=1}^{n} \left(\frac{1}{\Delta\sigma_i}\right)^2}$$

2.ii The Absolute Errors

These errors are due to the following

(a) The uncertainty in the measurements of target thickness (Chapter III Table 4)

(b) The uncertainty in the beam current integration (1.0%).

(c) The uncertainty in the determination of the solid angle subtended by the detectors ($\sim$ 1.0%)

(d) The uncertainty in setting the target angle ($\pm$ 0.75°). This error is less than 1.0%. The values of the absolute errors are shown in Table 6.

The toal absolute error is obtained by adding the above errors in quadrature.

Table 5

Relative Errors

Yield Statistics	$\leq$ 1.0 %
Dead Time Correction	< 1.0% Forward Angles $\sim$ 0.2% Backward Angles
Reactions in NaI(Tℓ)	< 0.1 %
Finite Geometry	< 0.3 %
Detector Angle	$\leq$ 1.0 %
Incident Proton Energy	$\leq$ 1.5 %
Impurity Subtraction	$\sim$ 2.0 %

Table 6

Absolute Errors

Solid Angle	$\sim$ 1.0 %
Target Angle	< 1.0 %
Target Thickness	Chap.III table 4
Beam Current Integration	1.0%

A recent measurement of the ratios of the differential cross sections for the calcium isotopes has been reported by Austin et al.[40] at 30.3 MeV. Linear interpolations in energy and angle were made for the present differential cross sections to match those of Austin et al. The ratios of the differential cross sections were then calculated and compared with the measured ratios[40]. An average deviation of $\pm$ 1.3% per data point was noticed between the two sets of data, which is consistent with the experimental uncertainties (1.0 - 5.0%) quoted by Austin et al.

A comparison of the measurements on ^{40}Ca at 27.5, 30.0, 35.0, 40.0 and 45.0 MeV is made with previous measurements by Ridley at 27.4 MeV[41], Ridley et al. at 30.3 MeV[42], Gross et al. at 35.8 and 45.5 MeV[43], Blumberg et al. at 40.0 MeV[44] and are shown in Figs. 7 to 11. One can see from these comparisons that there are no appreciable differences between the shapes and the phases of the oscillations of the present results and of the previous measurements of the differential cross section angular distribution at these five energies. However, at 40.0 MeV a slight discrepancy in the backward hemisphere can be noticed between the present result and that of Blumberg et al.[44]. This discrepancy is probably due to an energy difference between the two measurements.

Numerical values of the elastic scattering differential cross sections are given in the tables of Appendix 1.

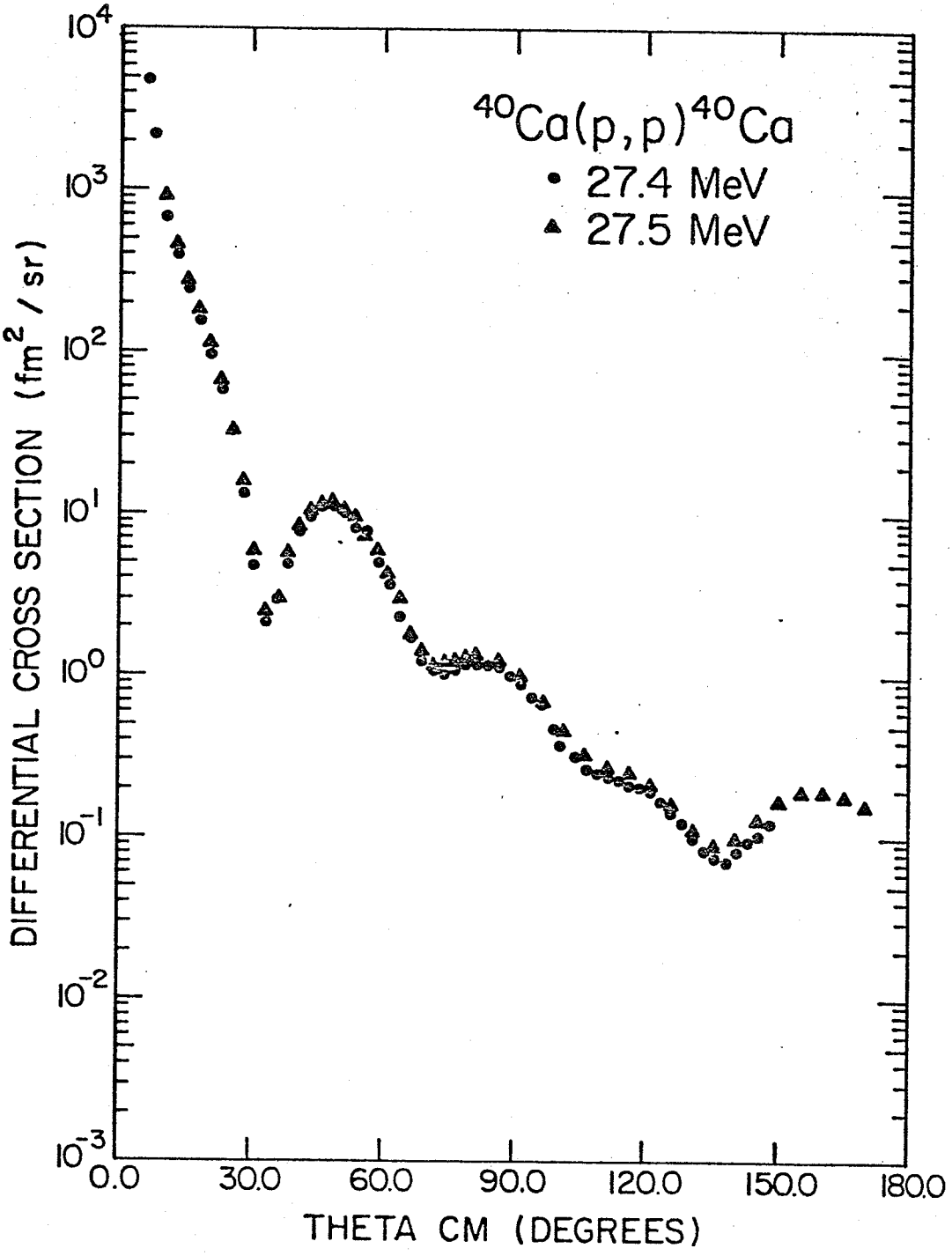
$^{40}Ca(p,p)^{40}Ca$
• 27.4 MeV
▲ 27.5 MeV
DIFFERENTIAL CROSS SECTION (fm²/sr)
THETA CM (DEGREES)
10⁴
10³
10²
10¹
10⁰
10⁻¹
10⁻²
10⁻³
0.0
30.0
60.0
90.0
120.0
150.0
180.0

Fig. 7

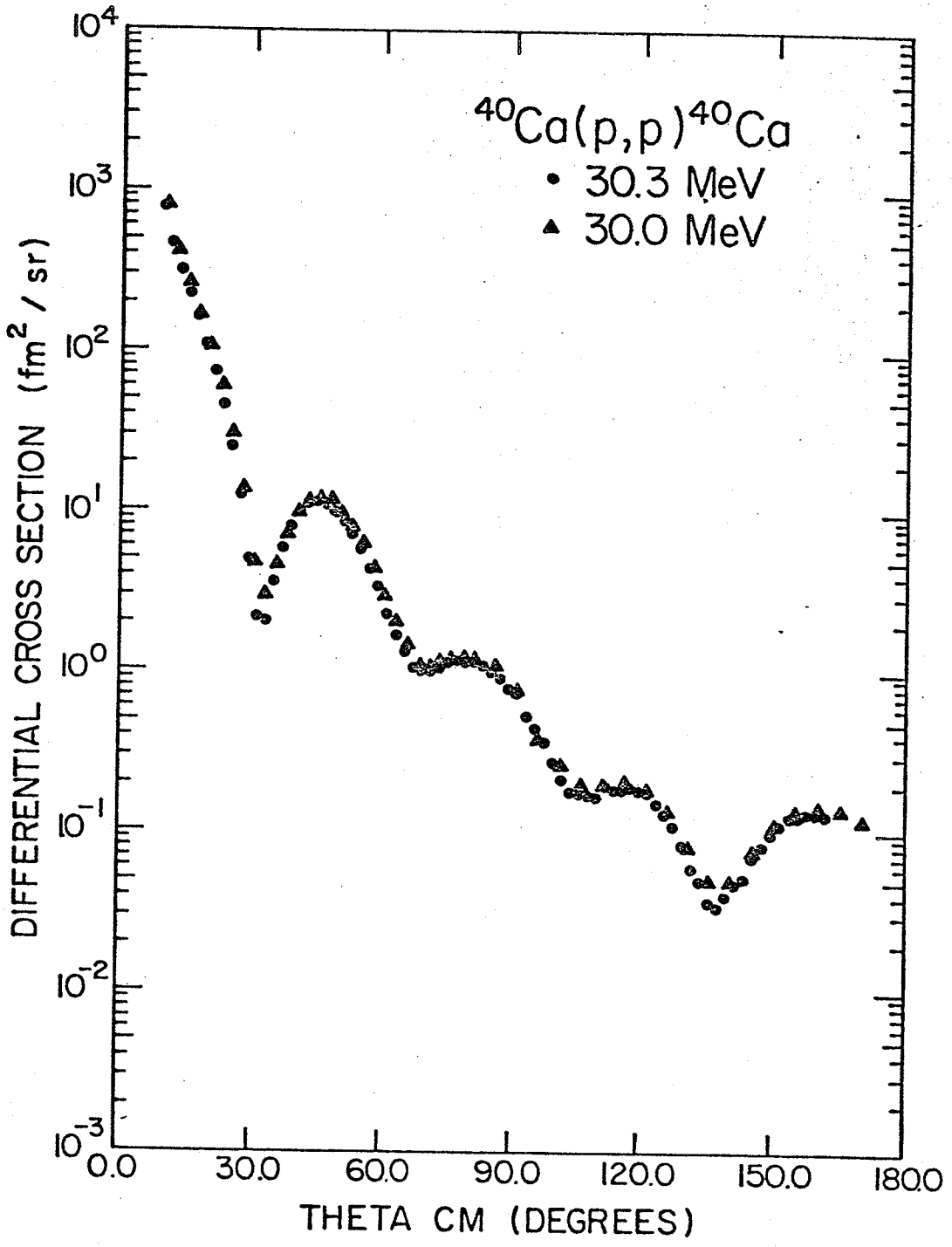
$^{40}Ca(p,p)^{40}Ca$
• 30.3 MeV
▲ 30.0 MeV
DIFFERENTIAL CROSS SECTION (fm² / sr)
THETA CM (DEGREES)
10⁴
10³
10²
10¹
10⁰
10⁻¹
10⁻²
10⁻³
0.0
30.0
60.0
90.0
120.0
150.0
180.0

Fig.8

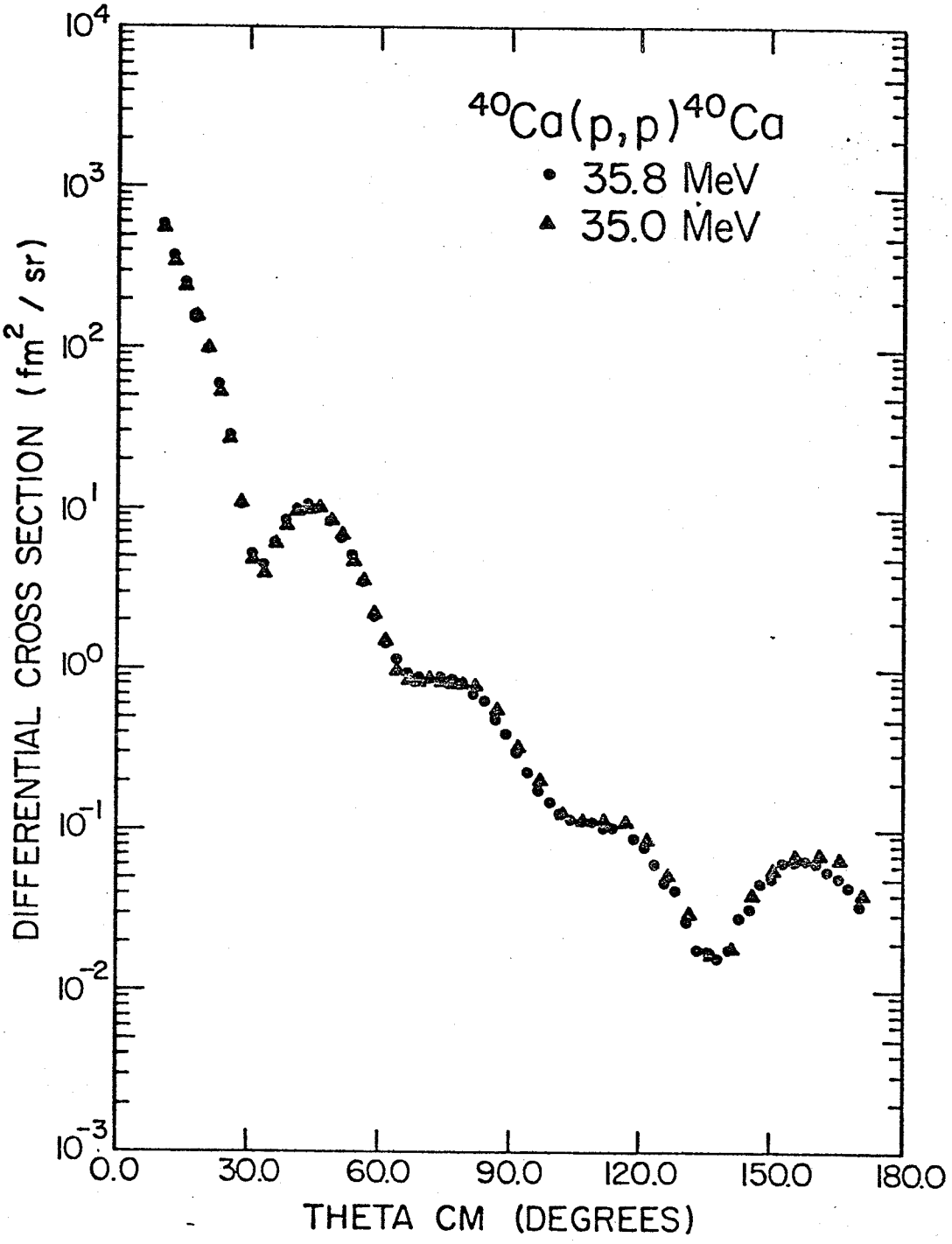
$^{40}Ca(p,p)^{40}Ca$
• 35.8 MeV
▲ 35.0 MeV
DIFFERENTIAL CROSS SECTION (fm² / sr)
THETA CM (DEGREES)
10⁴
10³
10²
10¹
10⁰
10⁻¹
10⁻²
10⁻³
0.0
30.0
60.0
90.0
120.0
150.0
180.0

Fig. 9

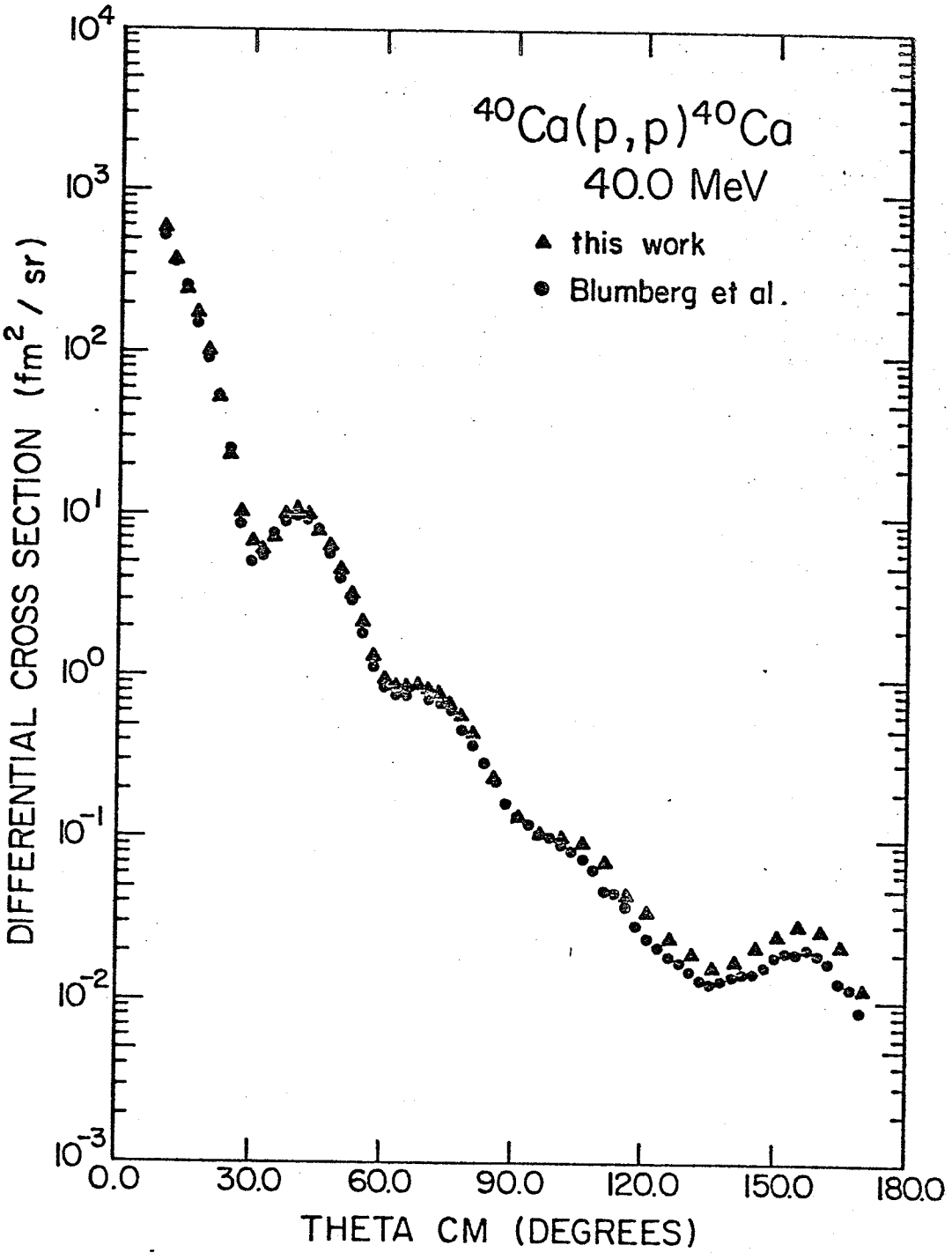
$^{40}Ca(p,p)^{40}Ca$
40.0 MeV
this work
Blumberg et al.
DIFFERENTIAL CROSS SECTION (fm^2 / sr)
10^4
10^3
10^2
10^1
10^0
10^{-1}
10^{-2}
10^{-3}
0.0
30.0
60.0
90.0
120.0
150.0
180.0
THETA CM (DEGREES)

Fig. 10

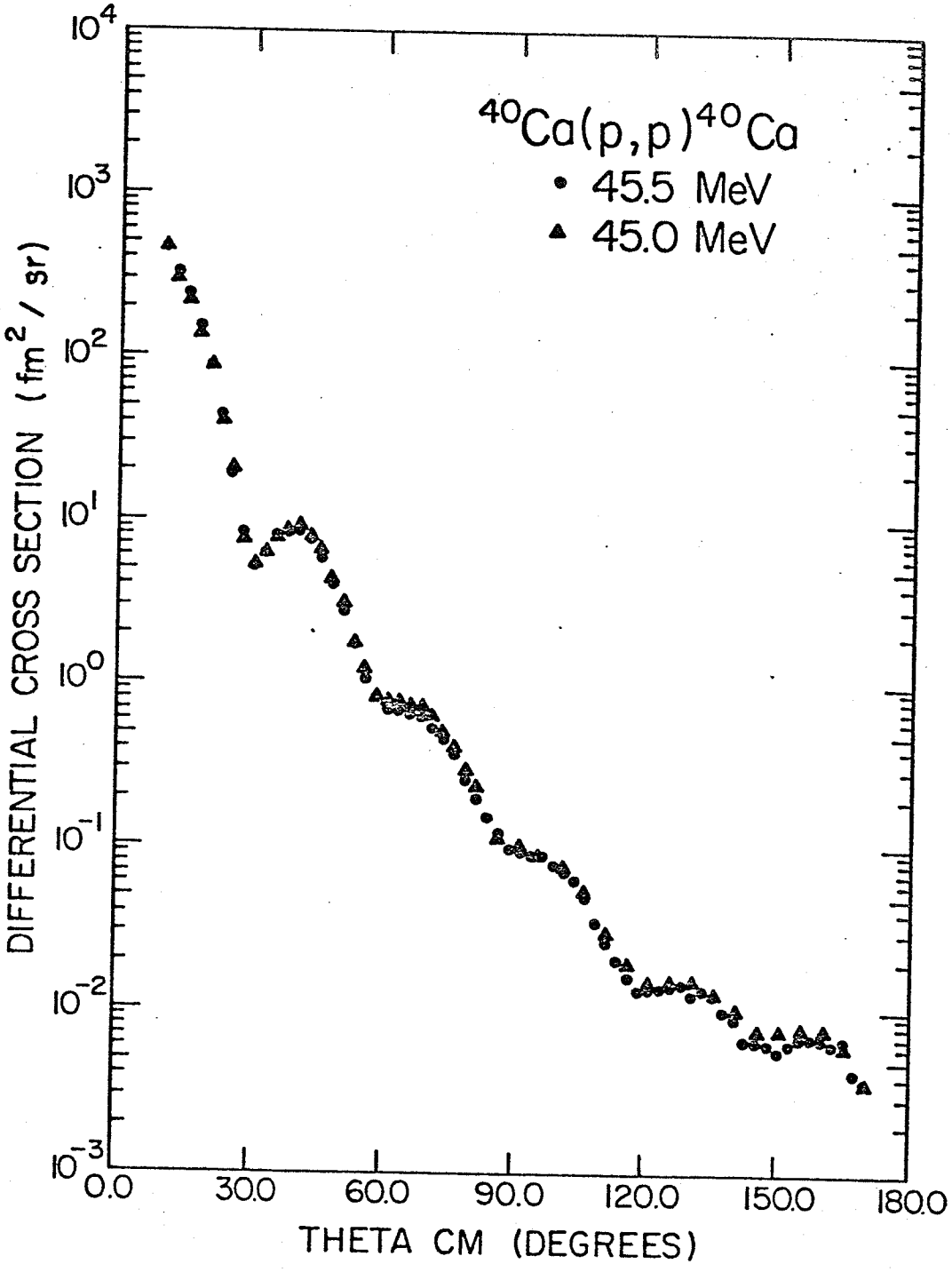
$^{40}Ca(p,p)^{40}Ca$
• 45.5 MeV
▲ 45.0 MeV
DIFFERENTIAL CROSS SECTION (fm²/sr)
10^4
10^3
10^2
10^1
10^0
10^{-1}
10^{-2}
10^{-3}
0.0
30.0
60.0
90.0
120.0
150.0
180.0
THETA CM (DEGREES)

Fig. 11

IV.3 Optical Model Analysis

The form of the optical model potential used in the analysis of the data is as described in Chapter II and given by equation (9). The optical model analysis is performed using the automatic search code SEEK[45] in a modified version which has the ability to handle the elastic scattering differential cross section and analyzing power data at different sets of angles, to vary independently the geometrical parameters of the spin-orbit term, to use a derivative Woods-Saxon form factor for the surface absorption term of the imaginary central potential, and to allow as a maximum number of partial waves 46 (previously 30) and finally to contain an explicit ℓ-dependent Woods-Saxon term.

The program permits searches to be made over the nuclear optical model parameter space to yield optimum fits to the differential elastic scattering cross sections, analyzing powers and total reaction cross section.

The data included in the analysis are the differential cross section angular distributions given in the Appendix together with proton elastic scattering differential cross section data on ^{40}Ca at 21.0, 23.5, 26.3 and 48.0 MeV measured by van Oers et al.[6], and the analyzing power data available in the literature for protons scattered by ^{40}Ca at 21.0[46], 26.3[47], 30.0[48], 35.0[43], 40.0[44], 45.0[43] and 48.0[49] MeV.

Starting with the optical model parameters of van Oers[50], subsequent searches were made over the real central potential parameters, the imaginary volume and imaginary surface potential parameters, the spin orbit potential parameters and the ℓ-dependent potential parameters. Finally, all parameter searches were made to obtain the best fit to the experimental data. The above cycle was repeated if necessary. For a fit to be acceptable the optical model parameters found must exhibit a reasonable continuity as a function of incident proton energy and the calculated total reaction cross sections must agree

reasonably well with the experimental values, when available. At those energies for which analyzing power data were available, searches were performed for best simultaneous fits to both differential cross section and analyzing power data. This was accomplished by minimizing the sum of the χ^2 for the differential cross sections, χ^2_σ, and the χ^2 for the analyzing power data, χ^2_p.

After an optimum set of parameters was obtained a search on the imaginary spin orbit potential strength, W_s, by itself and subsequently with all other parameters gave a very small value for W_s ($\sim$ 0.01 MeV) which did not improve the fits appreciably (a change of $\chi^2_\sigma + \chi^2_p$ from 920 to 919) for p+^{40}Ca at 40.0 MeV. Consequently the value of W_s was set equal to zero at all energies. This reduced the number of free parameters in the optical potential to thirteen.

The Coulomb radius parameter, r_c, is taken to be 1.316, 1.306 and 1.285 fm for ^{40}Ca, ^{42}Ca and ^{44}Ca, respectively, as determined from electron scattering experiments[10].

The optical model parameters which give the best fits to the experimental data are shown in Tables 7, 8 and 9 for ^{40}Ca, ^{42}Ca and ^{44}Ca, respectively. The quantities given are the dynamical and geometrical parameters defined in Chapter II, Section 1. The theoretical total reaction cross section σ_r^{th} and χ^2_σ/N_σ, the χ^2 value per data point, where χ^2_σ is the total χ^2 for the differential cross section data. The corresponding quantity for the analyzing powers χ^2_p/N_p and the experimental total reaction cross section σ_r^{exp} are given only in Table 7 for ^{40}Ca where they are available.

The best fits obtained for the differential cross section and analyzing power angular distributions are shown in Figs. 12 to 18 and in Figs. 19 to 20, respectively.

Table 7

Best Fit Optical Model Parameters for p + ^{40}Ca

T_p (MeV)	V (MeV)	r_o (fm)	a_o (fm)	W (MeV)	W_I (MeV)	r_I (fm)	a_I (fm)	V_{so} (MeV)	r_{so} (fm)	a_{so} (fm)	V_{ex} (MeV)	r_{ex} (fm)	a_{ex} (fm)	$\frac{\chi^2_\sigma}{N_\sigma}$	$\frac{\chi^2_p}{N_p}$	σ_r^{th} (fm^2)	σ_r^{exp} (fm^2)
21.0	52.14	1.155	0.747	(0.0)	7.85	1.265	0.541	3.19	0.959	0.558	0.009	1.001	0.302	22.7	7.7	91.9	
23.5	48.84	1.176	0.734	(0.0)	7.38	1.204	0.591	4.24	1.076	0.557	-0.650	0.844	0.709	30.3	-	90.9	
25.0	46.56	1.189	0.719	(0.0)	6.46	1.243	0.572	4.28	1.075	0.559	-1.215	0.877	0.733	13.5	-	85.8	87.6 ± 3.3
26.3	48.95	1.154	0.755	0.69	5.49	1.272	0.644	3.50	1.076	0.562	-1.319	0.873	0.373	8.3	42.4	91.9	
27.5	47.49	1.149	0.765	0.21	4.81	1.254	0.742	5.38	1.176	0.593	-0.088	0.976	0.311	8.1	-	90.7	91.5 ± 3.0
30.0	45.19	1.180	0.704	(0.0)	4.97	1.296	0.727	5.34	1.076	0.706	0.234	0.908	0.364	12,0	17.8	90.3	88.0 ± 2.6
35.0	47.85	1.119	0.749	2.14	4.59	1.384	0.586	7.29	0.976	0.763	0.498	0.971	0.430	18.1	17.5	88.8	85.4 ± 2.5
40.0	46.31	1.115	0.793	4.22	1.69	1.503	0.542	4.99	1.016	0.591	0.110	1.040	0.730	12.9	6.5	83.1	80.7 ± 2.4
45.0	45.86	1.119	0.780	4.87	0.05	1.663	0.296	6.19	0.995	0.732	-0.025	0.969	0.302	7.9	4.3	76.4	77.8 ± 2.3
48.0	40.77	1.179	0.703	5.82	0.12	1.561	0.559	5.69	0.983	0.791	-0.015	0.796	0.281	27.8	15.3	80.7	76.9 ± 2.2

Table 8

Best Fit Optical Model Parameters for p + ^{42}Ca

T_p (MeV)	V (MeV)	r_o (fm)	a_o (fm)	W (MeV)	W_I (MeV)	r_I (fm)	a_I (fm)	V_{so} (MeV)	r_{so} (fm)	a_{so} (fm)	V_{ex} (MeV)	r_{ex} (fm)	a_{ex} (fm)	$\frac{\chi^2_\sigma}{N_\sigma}$	σ_r^{th} (fm^2)
21.0	55.57	1.112	0.764	(0.0)	8.13	1.266	0.621	3.85	1.066	0.660	-0.008	0.844	0.124	11.2	103.1
25.0	45.78	1.193	0.715	(0.0)	6.58	1.239	0.683	4.29	0.989	0.634	-0.775	1.097	0.361	14.2	99.6
30.0	46.23	1.148	0.759	2.04	3.80	1.405	0.723	3.63	1.020	0.579	-0.032	0.761	0.352	10.9	103.7
35.0	46.49	1.109	0.768	1.76	5.81	1.373	0.517	7.67	1.031	0.800	0.471	0.907	0.339	5.7	89.1
40.0	42.98	1.152	0.758	5.08	0.20	1.511	0.460	6.12	0.914	0.759	0.173	0.865	0.336	15.1	84.4
45.0	42.84	1.146	0.758	5.06	0.63	1.615	0.414	5.60	1.005	0.711	-0.011	0.972	0.266	7.1	83.8
48.4	40.34	1.168	0.722	5.75	0.76	1.496	0.586	5.61	0.980	0.790	-0.015	0.795	0.330	14.2	83.4

Table 9

Best Fit Optical Model Parameters for p + ^{44}Ca

T_p (MeV)	V (MeV)	r_o (fm)	a_o (fm)	W (MeV)	W_I (MeV)	r_I (fm)	a_I (fm)	V_{so} (MeV)	r_{so} (fm)	a_{so} (fm)	V_{ex} (MeV)	r_{ex} (fm)	a_{ex} (fm)	$\frac{\chi^2_\sigma}{N_\sigma}$	σ_r^{th} (fm^2)
21.0	52.86	1.142	0.722	(0.0)	8.87	1.286	0.602	6.16	1.047	0.791	0.032	0.901	0.228	17.5	106.7
25.0	51.84	1.143	0.718	(0.0)	8.17	1.266	0.618	8.74	0.876	0.817	-0.564	0.837	0.337	20.2	103.2
30.0	44.91	1.162	0.762	2.53	3.44	1.397	0.723	3.86	1.193	0.588	-0.033	0.829	0.337	5.6	105.4
35.0	45.83	1.127	0.759	1.80	4.95	1.382	0.609	7.76	0.951	0.798	0.066	0.951	0.307	3.5	97.0
40.0	46.63	1.098	0.814	4.98	0.25	1.634	0.458	7.11	0.885	0.739	0.087	0.908	0.364	10.0	89.2
45.0	43.65	1.133	0.776	4.79	1.67	1.524	0.443	5.83	0.987	0.727	-0.009	0.971	0.275	3.9	85.3
48.4	42.81	1.144	0.737	5.75	0.78	1.495	0.587	5.31	0.980	0.799	0.057	0.967	0.302	4.9	86.3

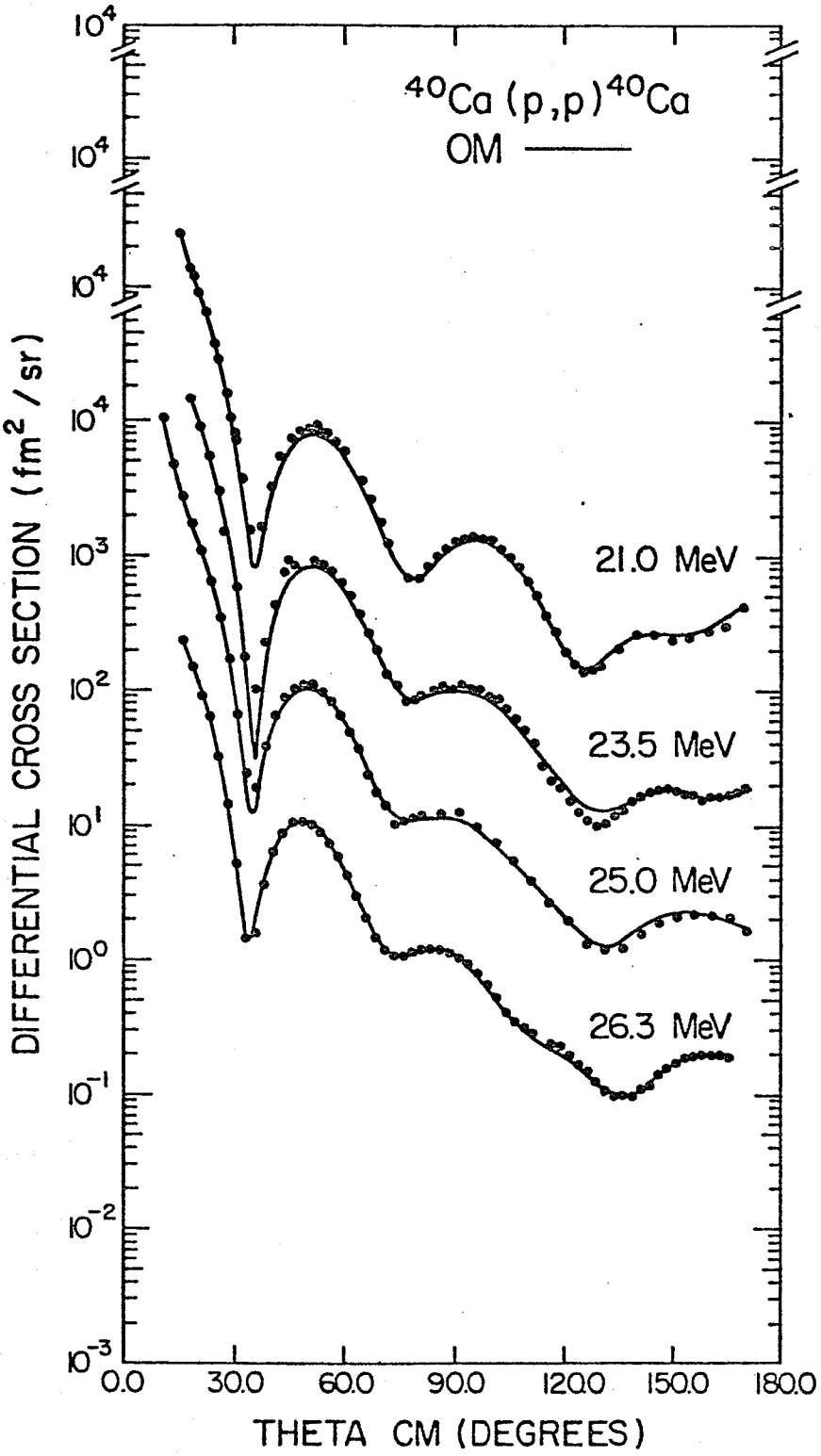
$^{40}Ca\,(p,p)^{40}Ca$
OM
21.0 MeV
23.5 MeV
25.0 MeV
26.3 MeV
DIFFERENTIAL CROSS SECTION (fm²/sr)
THETA CM (DEGREES)
0.0
30.0
60.0
90.0
120.0
150.0
180.0

Fig. 12

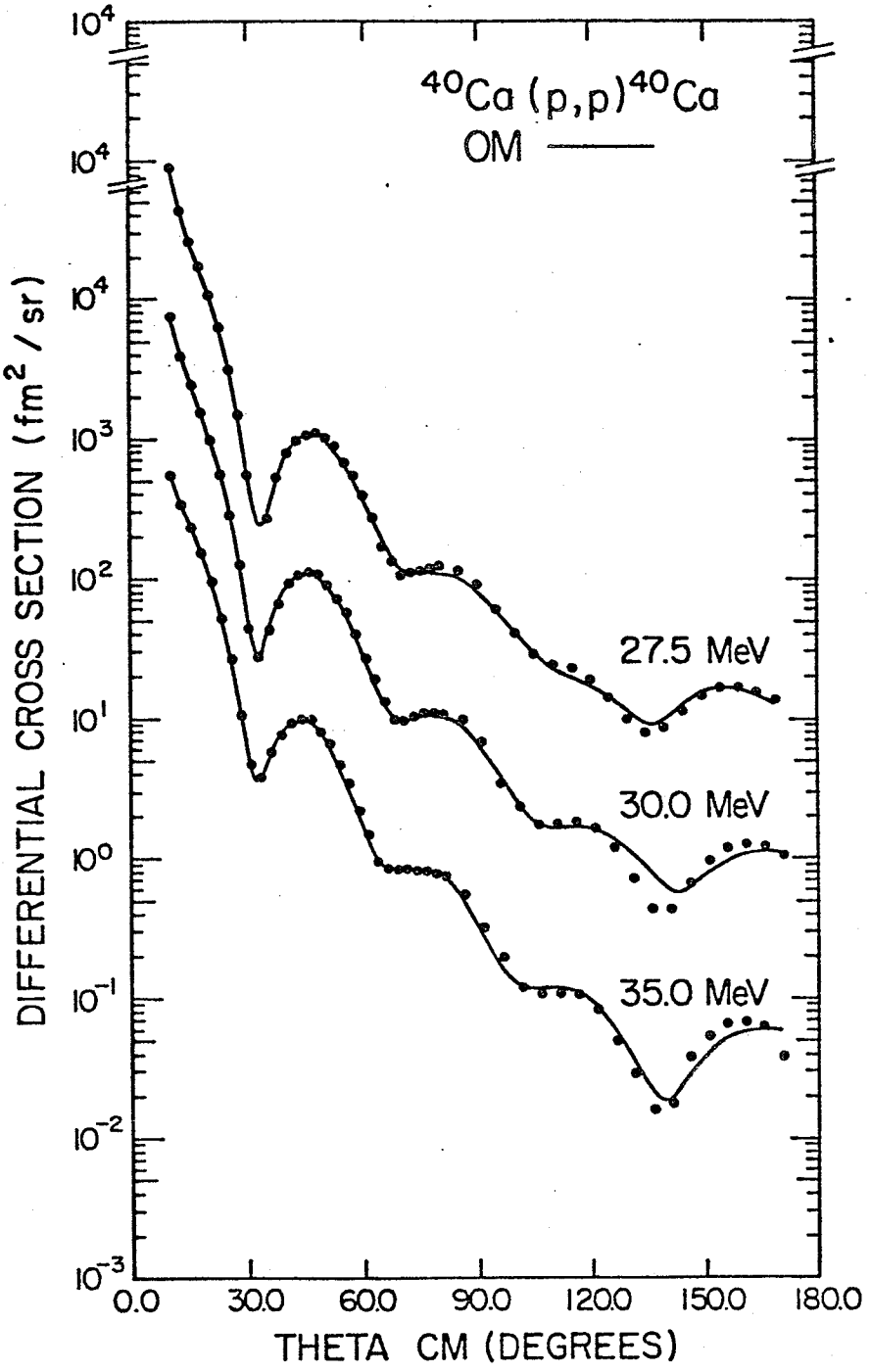
$^{40}Ca\,(p,p)^{40}Ca$
OM
27.5 MeV
30.0 MeV
35.0 MeV
DIFFERENTIAL CROSS SECTION (fm^2 / sr)
THETA CM (DEGREES)
10^4
10^4
10^4
10^3
10^2
10^1
10^0
10^{-1}
10^{-2}
10^{-3}
0.0
30.0
60.0
90.0
120.0
150.0
180.0

Fig. 13

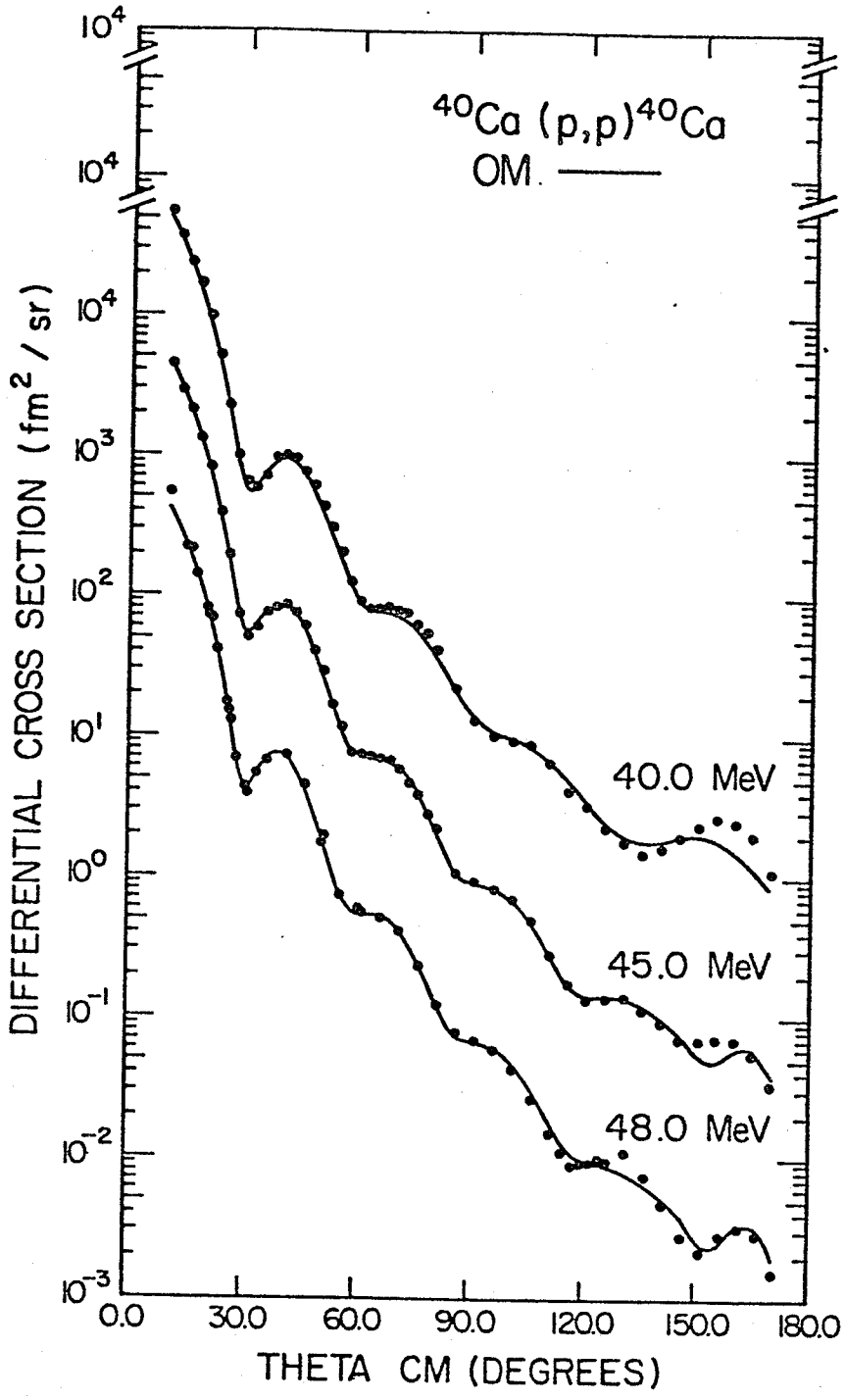
$^{40}Ca\ (p,p)^{40}Ca$
OM
40.0 MeV
45.0 MeV
48.0 MeV
DIFFERENTIAL CROSS SECTION (fm^2 / sr)
THETA CM (DEGREES)
10^4
10^3
10^2
10^1
10^0
10^{-1}
10^{-2}
10^{-3}
0.0
30.0
60.0
90.0
120.0
150.0
180.0

Fig. 14

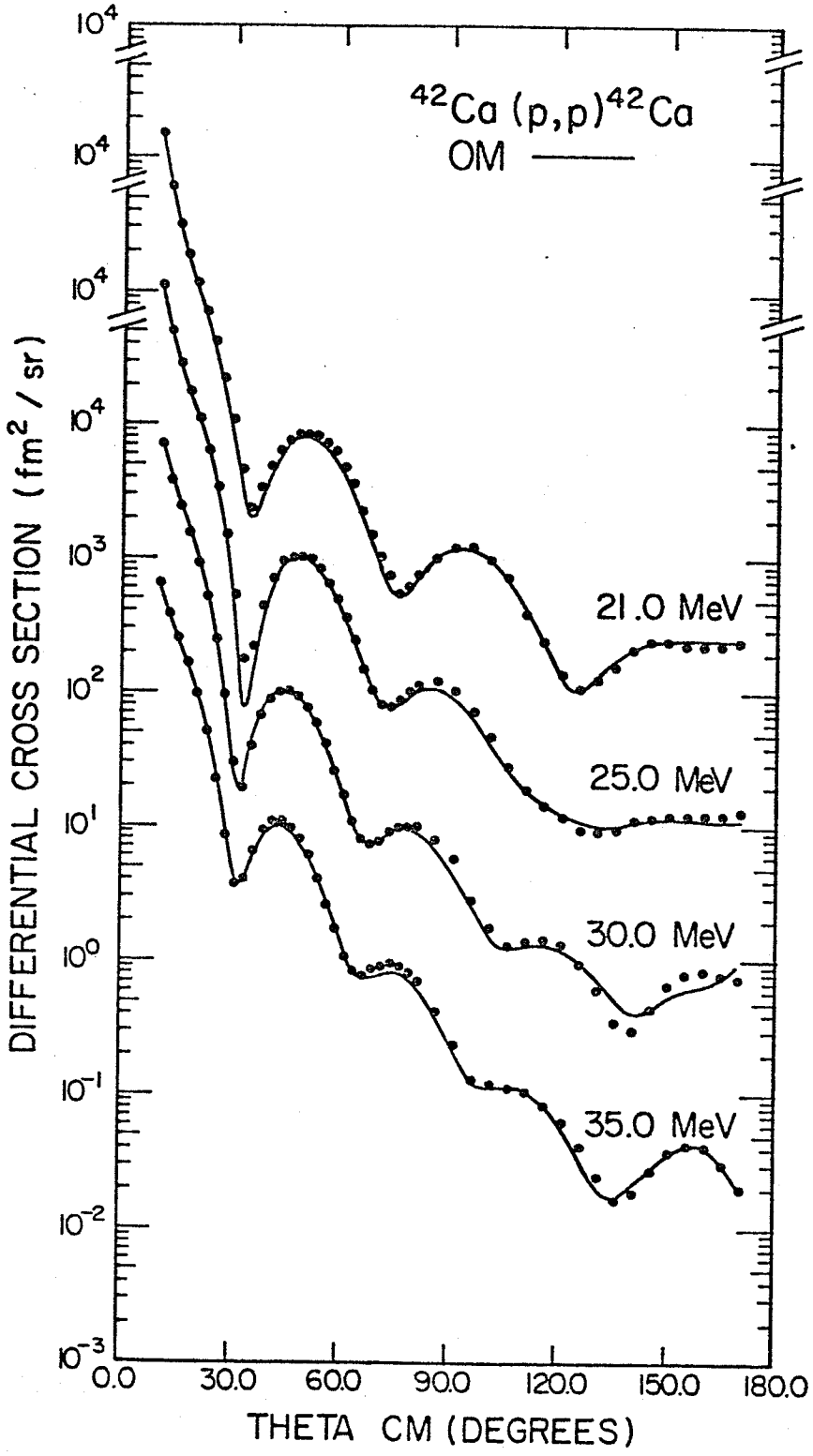
^{42}Ca (p,p)^{42}Ca
OM
21.0 MeV
25.0 MeV
30.0 MeV
35.0 MeV
DIFFERENTIAL CROSS SECTION (fm^2 / sr)
THETA CM (DEGREES)
10^4
10^4
10^4
10^3
10^2
10^1
10^0
10^{-1}
10^{-2}
10^{-3}
0.0
30.0
60.0
90.0
120.0
150.0
180.0

Fig. 15

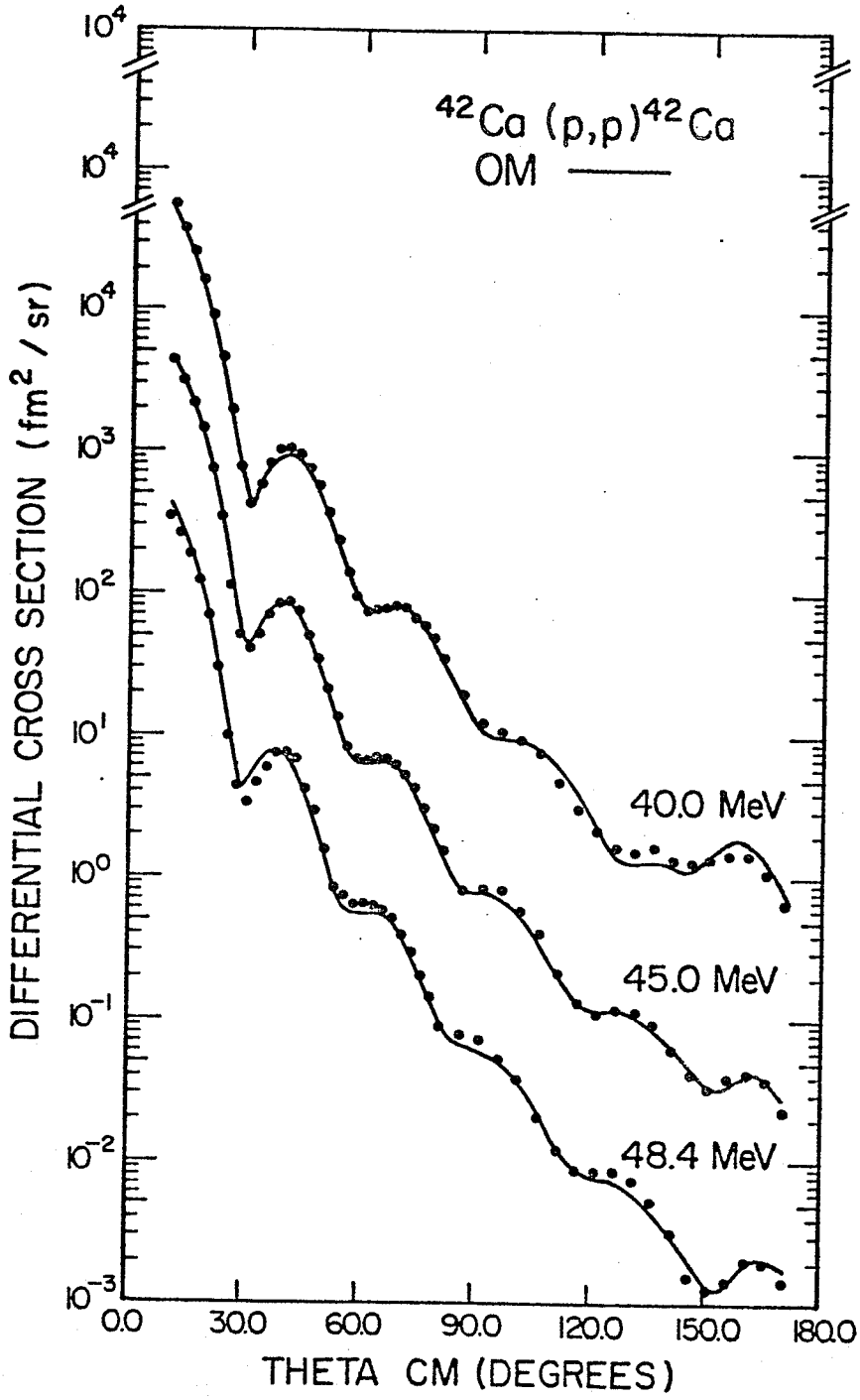
^{42}Ca (p,p)^{42}Ca
OM
40.0 MeV
45.0 MeV
48.4 MeV
DIFFERENTIAL CROSS SECTION (fm^2 / sr)
THETA CM (DEGREES)
0.0
30.0
60.0
90.0
120.0
150.0
180.0

Fig. 16

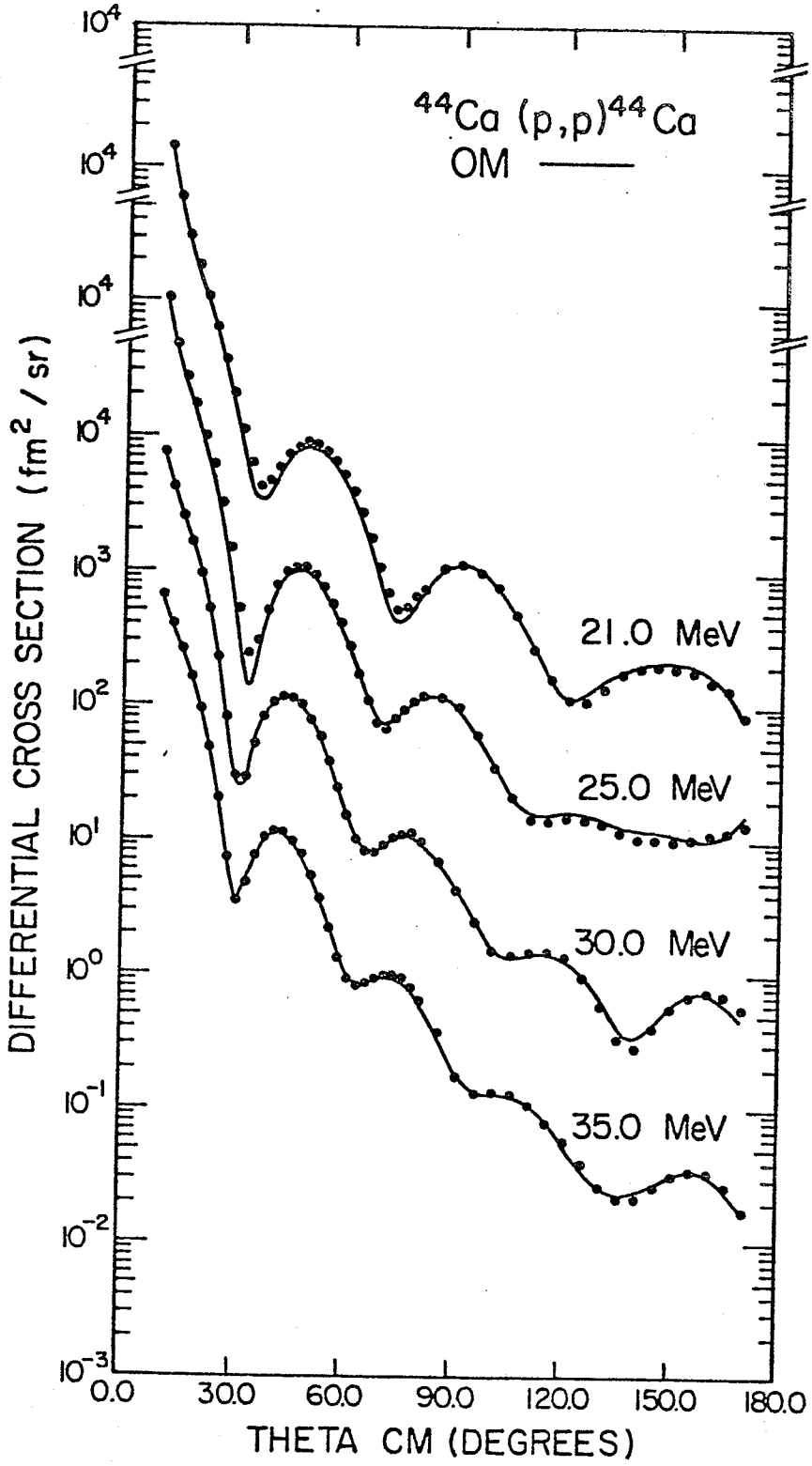
^{44}Ca (p,p)^{44}Ca
OM
21.0 MeV
25.0 MeV
30.0 MeV
35.0 MeV
DIFFERENTIAL CROSS SECTION (fm^2 / sr)
THETA CM (DEGREES)
10^4
10^4
10^4
10^3
10^2
10^1
10^0
10^{-1}
10^{-2}
10^{-3}
0.0
30.0
60.0
90.0
120.0
150.0
180.0

Fig. 17

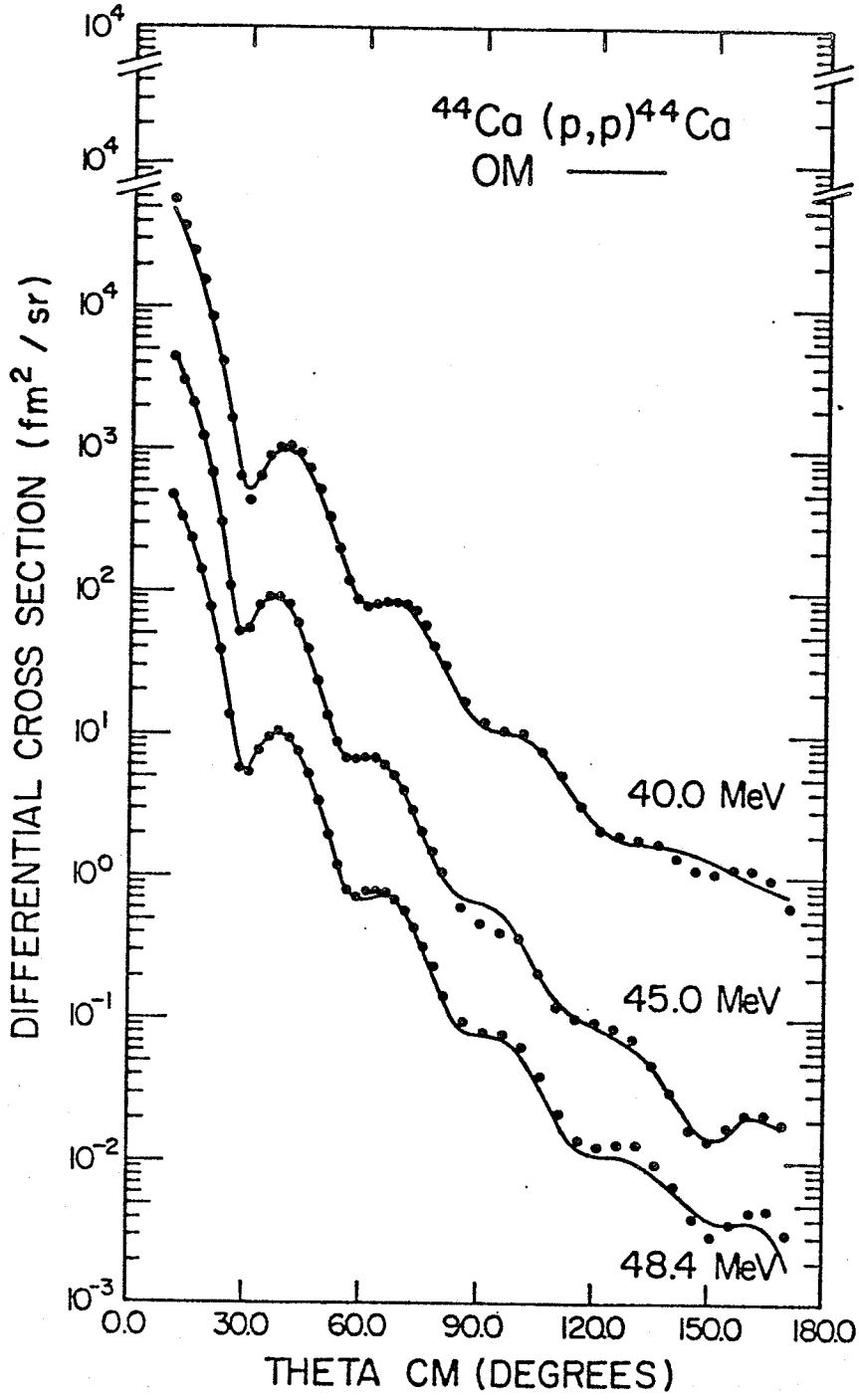
^{44}Ca (p,p)^{44}Ca
OM
40.0 MeV
45.0 MeV
48.4 MeV
DIFFERENTIAL CROSS SECTION (fm^2 / sr)
THETA CM (DEGREES)
10^4
10^4
10^4
10^3
10^2
10^1
10^0
10^{-1}
10^{-2}
10^{-3}
0.0
30.0
60.0
90.0
120.0
150.0
180.0

Fig. 18

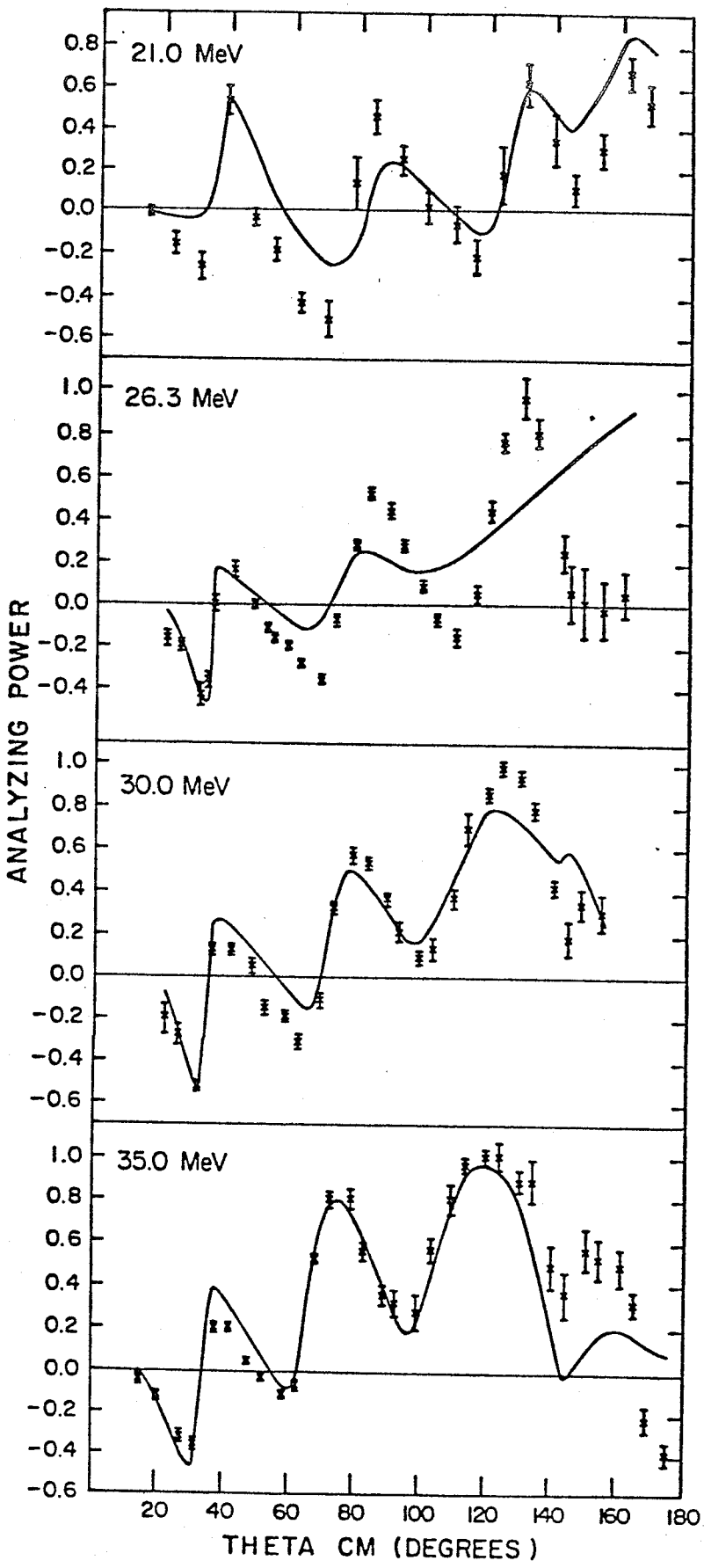
21.0 MeV
26.3 MeV
30.0 MeV
35.0 MeV
ANALYZING POWER
THETA CM (DEGREES)

Fig. 19

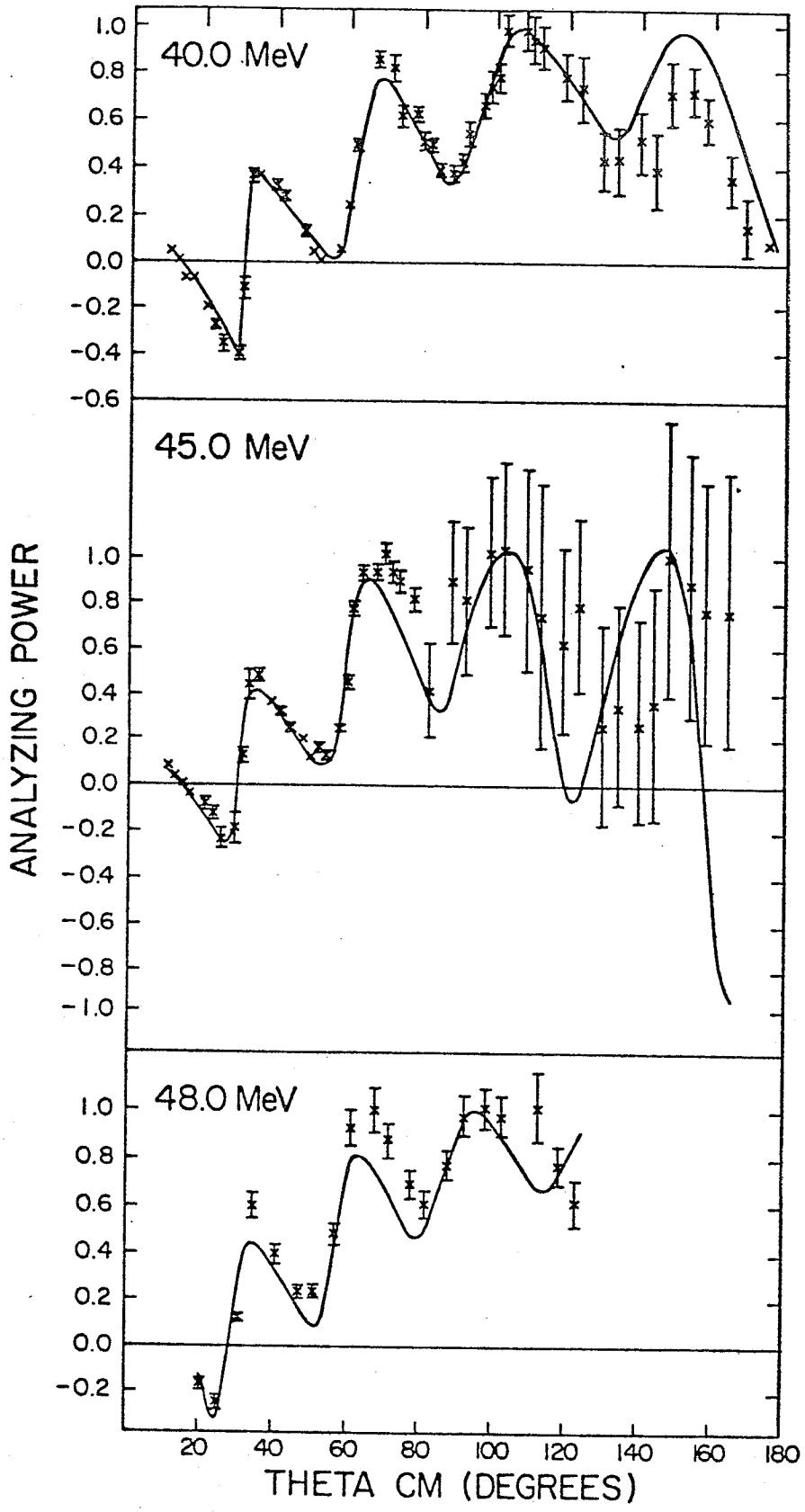

Fig. 20

In general, the quality of the fits to the differential cross section and analyzing power angular distributions is quite good. The introduction of an explicit ℓ-dependent term into the standard optical potential certainly improves the fits at the back angles of most of the angular distributions if compared with previous analyses[42]. Some discrepancies can be noticed at the extreme backward angles at 30.0, 40.0 and 45.0 MeV for ^{40}Ca, at 30.0 and 40.0 MeV for ^{42}Ca and at 40.0 and 48.4 MeV for ^{44}Ca. This suggests that there is still room for refinements of the optical model potential. The fit to the analyzing power angular distribution at 26.3 MeV is reasonable for angles up to 100° c.m., beyond which the quality of the fit starts to deteriorate if compared with the fits to the analyzing power angular distributions at the other energies.

The r.m.s. radii of the real central potential are calculated using equation (14) of Chapter II, using the best fit optical model parameters given in Tables 7, 8 and 9. The calculated r.m.s. radii are shown in Tables 10, 11 and 12 for ^{40}Ca, ^{42}Ca and ^{44}Ca, respectively. Also shown in the last column of the tables is the volume integral per nucleon of the real central potential. This is calculated as follows:

$$J/A = \frac{1}{A} \int V(r)\, d^3r$$

$$= \frac{V_o}{A} \int \frac{4\pi r^2}{\left(1 + \exp \frac{r - r_o}{a_o}\right)} dr \quad , \quad \text{or}$$

$$J/A \approx \frac{4\pi V_o}{3} r_o^3 \left(1 + \frac{\pi^2 a_o^2}{r_o^2 A^{2/3}}\right) \qquad (18)$$

In Tables 10, 11 and 12 one can notice that the real central r.m.s. radii obtained in these analyses are independent of energy as expected. The results of the volume integral per nucleon of the real central potential suggest a gradual decrease in these integrals with increasing incident energy. The volume integral per nucleon is plotted as a function of energy for the three isotopes under consideration in Fig. 21.

Since, for the purpose of this work, one is mainly interested in the real central potential parameters, the effect on the real central parameters of including the analyzing power data have been examined. This is done by first of all fitting the differential cross section data alone and allowing the spin orbit parameters to vary. Later, fits to the differential cross section and analyzing power data are made. The r.m.s. radii of the real central potential with and without analyzing power data included in the analysis are compared in Table 13. It can be seen that the r.m.s. radii are not appreciably affected by including the analyzing power data in the analysis.

An effort was made to further investigate the energy dependence of the depth of the ℓ-dependent potential, V_{ex}. The analysis was carried out keeping the geometrical parameters of this potential fixed to values independent of energy. The fixed geometrical parameters (r_{ex} and a_{ex}) were obtained by averaging over the optimum parameters given in Tables 7, 8 and 9. The quality of the fits to the experimental data and the values of the remaining parameters were not appreciably affected. For instance, an increase in χ^2_{tot} ($\chi^2_\sigma + \chi^2_p$) by about 1% and a change of less than 0.3% in the real central potential parameters were noticed for ^{40}Ca at 21.0 MeV. The values of V_{ex} as a function of energy are shown in table 14 and plotted in Fig. 22 for the three calcium isotopes ^{40}Ca, ^{42}Ca and ^{44}Ca. A smooth line has been drawn through the ^{40}Ca data points to guide the eye and has no further significance. One can see the oscillatory

Table 10

r.m.s. radii and Volume Integral per Nucleon for p + ^{40}Ca

T_p (MeV)	r.m.s. radius (fm)	J/A (MeV. fm^3)
21.0	4.131	455.3
23.5	4.142	442.1
25.0	4.120	429.0
26.3	4.148	428.4
27.5	4.164	414.7
30.0	4.077	404.5
35.0	4.067	387.1
40.0	4.173	383.7
45.0	4.146	379.6
48.4	4.071	363.6

Table 11

r.m.s. radii and Volume Integral per Nucleon for p + ^{42}Ca

T_p (MeV)	r.m.s. radius (fm)	J/A (MeV. fm^3)
21.0	4.128	443.5
25.0	4.169	421.2
30.0	4.185	397.6
35.0	4.133	369.7
40.0	4.191	372.6
45.0	4.179	366.6
48.4	4.135	358.9

Table 12

r.m.s. radii and Volume Integral per Nucleon for p + ^{44}Ca

T_p (MeV)	r.m.s. radius (fm)	J/A (MeV. fm^3)
21.0	4.116	434.2
25.0	4.108	425.6
30.0	4.257	395.7
35.0	4.178	373.5
40.0	4.262	371.1
45.0	4.233	364.7
48.4	4.158	356.8

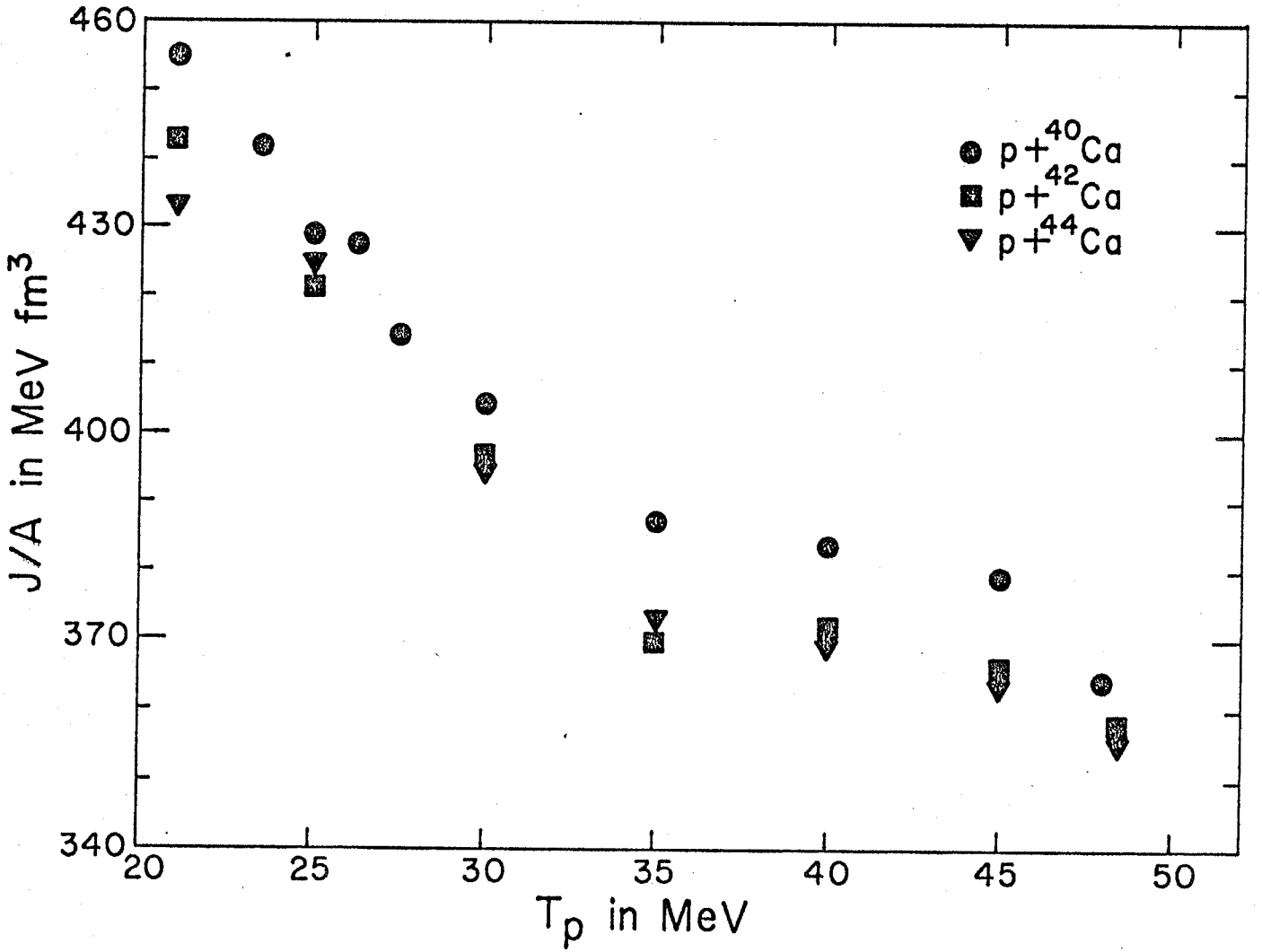
460
430
400
370
340
J/A in MeV fm^3
20
25
30
35
40
45
50
T_p in MeV
p+^{40}Ca
p+^{42}Ca
p+^{44}Ca

Fig. 21

Table 13

Comparison of the r.m.s. radii of the Real Central Potential With and Without Analyzing Power Data Included in the Analses of ^{40}Ca

T_p (MeV)	r.m.s. radius with P(θ)	r.m.s. radius without P(θ)
21.0	4.131	4.116
26.3	4.148	4.131
30.0	4.077	4.117
35.0	4.067	4.067
40.0	4.173	4.171
45.0	4.146	4.174
48.0	4.071	4.076
	$\overline{< r^2_{opt} >}^{1/2}$	$< r^2_{opt} >^{1/2}$
	$= 4.116 \pm 0.016$ fm	$= 4.122 \pm 0.016$ fm

Table 14

Variation of V_{ex} with Energy

a_{ex} = 0.366 fm r_{ex} = 0.911 fm

T_p (MeV)	V_{ex}(MeV)		
	^{40}Ca	^{42}Ca	^{44}Ca
21.0	0.067	-0.066	-0.287
23.5	-0.606		
25.0	-1.43	-1.05	-0.740
26.3	-1.05		
27.5	0.119		
30.0	0.403	-0.256	-0.199
35.0	0.556	0.523	0.240
40.0	0.109	0.247	0.087
45.0	0.028	0.027	-0.022
48.0	0.017	0.002	-0.042

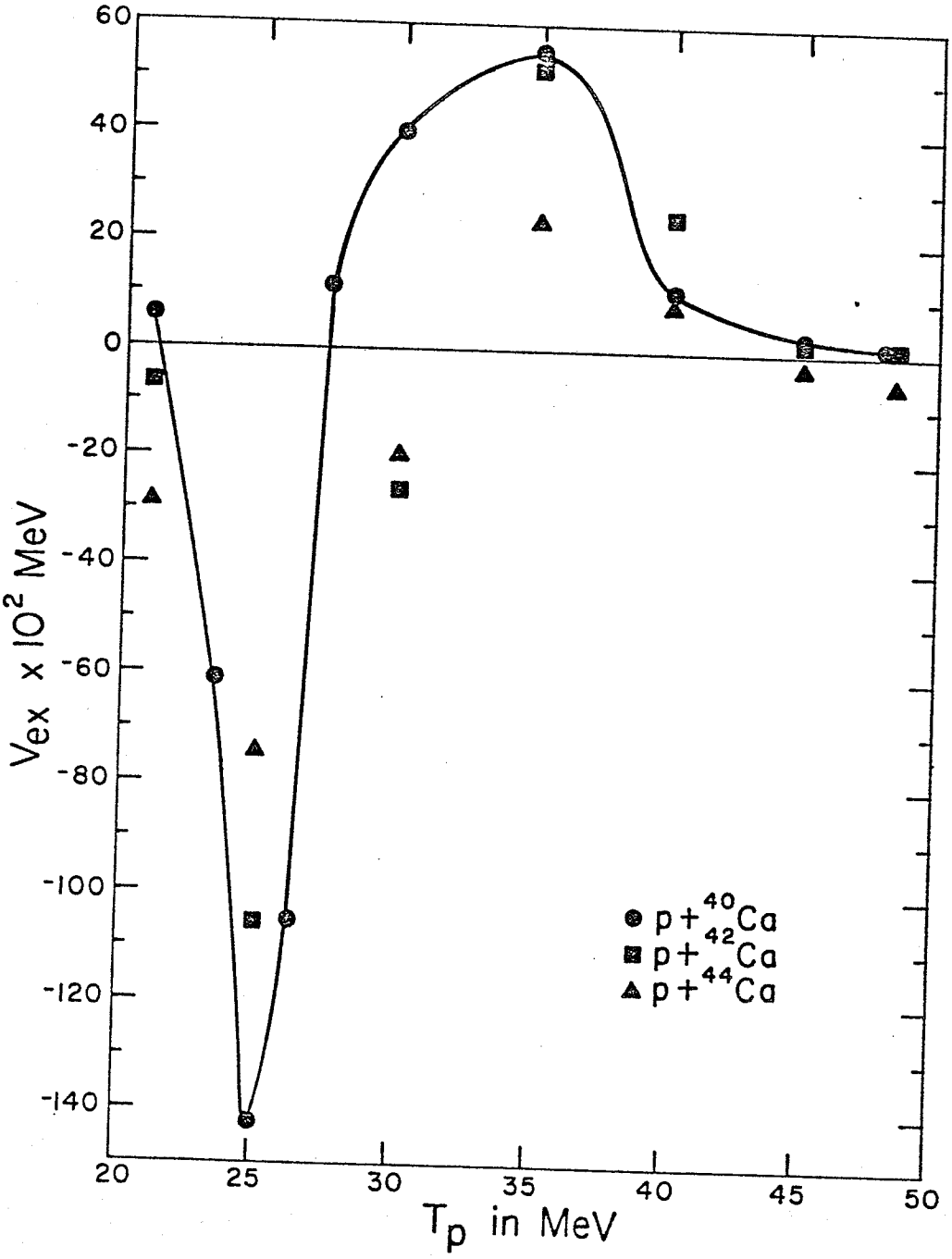
60
40
20
0
-20
-40
-60
-80
-100
-120
-140
$V_{ex} \times 10^2$ MeV
20
25
30
35
40
45
50
T_p in MeV
$p + {}^{40}_{42}Ca$
$p + {}^{42}Ca$
$p + {}^{44}Ca$

Fig.22

nature of V_{ex}, which reflects the ℓ-dependence of this potential[51]. It seems that the ℓ-dependent potential increases in importance as the mass number of the target nucleus becomes smaller.

To date all studies, except for a recent study by Vosniakos et al.[52] of ℓ-dependent terms in the optical model potential have been carried out using data at a single incident proton energy. More studies of these ℓ-dependent terms over a wide range of energies and mass numbers are to be encouraged with the hope that understandable systematic features of V_{ex} will be revealed.

IV.4 Extraction of the Nuclear Matter Radii

The average values of the m.s. radii for the real central potential, $< r_{op}^2 >$, are calculated from Tables 10, 11 and 12. These averages are 17.01 ± 0.16, 17.31 ± 0.15 and 17.54 ± 0.23 fm^2 for ^{40}Ca, ^{42}Ca and ^{44}Ca, respectively. The uncertainties in each of these values are due to the following:

a) A statistical error which is calculated according to the formula,

$$\sum_{i=1}^{n} \frac{(< r_{op}^2 >_i - \overline{< r_{op}^2 >})^2}{n(n-1)}$$

where n is the number of measurements made of $< r_{op}^2 >$, $< r_{op}^2 >_i$ is the i^{th} value of $< r_{op}^2 >$ and $\overline{< r_{op}^2 >}$ is the average of the n measurements of $< r_{op}^2 >$.

b) The ambiguity of the optical model in fitting the experimental data. A variation in $< r_{op}^2 >$ by 0.08 fm^2 resulted in a change of approximately 50% in χ^2 from its minimum value. An increase in χ^2 of more than 50% makes the fit noticeably worse than the best fit[23] (see Fig. 23). Therefore the uncertainty in $< r_{op}^2 >$ is taken to be $\pm$ 0.08 fm^2.

c) The uncertainty in the absolute normalization of the measured differential cross sections ($\pm$ 2.5%). This resulted in an uncertainty in $< r_{op}^2 >$ of $\pm$ 0.09 fm^2.

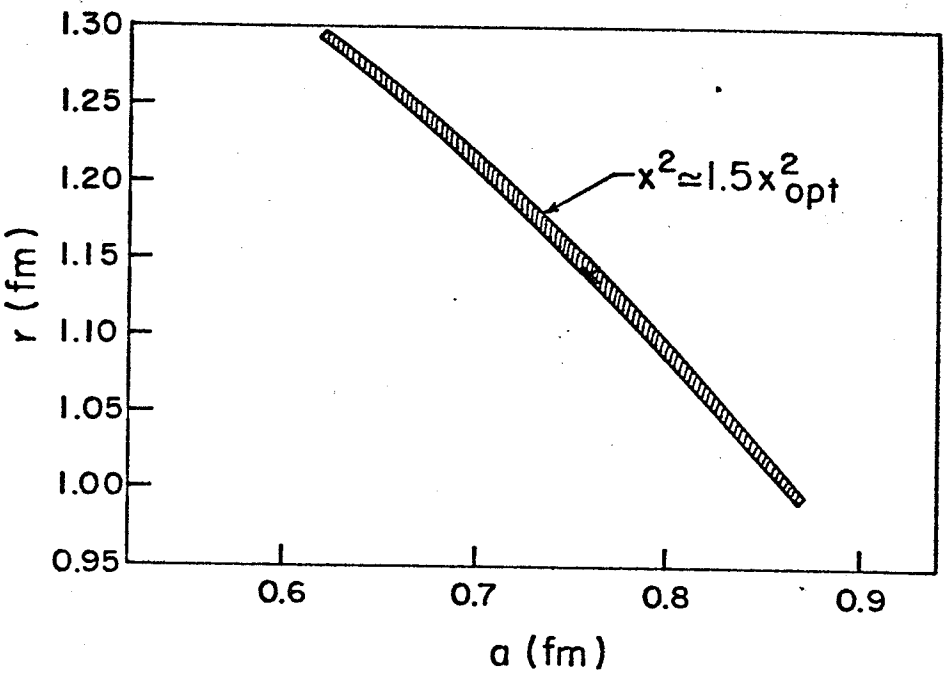

Fig. 23 Contour of constant $x^2 (x^2 \simeq 1.5 x^2_{opt})$ for variations of radius r and diffuseness a of the real central potential. The cross represents the best-fit point. The shaded area encompasses a region within which the fits are visibly indistinguishable.

The error in the calibration of the energy (calibration of the bending magnet) was the same in all measurements for the three isotopes and cancels to first order when differences in the r.m.s. radii are considered. The error in setting or resetting the energy for a particular angular distribution was considered when calculating the relative errors of the measured differential cross sections as discussed in section IV.2 above.

The uncertainty in the zero of the angular scale was found to cancel out, to first order, since left and right measurements were made simultaneously. A deviation between the plane of the target and the axis of rotation of the detector arrays (estimated to be 0.02 degrees at the first minima of the angular distributions) can cause a varying error in the scattering angle. The position of the target along the incident proton beam path was checked. This was done by measuring the differential cross section at a number of angles around 90° lab, then rotating the target by 180° and repeating the measurements at the same angles. The two sets of measurements were found to agree within the statistical errors. The calculations of Appendix 2 show that if there were any errors in the position of the target along the proton beam path (within the limits imposed by the measurements mentioned above) it would not introduce errors of significance in the differences of the r.m.s. radii (see Appendix 2).

All the above uncertainties are added in quadrature to obtain the total uncertainty in $< r_{op}^2 >$.

The average values of $< r_{op}^2 >$ are used in the subsequent calculations. The mass number of each isotope is written to the right hand side of its associated radius for simplicity. For instance, $< r_{op}^2 >_{40}$ is the mean square radius of the real central potential for ^{40}Ca, and so on.

The values of $< r_p^2 >$, the m.s. radius for point proton distributions, are taken from the results of electron scattering experiments[10]. The errors

on $< r_p^2 >$ are $\pm$ 2.0%.

Now from equation (15) of Chapter II one has,

$$< r_{op}^2 > = < r_m^2 > + < r^2 >_{2b} ,$$

where $< r_m^2 >$ is the m.s. radius of the matter distribution and $< r^2 >_{2b}$ is the m.s. radius or range of the nucleon-nucleon interaction. Since the value of $< r^2 >_{2b}$ is uncertain, only relative calculations will be made to obtain $\Delta r_{np} = < r_n^2 >^{1/2} - < r_p^2 >^{1/2}$, the difference between the r.m.s. radii for the neutron and proton distributions, respectively. Relative is used here in the sense that the recent value of Δr_{np} for ^{40}Ca obtained at Los Alamos from the analyses of 0.8 GeV proton scattering data[53] is used to determine Δr_{np} for ^{42}Ca and ^{44}Ca.

From the previous equation, namely

$$< r_{op}^2 > = < r_m^2 > + < r^2 >_{2b}$$

one obtains for the radius difference between ^{40}Ca and ^{42}Ca

$$< r_{op}^2 >_{42} - < r_{op}^2 >_{40} = < r_m^2 >_{42} - < r_m^2 >_{40} \qquad (19)$$

since[53],

$$< r_n^2 >_{40}^{1/2} - < r_p^2 >_{40}^{1/2} = 0.03 \pm 0.05 \text{ fm},$$

$$< r_n^2 >_{40}^{1/2} = 3.42 \pm 0.06$$

but $$< r_m^2 >_{40} = \frac{Z}{A} < r_p^2 >_{40} + \frac{N}{A} < r_n^2 >_{40}$$

or $$< r_m^2 >_{40} = 11.60 \pm 0.23 \text{ fm}^2$$

substituting in equation (19):

$$< r_m^2 >_{42} = 11.90 \pm 0.32 \text{ fm}^2$$

with

$$\langle r_m^2 \rangle_{42} = \frac{Z}{A} \langle r_p^2 \rangle_{42} + \frac{N}{A} \langle r_n^2 \rangle_{42}$$

one obtains:

$$\langle r_n^2 \rangle_{42}^{1/2} = 3.48 \pm 0.09 \text{ fm}$$

Finally one obtains for ^{42}Ca,

$$\Delta r_{np} = 0.06 \pm 0.09 \text{ fm}$$

Similarily,

$$\langle r_{op}^2 \rangle_{44} - \langle r_{op}^2 \rangle_{40} = \langle r_m^2 \rangle_{44} - \langle r_m^2 \rangle_{40}$$

or

$$\langle r_m^2 \rangle_{44} = 12.13 \pm 0.36 \text{ fm}^2,$$

with

$$\langle r_m^2 \rangle_{44} = \frac{Z}{A} \langle r_p^2 \rangle_{44} + \frac{N}{A} \langle r_n^2 \rangle_{44} ,$$

one obtains:

$$\langle r_n^2 \rangle_{44}^{1/2} = 3.53 \pm 0.09 \text{ fm} .$$

Finally, one obtains for ^{44}Ca,

$$\Delta r_{np} = 0.11 \pm 0.09 \text{ fm} .$$

IV.5 Comparison with Previous Measurements and Theoretical Calculations

In Table 15 the present results for Δr_{np} are compared first of all with those obtained from an analysis of the 0.8 GeV proton elastic scattering data obtained at los Alamos[54]. These latter data were analyzed by Igo et al.[54] using the first-order, spin-dependent proton-nucleus optical potential of Kerman, McManus and Thaler (KMT). The ingredients of the first-order optical potential description are the spin-dependent nucleon-nucleon scattering amplitudes and the nuclear matter densities. The parameters of the nucleon-nucleon amplitudes appropriate at 0.8 GeV were determined by fitting nucleon-nucleon elastic scattering data.

The model density assumed for the point-proton and -neutron densities was

$$\rho_i(r) = \rho_{oi}[(1 + w_i\, r^2/R_i^2) \,/\, (1 + \exp\, \frac{r-R_i}{z_i}\,)$$

$$+ s_i \cos\,(m_i\, r - \phi_i)\, \exp(-\, d_i(r - r_{oi})^2)/m_i r]$$

for i = p or n, s_i, m_i, ϕ_i are adjustable parameters to be obtained by fitting the experimental data. The second term is needed in order to reproduce the charge distributions obtained in the analysis of electron scattering data[10]. The point proton densities were kept fixed in the analysis. The point neutron densities and the spin-dependent nucleon-nucleon amplitudes were then determined by simultaneously fitting the elastic scattering differential cross sections and analyzing powers. Only the first term in the above equation was used for the neutron density distribution.

Also shown in Table 15 are the results of different analyses of the 1 GeV proton elastic scattering data[55-57] obtained at Saclay. Alkhazov et al.[56] employed a spin-independent Glauber type analysis to extract neutron and nuclear matter densities of the calcium isotopes. In the analysis nuclear correlations are taken into account. The charge and neutron density distributions are parametrized as parabolic Fermi functions

$$\rho_c(r) = C_c[\, 1 + W_c\, (\frac{r}{R_c})^2\,] \,/\, [\, 1 + \exp\, (\frac{r-R_c}{z_c})\,]$$

$$\rho_n(r) = C_n[\, 1 + W_n\, (\frac{r}{R_n})^2\,] \,/\, [\, 1 + \exp\, (\frac{r-R_n}{z_n})\,]$$

where C_c and C_n are normalization constants. The parameters of the charge distribution, $\rho_c(r)$, are fixed to those obtained from electron scattering experiments[10], while the parameters for the neutron density distributions are obtained from least squares fit to the experimental data. The W_n parameter was kept constant and equal to W_c.

Table 15

Comparison of $\Delta r_{np} = \langle r_n^2 \rangle^{1/2} - \langle r_p^2 \rangle^{1/2}$ (fm)

for ^{40}Ca, ^{42}Ca, ^{44}Ca and ^{48}Ca

Method		0.8 GeV (p,p)	1 GeV (p,p)				16 MeV LEP	(α,α) 1.3 GeV	(α,α) 166 MeV	CE	πA		(π,π)	HF	SM
Ref.	This Work	54	55	55*)	56	57	58	59	60	61	62	63	64†)	54	65
^{40}Ca		0.01▲)	-0.03	0.02	0.01	-0.03	0.01	-0.03	-0.07					-0.05	-0.04
^{42}Ca	0.06	0.08	0.04	0.08	0.05	0.07		0.02		0.01				0.03	
^{44}Ca	0.11	0.10	0.05	0.13	0.09	0.07	-0.02	0.10	0.09	0.02	0.35	0.49	0.13	0.09	0.19
^{48}Ca		0.18	0.16	0.21	0.18	0.17	0.39	0.20	0.33	0.06			0.20	0.19	0.34
Error	0.09	0.08	0.05	0.03	0.03		0.12	0.05	0.12		0.15	0.07	0.08		

*) Analysis includes nuclear correlations.

†) These values result under the assumption that $\Delta r_{np}(^{40}Ca) = 0$.

▲) A more recent value is 0.03 ± 0.05 fm[53].

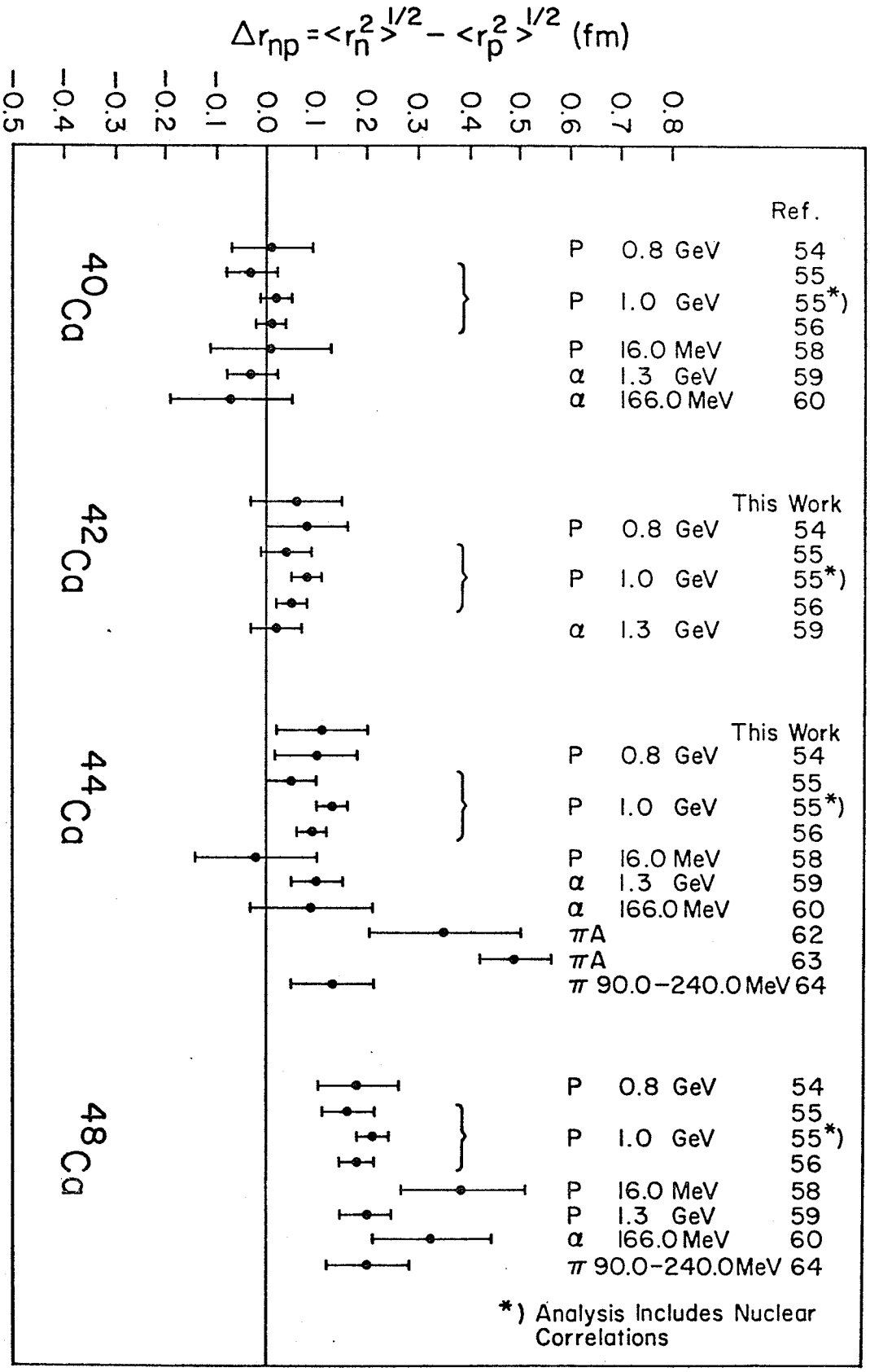

Fig. 24. Comparison of $\Delta r_{np} = \langle r_n^2 \rangle^{1/2} - \langle r_p^2 \rangle^{1/2}$ for ^{40}Ca, ^{42}Ca, ^{44}Ca and ^{48}Ca

In Table 15 a comparison is also presented with the results of analysis of low energy (16 MeV) proton (LEP) elastic scattering data[58], alpha elastic scattering data[59-60], Coulomb displacement energies (CE)[61], pionic atom data (πA)[62-63] and pion total and differential cross section data[64]. Also given in the table are the theoretical predictions of Hartree-Fock (HF)[54] and shell-model (SM)[65] calculations.

On notices in Table 15 that in general there is good agreement between the present results and those obtained in analysis of intermediate energy proton and alpha elastic scattering data. The Coulomb displacement energies yield smaller values while pionic atom data yield larger values than those obtained from hadronic scattering data. The predictions of Hartree-Fock calculations are in satisfactory agreement with the hadronic scattering results whereas the shell-model predictions are too large. These comparisons are also plotted in Fig. 24.

CHAPTER V

DISCUSSION AND CONCLUSIONS

Differential cross sections for protons scattered by ^{40}Ca, ^{42}Ca and ^{44}Ca over a wide range of energies and angles have been measured. An optical model analysis of these data has been carried out and nuclear sizes have been extracted.

The optical model potential used in the analysis of the data gives a good description of the elastic scattering of protons by the calcium isotopes. The introduction of ℓ-dependence into the optical model potential is capable of improving the fits to the experimental data, especially at angles larger than about 120^{o}. The result supports the idea that these ℓ-dependent terms are important in the optical model description of proton elastic scattering.

The present work demonstrates the degree to which accurately measured proton elastic scattering differential cross sections in the low energy region can provide information about differences in nuclear matter radii for an isotopic sequence.

This work also reveals shell effects. The neutron radius increases by adding successive neutron pairs in the $1f_{7/2}$ shell. This behaviour suggests a neutron envelope outside the ^{40}Ca core which expands with mass number.

One can also notice form the optical model analysis that the r.m.s. radii of the real central potential are independent of energy, as expected, and significantly greater than the corresponding proton radii obtained from electromagnetic probes. The results for the volume integral per nucleon of the real central potential suggest a gradual decrease in these integrals with increasing incident energies.

Perhaps more satisfying conclusions might emerge from similar programs of systematic studies of differences in nuclear radii for isotopic sequences which, unfortunately, have not yet received enough attention.

Appendix 1

Tables of Differential Cross Sections

$^{40}Ca(p,p)^{40}Ca$

$T_p = 25.0 \pm 0.2$ MeV

$\theta_{c.m.}$ (degrees)	$(\frac{d\sigma}{d\Omega})_{c.m.}$ (fm^2/sr)	relative error (percent)	$\theta_{c.m.}$ (degrees)	$(\frac{d\sigma}{d\Omega})_{c.m.}$ (fm^2/sr)	relative error (percent)
10.24	1070.	2.9	86.37	1.291	2.6
12.80	486.0	2.7	91.38	1.309	3.5
15.36	279.4	3.2	96.37	1.031	3.4
17.91	176.6	2.4	101.36	0.7854	3.3
20.47	112.1	2.4	106.33	0.5779	3.5
23.03	66.75	2.4	111.30	0.4108	3.4
25.58	35.52	2.5	116.25	0.2800	2.6
28.14	17.45	2.5	121.19	0.2095	2.4
30.69	6.851	2.5	126.13	0.1417	2.8
33.24	2.493	2.6	131.06	0.1281	3.1
35.79	1.975	3.3	135.97	0.1299	3.8
38.34	3.988	3.3	140.89	0.1656	3.3
40.89	6.624	2.6	145.79	0.2030	3.0
43.43	9.141	2.5	150.69	0.2232	2.5
45.98	10.76	2.5	155.58	0.2326	2.6
48.52	11.35	2.4	160.47	0.2308	2.5
51.06	11.27	2.3	165.36	0.2237	2.8
53.59	10.03	2.4	170.24	0.1781	3.0
56.13	8.619	2.7			
58.66	6.823	2.6			
61.19	5.113	2.5			
63.72	3.846	3.3			
66.25	2.474	3.2			
68.77	1.842	3.4			
71.30	1.468	3.1			
73.82	1.065	3.1			
76.33	1.109	2.6			
78.85	1.171	3.1			
81.36	1.242	2.6			

$^{40}Ca(p,p)^{40}Ca$

$T_p = 27.5 \pm 0.2$ MeV

$\theta_{c.m.}$ (degrees)	$(\frac{d\sigma}{d\Omega})_{c.m.}$ (fm^2/sr)	relative error (percent)	$\theta_{c.m.}$ (degrees)	$(\frac{d\sigma}{d\Omega})_{c.m.}$ (fm^2/sr)	relative error (percent)
10.24	897.7	3.1	91.38	0.9839	3.1
12.80	446.5	2.6	96.38	0.6586	3.3
15.36	264.8	2.5	101.36	0.4507	3.5
17.92	175.9	2.4	106.34	0.3181	3.9
20.47	110.9	2.4	111.30	0.2697	3.2
23.03	65.18	2.5	116.25	0.2491	3.4
25.58	32.50	2.4	121.20	0.2096	2.5
28.14	15.60	2.6	126.13	0.1582	2.5
30.69	5.727	2.5	131.06	0.1104	2.8
33.24	2.442	2.5	135.98	0.0884	3.2
35.79	2.886	3.1	140.89	0.0963	3.6
38.34	5.534	3.0	145.79	0.1273	3.6
40.89	8.248	2.5	150.69	0.1656	2.9
43.43	10.17	2.5	155.58	0.1876	2.7
45.98	11.18	2.4	160.47	0.1893	2.7
48.52	11.52	2.4	165.36	0.1765	2.7
51.06	10.60	2.3	170.24	0.1567	3.3
53.60	9.385	2.5			
56.13	7.156	2.5			
58.67	5.743	2.8			
61.20	4.179	2.6			
63.73	2.908	3.1			
66.25	1.796	2.8			
68.78	1.399	3.1			
71.30	1.122	2.9			
73.82	1.180	2.6			
76.34	1.211	2.6			
78.85	1.273	2.5			
81.36	1.317	2.4			
86.38	1.228	2.6			

$^{40}Ca(p,p)^{40}Ca$

$T_p = 30.0 \pm 0.2$ MeV

$\theta_{c.m.}$ (degrees)	$(\frac{d\sigma}{d\Omega})_{c.m.}$ (fm^2/sr)	relative error (percent)	$\theta_{c.m.}$ (degrees)	$(\frac{d\sigma}{d\Omega})_{c.m.}$ (fm^2/sr)	relative error (percent)
10.24	783.2	4.1	91.39	0.7404	3.9
12.80	405.5	3.9	96.38	0.3709	5.3
15.36	254.7	3.6	101.36	0.2555	3.3
17.92	162.1	4.3	106.34	0.1938	3.4
20.47	103.4	3.5	111.30	0.1924	2.7
23.03	58.92	3.9	116.26	0.1987	3.4
25.59	29.99	3.6	121.20	0.1794	2.6
28.14	13.23	4.0	126.14	0.1318	3.1
30.69	4.685	3.5	131.06	0.0793	3.0
33.25	2.939	4.1	135.98	0.0480	6.6
35.80	4.532	3.9	140.89	0.0479	4.0
38.34	6.990	3.9	145.79	0.0733	4.1
40.89	9.750	3.5	150.69	0.1069	3.1
43.44	11.39	3.8	155.59	0.1313	3.4
45.98	11.79	3.6	160.47	0.1398	2.8
48.52	11.48	3.2	165.36	0.1361	3.1
51.06	9.578	2.6	170.24	0.1180	3.3
53.60	7.731	3.2			
56.14	6.096	3.0			
58.67	4.307	3.8			
61.20	2.899	2.9			
63.73	2.029	3.4			
66.26	1.424	2.7			
68.78	1.058	3.6			
71.30	1.047	2.4			
73.82	1.126	2.7			
76.34	1.178	2.5			
78.85	1.187	2.7			
81.37	1.159	2.6			
86.38	1.064	3.3			

$^{40}Ca(p,p)^{40}Ca$

$T_p = 35.0 \pm 0.2$ MeV

$\theta_{c.m.}$ (degrees)	$(\frac{d\sigma}{d\Omega})_{c.m.}$ (fm^2/sr)	relative error (percent)	$\theta_{c.m.}$ (degrees)	$(\frac{d\sigma}{d\Omega})_{c.m.}$ (fm^2/sr)	relative error (percent)
10.24	556.2	3.2	91.39	0.3286	3.3
12.80	342.6	3.1	96.39	0.2015	2.8
15.36	235.4	2.6	101.37	0.1250	2.4
17.92	152.5	2.5	106.35	0.1128	3.0
20.48	95.91	2.4	111.31	0.1119	2.5
23.03	52.55	2.6	116.26	0.1109	4.1
25.59	26.74	2.5	121.21	0.0864	3.0
28.14	10.66	3.0	126.14	0.0521	5.5
30.70	4.786	2.5	131.07	0.0305	2.9
33.25	3.842	2.5	135.98	0.0169	3.1
35.80	5.879	2.4	140.89	0.0183	2.5
38.35	7.785	2.5	145.80	0.0398	2.9
40.90	9.419	2.4	150.70	0.0564	2.5
43.44	9.949	2.5	155.59	0.0683	3.2
45.99	9.959	2.4	160.48	0.0706	2.7
48.53	8.166	2.7	165.36	0.0666	3.7
51.07	6.773	2.4	170.24	0.0402	4.4
53.61	4.741	2.8			
56.14	3.511	2.7			
58.68	2.201	3.1			
61.21	1.505	2.6			
63.74	0.9683	3.0			
66.26	0.8718	2.8			
68.79	0.8500	2.6			
71.31	0.8606	2.5			
73.83	0.8355	3.0			
76.35	0.8252	2.8			
78.86	0.8004	2.9			
81.37	0.7681	2.5			
86.39	0.5608	3.2			

$^{40}Ca(p,p)^{40}Ca$

$T_p = 40.0 \pm 0.2$ MeV

$\theta_{c.m.}$ (degrees)	$(\frac{d\sigma}{d\Omega})_{c.m.}$ (fm^2/sr)	relative error (percent)
10.24	566.5	3.7
12.80	370.9	3.9
15.36	240.7	3.6
17.92	169.1	3.6
20.48	98.33	3.2
23.04	51.61	3.6
25.59	22.90	3.6
28.15	10.14	4.2
30.70	6.550	3.6
33.25	5.980	3.6
35.80	7.180	3.3
38.35	9.770	3.5
40.90	10.34	3.5
43.45	9.740	3.5
45.99	7.730	3.3
48.53	6.252	2.9
51.07	4.481	2.6
53.61	3.158	3.1
56.15	2.128	2.7
58.68	1.314	3.3
61.21	0.9437	2.7
63.74	0.8423	2.5
66.27	0.8356	2.6
68.79	0.8515	2.5
71.32	0.8094	2.4
73.84	0.7759	2.6
76.35	0.6528	2.7
78.87	0.5597	3.6
81.38	0.4335	3.0
86.39	0.2298	3.4
91.40	0.1349	3.2
96.39	0.1050	3.1
101.38	0.0979	2.7
106.35	0.0913	2.6
111.32	0.0684	2.6
116.27	0.0431	4.1
121.21	0.0333	3.7
126.15	0.0235	3.6
131.07	0.0187	2.6
135.99	0.0155	2.7
140.90	0.0167	2.4
145.80	0.0205	3.3
150.70	0.0244	3.2
155.59	0.0279	5.4
160.48	0.0261	4.2
165.36	0.0210	6.5
170.24	0.0114	5.1

$^{40}Ca(p,p)^{40}Ca$

$T_p = 45.0 \pm 0.2$ MeV

$\theta_{c.m.}$ (degrees)	$(\frac{d\sigma}{d\Omega})_{c.m.}$ (fm^2/sr)	relative error (percent)	$\theta_{c.m.}$ (degrees)	$(\frac{d\sigma}{d\Omega})_{c.m.}$ (fm^2/sr)	relative error (percent)
10.24	455.6	2.6	86.40	0.1117	3.2
12.80	296.3	2.5	91.41	0.0976	2.4
15.36	218.0	2.9	96.40	0.0872	2.4
17.92	134.7	2.5	101.39	0.0749	2.6
20.48	85.20	2.4	106.36	0.0514	2.8
23.04	39.74	2.5	111.32	0.0298	3.8
25.60	20.03	2.5	116.27	0.0186	3.1
28.15	7.529	2.8	121.22	0.0143	2.9
30.70	5.244	2.6	126.15	0.0146	2.7
33.26	6.167	2.7	131.08	0.0148	2.6
35.81	7.779	2.4	135.99	0.0121	3.1
38.36	8.451	2.4	140.90	0.0098	3.0
40.90	8.948	2.4	145.81	0.0074	4.3
43.45	7.880	2.5	150.70	0.0073	4.0
46.00	6.327	2.3	155.59	0.0075	4.1
48.54	4.216	2.5	160.48	0.0073	4.2
51.08	3.023	2.4	165.36	0.0059	3.7
53.62	1.739	2.7	170.24	0.0035	5.9
56.15	1.213	2.5			
58.69	0.8029	2.6			
61.22	0.7808	2.4			
63.75	0.7552	2.5			
66.28	0.7232	2.5			
68.80	0.7088	2.5			
71.32	0.6156	2.5			
73.84	0.4864	2.7			
76.36	0.4010	2.5			
78.87	0.2889	3.0			
81.39	0.2305	2.6			

$^{42}Ca(p,p)^{42}Ca$

$T_p = 21.0 \pm 0.2$ MeV

$\theta_{c.m.}$ (degrees)	$(\frac{d\sigma}{d\Omega})_{c.m.}$ (fm^2/sr)	relative error (percent)	$\theta_{c.m.}$ (degrees)	$(\frac{d\sigma}{d\Omega})_{c.m.}$ (fm^2/sr)	relative error (percent)
10.23	1523.	4.3	91.31	1.243	3.9
12.78	610.2	4.1	96.30	1.267	4.0
15.34	314.9	3.6	101.29	1.026	3.9
17.89	187.1	3.6	106.26	0.7537	4.1
20.45	116.2	3.6	111.23	0.4033	3.8
23.00	70.42	3.6	116.19	0.2530	3.9
25.55	41.93	3.7	121.13	0.1433	3.8
28.10	22.33	3.8	126.07	0.1132	3.8
30.65	10.94	4.0	131.00	0.1317	3.9
33.20	4.668	4.5	135.93	0.1631	3.8
35.75	2.429	3.7	140.84	0.2213	3.8
38.30	3.405	3.8	145.75	0.2538	4.0
40.84	4.957	3.8	150.65	0.2558	3.8
43.38	6.489	4.2	155.55	0.2406	3.8
45.93	7.761	3.9	160.45	0.2372	3.8
48.47	8.498	4.0	165.34	0.2400	3.8
51.00	8.648	3.7	170.23	0.2545	4.0
53.54	8.434	3.6			
56.07	7.400	3.6			
58.60	6.483	3.7			
61.13	4.936	3.6			
63.66	3.761	3.8			
66.19	2.329	3.8			
68.71	1.561	3.8			
71.23	1.075	3.9			
73.75	0.7735	3.8			
76.26	0.5626	5.5			
78.78	0.6386	4.7			
81.29	0.7854	4.2			
86.30	1.043	4.0			

$^{42}Ca(p,p)^{42}Ca$

$T_p = 25.0 \pm 0.2$ MeV

$\theta_{c.m.}$ (degrees)	$(\frac{d\sigma}{d\Omega})_{c.m.}$ (fm^2/sr)	relative error (percent)	$\theta_{c.m.}$ (degrees)	$(\frac{d\sigma}{d\Omega})_{c.m.}$ (fm^2/sr)	relative error (percent)
10.23	1094.	4.5	91.31	1.102	3.8
12.78	499.8	3.8	96.31	0.7675	4.3
15.34	287.6	3.7	101.29	0.5021	4.0
17.90	178.3	3.7	106.27	0.3009	4.6
20.45	110.9	3.6	111.23	0.2051	3.8
23.00	64.60	3.7	116.19	0.1564	3.9
25.56	34.03	3.7	121.14	0.1264	3.7
28.11	15.24	3.9	126.08	0.1022	3.7
30.66	5.463	4.1	131.01	0.0998	3.8
33.21	1.803	4.7	135.93	0.1045	4.0
35.75	2.244	4.1	140.84	0.1235	3.9
38.30	4.470	3.8	145.75	0.1287	4.1
40.85	7.267	3.6	150.66	0.1323	3.9
43.39	9.786	3.8	155.56	0.1357	4.0
45.93	10.40	3.6	160.45	0.1360	3.8
48.47	10.59	3.6	165.34	0.1379	4.0
51.01	10.24	3.6	170.23	0.1460	4.0
53.54	8.621	3.7			
56.08	6.744	3.7			
58.61	5.185	3.8			
61.14	3.752	3.7			
63.67	2.532	4.0			
66.19	1.560	3.9			
68.71	1.089	3.9			
71.24	0.8566	3.7			
73.75	0.8298	4.1			
76.27	0.9341	3.9			
78.78	1.071	4.0			
81.29	1.193	3.6			
86.31	1.293	3.7			

$^{42}Ca(p,p)^{42}Ca$

$T_p = 30.0 \pm 0.2$ MeV

$\theta_{c.m.}$ (degrees)	$(\frac{d\sigma}{d\Omega})_{c.m.}$ (fm^2/sr)	relative error (percent)
10.23	718.2	3.8
12.79	384.8	3.7
15.34	244.8	3.6
17.90	155.2	3.7
20.45	93.53	3.6
23.01	52.23	3.7
25.56	25.38	3.7
28.11	9.765	3.8
30.66	3.102	3.7
33.21	2.005	4.3
35.76	4.107	4.5
38.30	6.904	4.0
40.85	9.042	3.6
43.39	10.32	3.6
45.93	10.58	3.6
48.47	9.553	3.6
51.01	7.989	3.7
53.55	6.116	3.8
56.08	4.333	3.7
58.61	2.710	4.1
61.14	1.774	3.9
63.67	1.132	4.2
66.20	0.8423	3.9
68.72	0.7695	3.8
71.24	0.8042	3.9
73.76	0.9585	3.8
76.28	1.035	3.7
78.79	1.047	4.1
81.30	1.048	3.8
86.32	0.8498	3.9
91.32	0.6052	4.3
96.32	0.2976	4.2
101.30	0.1855	3.9
106.28	0.1372	3.7
111.24	0.1481	3.6
116.20	0.1517	3.7
121.14	0.1406	3.7
126.08	0.1017	3.7
131.01	0.0648	3.9
135.93	0.0372	4.4
140.85	0.0320	4.5
145.76	0.0470	4.0
150.66	0.0702	3.7
155.56	0.0853	3.7
160.45	0.0902	3.7
165.34	0.0842	3.8
170.23	0.0792	4.0

$^{42}Ca(p,p)^{42}Ca$

$T_p = 35.0 \pm 0.2$ MeV

$\theta_{c.m.}$ (degrees)	$(\frac{d\sigma}{d\Omega})_{c.m.}$ (fm^2/sr)	relative error (percent)	$\theta_{c.m.}$ (degrees)	$(\frac{d\sigma}{d\Omega})_{c.m.}$ (fm^2/sr)	relative error (percent)
10.23	645.9	3.8	86.32	0.4354	4.0
12.79	383.5	3.8	91.33	0.2470	4.4
15.34	255.9	3.6	96.32	0.1342	3.7
17.90	164.2	3.6	101.31	0.1244	3.6
20.45	97.78	3.6	106.28	0.1164	3.7
23.01	51.30	3.7	111.25	0.1099	3.8
25.56	22.91	3.7	116.20	0.0882	4.1
28.11	8.616	3.7	121.15	0.0659	4.3
30.66	3.724	3.7	126.09	0.0430	5.1
33.21	4.084	4.0	131.02	0.0258	4.1
35.76	6.651	3.8	135.94	0.0175	3.9
38.31	9.461	3.7	140.85	0.0195	3.7
40.85	11.03	3.6	145.76	0.0286	3.8
43.40	11.25	3.6	150.66	0.0393	3.9
45.94	9.951	3.6	155.56	0.0449	4.0
48.48	8.253	3.7	160.45	0.0433	3.9
51.02	6.312	3.7	165.34	0.0326	4.7
53.55	4.205	3.8	170.23	0.0211	5.7
56.09	2.654	3.7			
58.62	1.798	4.1			
61.15	1.089	3.7			
63.68	0.8602	4.0			
66.20	0.7971	3.7			
68.73	0.8962	4.0			
71.25	0.9367	3.6			
73.77	0.9727	3.8			
76.28	0.9478	3.7			
78.80	0.8429	3.9			
81.31	0.7173	3.7			

$^{42}Ca(p,p)^{42}Ca$

$T_p = 40.0 \pm 0.2$ MeV

$\theta_{c.m.}$ (degrees)	$(\frac{d\sigma}{d\Omega})_{c.m.}$ (fm^2/sr)	relative error (percent)	$\theta_{c.m.}$ (degrees)	$(\frac{d\sigma}{d\Omega})_{c.m.}$ (fm^2/sr)	relative error (percent)
10.23	564.5	4.1	96.33	0.1109	3.7
12.79	378.8	3.7	101.31	0.0971	3.7
15.35	257.6	3.6	106.29	0.0790	4.6
17.90	162.6	3.6	111.25	0.0499	4.1
20.46	92.69	3.6	116.21	0.0318	5.1
23.01	46.68	3.7	121.15	0.0227	4.0
25.56	19.94	3.7	126.09	0.0173	4.1
28.12	7.702	3.8	131.02	0.0162	3.7
30.67	4.294	3.6	135.94	0.0173	4.2
33.22	5.897	3.7	140.86	0.0144	4.0
35.77	8.323	3.6	145.76	0.0136	4.5
38.31	10.45	3.7	150.67	0.0147	4.3
40.86	10.69	3.6	155.56	0.0157	4.9
43.40	9.747	3.8	160.46	0.0153	4.1
45.94	7.855	3.7	165.34	0.0117	4.7
48.48	5.907	3.8	170.23	0.0070	4.4
51.02	3.774	3.7			
53.56	2.427	4.0			
56.09	1.406	3.9			
58.63	0.9743	4.1			
61.16	0.7677	3.6			
63.68	0.7866	3.7			
66.21	0.8102	3.7			
68.73	0.8422	3.7			
71.25	0.8164	3.6			
73.77	0.7010	4.3			
76.29	0.6171	3.9			
78.80	0.5103	4.7			
81.31	0.3647	3.9			
86.33	0.1996	5.2			
91.33	0.1286	3.9			

$^{42}Ca(p,p)^{42}Ca$

$T_p = 45.0 \pm 0.2$ MeV

$\theta_{c.m.}$ (degrees)	$(\frac{d\sigma}{d\Omega})_{c.m.}$ (fm^2/sr)	relative error (percent)	$\theta_{c.m.}$ (degrees)	$(\frac{d\sigma}{d\Omega})_{c.m.}$ (fm^2/sr)	relative error (percent)
10.23	449.6	6.2	96.34	0.0864	4.5
12.79	320.2	5.4	101.32	0.0623	3.8
15.35	220.6	4.6	106.29	0.0431	4.4
17.90	148.4	4.7	111.26	0.0233	3.9
20.46	76.94	4.3	116.21	0.0143	4.2
23.01	35.41	4.3	121.16	0.0120	3.8
25.57	11.66	4.1	126.10	0.0128	4.1
28.12	5.205	4.2	131.03	0.0123	3.8
30.67	4.146	3.8	135.95	0.0101	4.4
33.22	5.285	4.2	140.86	0.0067	4.1
35.77	7.319	3.9	145.77	0.0045	5.1
38.32	8.862	4.2	150.67	0.0036	4.6
40.86	8.867	3.6	155.57	0.0042	5.4
43.41	7.867	3.7	160.46	0.0045	4.7
45.95	5.155	3.7	165.35	0.0041	6.3
48.49	3.604	3.8	170.23	0.0025	6.9
51.03	2.220	3.7			
53.56	1.419	4.4			
56.10	0.8725	3.7			
58.63	0.7194	4.1			
61.16	0.7131	3.7			
63.69	0.7410	3.8			
66.22	0.7113	3.7			
68.74	0.6643	4.0			
71.26	0.5596	3.7			
73.78	0.4550	3.9			
76.30	0.3279	4.0			
78.81	0.2363	4.3			
81.32	0.1653	4.2			
86.34	0.0872	5.2			
91.34	0.0897	4.2			

$^{42}Ca(p,p)^{42}Ca$

$T_p = 48.4 \pm 0.2$ MeV

$\theta_{c.m.}$ (degrees)	$(\frac{d\sigma}{d\Omega})_{c.m.}$ (fm^2/sr)	relative error (percent)	$\theta_{c.m.}$ (degrees)	$(\frac{d\sigma}{d\Omega})_{c.m.}$ (fm^2/sr)	relative error (percent)
10.23	344.6	5.5	91.34	0.0743	4.3
12.79	261.4	5.6	96.34	0.0546	4.5
15.35	187.4	4.9	101.32	0.0394	3.9
17.90	122.3	5.8	106.30	0.0213	5.4
20.46	68.80	4.1	111.26	0.0126	4.7
23.02	30.40	4.7	116.22	0.0090	4.3
25.57	10.00	4.2	121.16	0.0089	3.8
28.12	4.447	4.6	126.10	0.0089	4.2
30.67	3.404	4.0	131.03	0.0076	4.1
33.22	4.644	4.6	135.95	0.0054	4.9
35.77	5.987	4.3	140.86	0.0033	4.9
38.32	7.567	4.6	145.77	0.0016	7.4
40.87	7.576	3.8	150.67	0.0013	6.7
43.41	6.959	3.6	155.57	0.0015	6.8
45.95	4.293	3.6	160.46	0.0021	5.6
48.49	2.999	3.8	165.35	0.0020	6.4
51.03	1.598	3.7	170.23	0.0015	5.3
53.57	0.8663	5.2			
56.10	0.7531	3.8			
58.63	0.6638	3.8			
61.17	0.6668	3.7			
63.69	0.6521	3.7			
66.22	0.6078	3.8			
68.74	0.5209	3.9			
71.26	0.4073	3.7			
73.78	0.3103	4.2			
76.30	0.2108	4.1			
78.81	0.1474	4.3			
81.32	0.0914	4.6			
86.34	0.0808	4.1			

$^{44}Ca(p,p)^{44}Ca$

$T_p = 21.0 \pm 0.2$ MeV

θ c.m. (degrees)	$(\frac{d\sigma}{d\Omega})$ c.m. (fm^2/sr)	relative error (percent)	θ c.m. (degrees)	$(\frac{d\sigma}{d\Omega})$ c.m. (fm^2/sr)	relative error (percent)
10.22	1479.	3.6	91.25	1.203	3.0
12.77	604.6	3.2	96.24	1.033	3.4
15.32	313.9	2.8	101.23	0.8230	3.4
17.88	188.1	2.9	106.21	0.5141	3.4
20.43	111.2	2.8	111.17	0.2838	3.2
22.98	65.12	2.9	116.13	0.1734	3.0
25.53	37.59	2.9	121.08	0.1233	3.0
28.08	21.27	3.1	126.02	0.1186	3.2
30.63	11.48	3.1	130.96	0.1479	2.9
33.17	6.445	4.0	135.88	0.1924	3.2
35.72	4.349	3.0	140.80	0.2148	3.1
38.26	4.760	2.9	145.72	0.2218	3.2
40.80	6.025	2.9	150.62	0.2169	3.1
43.34	7.567	3.1	155.53	0.2026	3.2
45.88	8.684	2.9	160.43	0.1706	3.0
48.42	9.376	2.9	165.32	0.1499	3.1
50.96	9.068	2.8	170.22	0.0960	4.0
53.49	8.058	2.9			
56.02	6.790	2.8			
58.55	5.463	3.0			
61.08	4.084	2.9			
63.61	2.838	3.2			
66.13	1.862	3.2			
68.65	1.116	3.3			
71.17	0.7270	3.0			
73.69	0.5463	4.4			
76.21	0.5699	5.3			
78.72	0.6892	4.9			
81.23	0.7772	3.5			
86.24	1.113	3.1			

$^{44}Ca(p,p)^{44}Ca$

$T_p = 25.0 \pm 0.2$ MeV

$\theta_{c.m.}$ (degrees)	$(\frac{d\sigma}{d\Omega})_{c.m.}$ (fm^2/sr)	relative error (percent)
10.22	1066.	3.5
12.77	488.0	3.0
15.32	276.5	2.8
17.88	173.2	2.9
20.43	101.0	2.8
22.98	61.50	2.9
25.53	31.92	3.0
28.08	14.78	3.8
30.63	5.320	3.4
33.17	2.459	4.2
35.72	3.081	2.8
38.26	5.116	3.1
40.81	7.932	2.9
43.35	9.998	2.9
45.89	10.74	2.8
48.43	10.81	2.9
50.96	9.450	2.8
53.50	7.732	2.9
56.03	5.805	2.9
58.56	4.234	3.1
61.09	2.854	3.0
63.61	1.756	3.5
66.14	1.124	3.2
71.18	0.7007	3.0
73.70	0.8332	3.6
76.21	0.9646	3.6
78.73	1.112	3.5
81.24	1.226	3.0
86.25	1.197	3.0
91.25	1.025	3.7
96.25	0.6281	3.3
101.24	0.3657	4.0
106.21	0.2246	4.3
111.18	0.1515	3.3
116.14	0.1475	3.1
121.09	0.1563	3.0
126.03	0.1540	3.1
130.96	0.1424	2.9
135.89	0.1235	3.3
140.81	0.1113	3.4
145.72	0.1102	3.6
150.63	0.1094	3.1
155.53	0.1125	3.1
160.43	0.1212	3.0
165.32	0.1263	3.2
170.22	0.1425	3.2

$^{44}Ca(p,p)^{44}Ca$

$T_p = 30.0 \pm 0.2$ MeV

$\theta_{c.m.}$ (degrees)	$(\frac{d\sigma}{d\Omega})_{c.m.}$ (fm^2/sr)	relative error (percent)	$\theta_{c.m.}$ (degrees)	$(\frac{d\sigma}{d\Omega})_{c.m.}$ (fm^2/sr)	relative error (percent)
10.22	759.1	3.0	91.26	0.4383	4.5
12.77	418.4	3.0	96.26	0.2562	4.1
15.33	254.2	2.8	101.24	0.1585	3.1
17.88	162.3	2.9	106.22	0.1446	2.9
20.43	93.60	2.8	111.18	0.1538	2.9
22.98	52.49	2.9	116.14	0.1566	2.9
25.53	22.99	2.9	121.09	0.1421	2.9
28.08	8.258	3.2	126.03	0.1002	3.4
30.63	2.972	2.8	130.97	0.0624	3.4
33.18	2.918	3.5	135.89	0.0353	4.6
35.72	5.154	3.1	140.81	0.0303	3.6
38.27	8.356	3.1	145.72	0.0430	3.3
40.81	10.70	2.8	150.63	0.0601	3.0
43.35	11.65	2.8	155.53	0.0743	3.0
45.89	11.47	2.9	160.43	0.0806	3.0
48.43	10.21	3.0	165.33	0.0751	3.7
50.97	7.906	2.8	170.22	0.0600	6.5
53.50	5.852	3.1			
56.03	3.902	3.0			
58.56	2.499	3.4			
61.09	1.556	3.1			
63.62	1.021	3.1			
66.14	0.8434	2.9			
68.67	0.8322	3.0			
71.19	0.9398	3.0			
73.70	1.065	3.1			
76.22	1.128	3.3			
78.73	1.155	3.2			
81.24	0.9998	3.1			
86.26	0.7049	3.4			

$^{44}Ca(p,p)^{44}Ca$

$T_p = 35.0 \pm 0.2$ MeV

$\theta_{c.m.}$ (degrees)	$(\frac{d\sigma}{d\Omega})_{c.m.}$ (fm^2/sr)	relative error (percent)	$\theta_{c.m.}$ (degrees)	$(\frac{d\sigma}{d\Omega})_{c.m.}$ (fm^2/sr)	relative error (percent)
10.22	663.8	3.0	81.25	0.6592	3.9
12.77	402.2	2.9	86.26	0.3766	4.2
15.33	261.6	2.9	91.27	0.1765	3.4
17.88	163.7	2.9	96.26	0.1331	3.1
20.43	93.82	2.8	101.25	0.1384	2.8
22.99	48.57	2.9	106.22	0.1335	3.0
25.54	20.20	2.9	111.19	0.1124	3.1
28.09	7.327	3.0	116.15	0.0819	4.0
30.63	3.538	2.9	121.10	0.0602	3.7
33.18	4.867	3.2	126.04	0.0411	4.0
35.73	7.728	2.9	130.97	0.0277	3.0
38.27	10.52	2.9	135.90	0.0226	3.0
40.81	11.72	2.8	140.81	0.0224	2.9
43.36	11.53	2.9	145.73	0.0274	3.0
45.90	9.896	2.8	150.63	0.0332	3.1
48.43	7.937	3.0	155.54	0.0364	3.7
50.97	5.522	2.9	160.43	0.0353	3.4
53.51	3.711	3.2	165.33	0.0279	5.9
56.04	2.257	3.1	170.22	0.0182	5.8
58.57	1.357	3.3			
61.10	0.9484	3.0			
63.62	0.8546	3.0			
66.15	0.8777	3.1			
68.67	0.9561	3.3			
71.19	1.008	3.0			
73.71	1.021	3.2			
76.22	0.9619	3.3			
78.74	0.8143	4.0			

$^{44}Ca(p,p)^{44}Ca$

$T_p = 40.0 \pm 0.2$ MeV

$\theta_{c.m.}$ (degrees)	$(\frac{d\sigma}{d\Omega})_{c.m.}$ (fm^2/sr)	relative error (percent)	$\theta_{c.m.}$ (degrees)	$(\frac{d\sigma}{d\Omega})_{c.m.}$ (fm^2/sr)	relative error (percent)
10.22	596.6	3.0	96.27	0.1143	3.1
12.78	387.5	3.0	101.25	0.1116	2.9
15.33	258.6	2.9	106.23	0.0832	3.3
17.88	160.3	2.9	111.20	0.0562	3.3
20.44	88.80	2.8	116.15	0.0341	3.9
22.99	43.39	2.9	121.10	0.0231	3.2
25.54	17.16	2.9	126.04	0.0211	3.1
28.09	6.628	3.0	130.97	0.0201	2.9
30.64	4.569	2.8	135.90	0.0185	3.1
33.18	6.724	2.9	140.82	0.0150	3.1
35.73	9.283	2.8	145.73	0.0123	3.7
38.28	10.96	2.9	150.64	0.0117	3.6
40.82	11.06	2.8	155.54	0.0126	4.1
43.36	9.934	2.9	160.44	0.0125	3.6
45.90	7.768	2.9	165.33	0.0106	4.1
48.44	5.487	3.1	170.22	0.0068	5.4
50.98	3.496	2.9			
53.51	2.133	3.4			
56.04	1.244	3.1			
58.57	0.9212	3.1			
61.10	0.8318	2.9			
63.63	0.8616	3.0			
66.15	0.8987	2.9			
68.68	0.9000	3.0			
71.20	0.8755	3.0			
73.71	0.7833	3.6			
76.23	0.6267	4.1			
78.74	0.4467	4.4			
81.25	0.3259	4.3			
86.27	0.1832	5.1			
91.27	0.1320	3.5			

$^{44}Ca(p,p)^{44}Ca$

$T_p = 45.0 \pm 0.2$ MeV

$\theta_{c.m.}$ (degrees)	$(\frac{d\sigma}{d\Omega})_{c.m.}$ (fm^2/sr)	relative error (percent)	$\theta_{c.m.}$ (degrees)	$(\frac{d\sigma}{d\Omega})_{c.m.}$ (fm^2/sr)	relative error (percent)
10.22	472.1	4.1	91.28	0.0818	3.3
12.78	334.0	8.4	96.27	0.0802	3.9
15.33	237.0	2.9	101.26	0.0657	3.2
17.89	142.7	3.1	106.24	0.0409	3.5
20.44	77.20	2.8	111.20	0.0222	3.4
22.99	39.10	3.2	116.16	0.0144	3.5
25.54	13.66	2.9	121.11	0.0131	3.0
28.09	5.753	2.9	126.05	0.0134	3.4
30.64	5.375	2.8	130.98	0.0134	3.4
33.19	7.713	2.9	135.90	0.0098	3.6
35.73	9.617	2.8	140.82	0.0070	3.4
38.28	10.53	2.9	145.73	0.0041	4.1
40.82	9.429	2.8	150.64	0.0031	3.9
43.37	7.640	3.0	155.54	0.0038	4.2
45.91	5.253	2.9	160.44	0.0046	3.8
48.44	3.426	3.2	165.33	0.0048	5.2
50.98	1.988	3.0	170.22	0.0032	4.6
53.52	1.207	3.2			
56.05	0.8123	2.9			
58.58	0.7404	2.9			
61.11	0.7842	2.9			
63.64	0.7886	2.9			
66.16	0.7808	3.0			
68.68	0.6883	3.0			
71.20	0.5771	3.3			
73.72	0.4423	4.0			
76.24	0.3237	3.4			
78.75	0.2383	3.5			
81.26	0.1447	3.3			
86.27	0.0974	3.6			

$^{44}Ca(p,p)^{44}Ca$

$T_p = 48.4 \pm 0.2$ MeV

$\theta_{c.m.}$ (degrees)	$(\frac{d\sigma}{d\Omega})_{c.m.}$ (fm^2/sr)	relative error (percent)	$\theta_{c.m.}$ (degrees)	$(\frac{d\sigma}{d\Omega})_{c.m.}$ (fm^2/sr)	relative error (percent)
10.22	446.7	2.9	91.28	0.0494	4.9
12.78	305.7	4.3	96.28	0.0429	6.4
15.33	212.0	2.9	101.26	0.0390	3.5
17.89	124.6	3.0	106.24	0.0219	4.5
20.44	68.85	2.8	111.21	0.0130	3.3
22.99	31.18	3.2	116.16	0.0108	3.0
25.54	11.19	2.9	121.11	0.0102	3.0
28.09	5.254	2.9	126.05	0.0093	3.3
30.64	5.648	2.8	130.98	0.0078	3.3
33.19	8.102	2.9	135.91	0.0052	3.7
35.74	9.426	2.8	140.82	0.0033	4.0
38.28	9.425	2.9	145.74	0.0018	5.6
40.83	8.208	2.8	150.64	0.0015	4.3
43.37	6.158	3.0	155.54	0.0019	4.6
45.91	4.093	3.0	160.44	0.0024	3.9
48.45	2.435	3.3	165.33	0.0024	7.2
50.98	1.390	3.0	170.22	0.0021	4.4
53.52	0.9046	3.4			
56.05	0.6995	2.9			
58.58	0.6951	3.0			
61.11	0.7063	2.9			
63.64	0.7096	2.9			
66.16	0.6310	3.1			
68.69	0.5334	3.1			
71.21	0.4207	3.2			
73.72	0.3043	3.4			
76.24	0.2144	3.8			
78.75	0.1558	4.6			
81.26	0.1126	3.9			
86.28	0.0640	5.4			

Appendix 2

The diffraction minima in the angular distributions occur at

$$\sin\theta = \frac{(n+\frac{1}{2})\lambda}{2r} \quad .$$

For isotope one we have

$$r_1 = \frac{(n+\frac{1}{2})\lambda}{2\sin\theta_1} \quad ;$$

similarly, for isotope two

$$r_2 = \frac{(n+\frac{1}{2})\lambda}{2\sin\theta_2}$$

$$r_1 - r_2 = \frac{(n+\frac{1}{2})\lambda}{2}\left[\frac{1}{\sin\theta_1} - \frac{1}{\sin\theta_2}\right]$$

$$\delta(r_1 - r_2) = \frac{(n+\frac{1}{2})\lambda}{2}\left[\left(\frac{-\cos\theta_1\,\delta\theta_1}{\sin^2\theta_1}\right)^2 + \left(\frac{\cos\theta_2\,\delta\theta_2}{\sin^2\theta_2}\right)^2\right]^{\frac{1}{2}} ,$$

or

$$\frac{\delta(r_1 - r_2)}{r_1} = \left[(-\cot\theta_1\,\delta\theta_1)^2 + \left(\frac{\sin\theta_1\cos\theta_2\,\delta\theta_2}{\sin^2\theta_2}\right)^2\right]^{\frac{1}{2}} ,$$

or

$$\delta(r_1 - r_2) = \left[(-r_1\cot\theta_1\,\delta\theta_1)^2 + \left(r_1\,\frac{\sin\theta_1\cos\theta_2\,\delta\theta_2}{\sin^2\theta_2}\right)^2\right]^{\frac{1}{2}} ,$$

where $\delta\theta_1$ and $\delta\theta_2$ is the uncertainty in setting the target along the proton beam path for isotope one and two, respectively.

Let us substitute numbers in the above formula r_1 and θ_1 are about 4.12 fm and 30.0°, respectively for ^{40}Ca while r_2 and θ_2 are about 4.16 fm and 30.32°, respectively for ^{42}Ca.

If we take $\delta\theta_1 = \delta\theta_2 = 0.02^\circ$, we obtain $\delta(r_1 - r_2) \simeq 0.003$ fm which is a negligible quantity.

References

1. E. Guth, Anz. Akad. Wiss. Wien, 24, 299 (1934).
2. E.M. Lyman, A.O. Hanson and M.B. Scott, Phys. Rev. 84, 626 (1951).
3. V.L. Fitch and Rainwater, Phys. Rev. 92, 782 (1953).
4. R.J. Glauber, in Lectures in Theoretical Physics, edited by W.E. Brittin and L.G. Dunham (Interscience, New York, 1959), Vol. I, p.315.
5. A.K. Kerman, H. McManus and R.M. Thaler, Ann. Phys. (N.Y.) 8, 551 (1959).
6. W.T.H. van Oers, Private Communication; K.H. Bray, K.S. Jayaraman, G.A. Moss, W.T.H. van Oers, D.O. Wells and Y.I. Wu, Nucl. Phys. A167, 57 (1971).
7. Los Alamos Scientific Laboratory, Progress Report LA-7607-PR.
8. E. Friedman, H.J. Gils, H. Rebel and Z. Majka, Phys. Rev. Lett. 41, 1220 (1978).
9. L.R.B. Elton, Nuclear Sizes, Oxford University Press (1961), p.11.
10. R.F. Frosch, R. Hofstadter, J.S. McCarthy, G.K. Nöldeke, K.J. Van Oostrum, M.R. Yearian, B.C. Clark, R. Herman and D.G. Ravenhall, Phys. Rev. 174, 1380 (1968).
11. T. Coffin, R.L. Garwin, S. Penman, L.M. Ledermann and A.M. Sacks, Phys. Rev. 109, 973 (1958).
12. J.A. Wheeler, Revs. Mod. Phys. 21, 133 (1949).
13. H.D. Wohlfahrt, E.B. Shera, M.V. Hoehn, Y. Yamazaki, G. Fricke and R.M. Steffen, Phys. Lett. 73B, 131 (1978).
14. D.C. Peaslee, Phys. Rev. 95, 717 (1954).
15. J.A. Nolen Jr., J.P. Schiffer and Williams, Phys. Lett. 27B, 1 (1968).
16. R.R. Roy and B.P. Nigam, Nuclear Physics, (Wiley, New York, 1967), p.10.
17. I. Kaplan, Phys. Rev. 81, 962 (1951).
18. H. Feshbach, C.E. Porter and V.F. Weisskoff, Phys. Rev. 96, 488 (1954).
19. R.D. Woods and D.S. Saxon, Phys. Rev. 95, 577 (1954).

20. R.S. Mackintosh and A.M. Kobos, Phys. Lett. 62B, 127 (1976).

21. R.S. Mackintosh and L.A. Cordero, Phys. Lett. 68B, 213 (1977).

22. L.G. Votta, P.G. Roos, N.S. Chant and R. Woody, Phys. Rev. C10, 520 (1974).

23. G.W. Greenlees, G.J. Pyle and Y.C. Tang, Phys. Rev. 171, 1115 (1968).

24. V. Hnizdo, O. Karban, J. Lowe, G.W. Greenlees and W. Makofske, Phys. Rev. C3, 1560 (1971).

25. G.W. Greenlees, V. Hnizdo, O. Karban, J. Lowe and W. Makofske, Phys. Rev. C2, 1063 (1970).

26. G.W. Greenlees, W. Makofske and G.J. Pyle, Phys. Lett. 26B, 658 (1968).

27. G.J. Pyle and G.W. Greenlees, Phys. Rev. 181, 1444 (1969).

28. G.W. Greenlees, W. Makofske and G.J. Pyle, Phys. Rev. C1, 1145 (1970).

29. P.B. Woollam, R.J. Griffiths, J.F. Grace and V.E. Lewis, Nucl. Phys. A154, 513 (1970).

30. R.N. Boyd, J. Fenton, M. Williams, T. Kruse and W. Savin, Nucl. Phys. A162, 497 (1971).

31. R.N. Boyd and G.W. Greenlees, Phys. Rev. 176, 1394 (1968); M. Makofske, G.W. Greenlees, H.S. Liers and G.J. Pyle, Phys. Rev. C5, 780 (1972).

32. E.E. Chambers and R. Hofstadter, Phys. Rev. 103, 1454 (1956).

33. R. Smyth, Rev. Sci. Instr. 41, 122 (1966).

34. H. Wilmes, Nucl. Instr. Meth. 41, 122 (1966).

35. A.M. Sourkes, M.S. de Jong, C.A. Goulding, W.T.H. van Oers, E.A. Ginkel, R.F. Carlson, A.J. Cox and D.J. Margaziotis, Nucl. Instr. Meth. 143, 589 (1977).

36. J.A. Fannon, E.J. Burge, D.A. Smith and N.K. Ganguly, Nucl. Phys. A97, 263 (1967).

37. W.T.H. van Oers and J.M. Cameron, Phys. Rev. 184, 1061 (1969).

38. J.L. Snelgrove and E. Kashy, Phys. Rev. 187, 1246 (1969).

39. O. Karban, P.D. Greaves, V. Hnizdo, J. Lowe, N. Berovic and G.W. Greenlees, Nucl. Phys. A132, 548 (1969).

40. Sam M. Austin, E. Kashy, C.H. King, R.G. Markham, I. Redmount and R.M. Ronningen, Phys. Rev. C19, 1186 (1979).

41. B.W. Ridley, University of Colorado, Technical Progress Report, 1966 (unpublished).

42. B.W. Ridley and J.F. Turner, Nucl. Phys. 58, 497 (1964).

43. E.E. Gross, R.H. bassel, L.N. Blumberg, B.J. Morton, A. van der Woude and A. Zucker, Nucl. Phys. A102, 673 (1967).

44. L.N. Blumberg, E.E. Gross, A. van der Woude, A. Zucker and R.H. Bassel, Phys. Rev. 147, 812 (1966).

45. M.A. Melkanoff, J. Raynal and T. Sawada, University of California at Los Angeles Report No. 66-10 (unpublished).

46. E.T. Boschitz, R.W. Bercaw and J.S. Vincent, Phys. Lett. 13, 322 (1964).

47. D.L. Watson, J. Lowe, J.C. Dore, R.M. Craig and D.J. Baugh, Nucl. Phys. A92, 193 (1967).

48. R.M. Craig, J.C. Dore, G.W. Greenlees, J.S. Lilley and J. Lowe, Nucl. Phys. 58, 515 (1964).

49. R.M. Craig, J.C. Dore, J. Lowe and D.L. Watson, Nucl. Phys. 86, 113 (1966).

50. W.T.H. van Oers, Phys. Rev. C3, 1550 (1971).

51. D.R. Thompson, Y.C. Tang and Ronald E. Brown, Phys. Rev. C5, 1939 (1972).

52. F.K. Vosniakos, N.E. Davison, W.R. Falk, O.A. Abou-Zeid and S.P. Kwan, Nucl. Phys. A332, 157 (1979).

53. G.W. Hoffmann, Private Communication.

54. G. Igo, G.S. Adams, T.S. Bauer, G. Pauletta, C.A. Whitten Jr., A. Wreikat, G.W. Hoffmann, G.S. Blanpied, W.R. Coker, C. Harvey, R.P. Liljestrand, L. Ray, J.E. Spencer, H.A. Thiessen, G. Glashausser, N.M. Hintz, M.A. Oothoudt, H. Nann, K.K. Seth, B.E. Wood, D.K. McDaniels and M. Gazzaly, Phys. Lett. 81B, 151 (1979).

55. A. Chaumeaux, V. Layly and R. Schaeffer, Phys. Lett. 72B, 33 (1977).

56. G.D. Alkhazov, T. Bauer, R. Beurtey, A. Boudard, G. Bruge, A. Chaumeaux, P. Couvert, G. Cvijanovich, H.H. Duhm, J.M. Fontaine, D. Garreta, A.V. Kulikov, D. Legrand, J.C. Lugol, J. Saudinos, J. Thirion and A.A. Vorobyov, Nucl. Phys. A274, 443 (1976).

57. L. Ray and W.R. Coker, UTNT-3 University of Texas Technical Report (1977), unpublished.

58. J.C. Lombardi, R.N. Boyd, R. Arking and A.B. Robbins, Nucl. Phys. A188, 103 (1972).

59. G.D. Alkhazov, T. Bauer, R. Bertini, L. Bimbot, O. Oing, A. Boudard, G. Bruge, H. Catz, A. Chaumeaux, P. Couvert, J.M. Fontaine, F. Hibou, G.J. Igo, J.C. Lugol and M. Matoba, Nucl. Phys. A280, 365 (1977).

60. I. Brissaud, Y. Le Bornec, B. Tatischeff, L. Bimbot, M.K. Brussel and G. Duhamel, Nucl. Phys. A191, 145 (1972).

61. J.A. Nolen and J.P. Schiffer, Ann. Rev. Nucl. Sci. 19, 471 (1969).

62. R. Kunselman and G.A. Grin, Phys. Rev. Lett. 24, 838 (1970).

63. L. Tauscher and S. Wycech, Phys. Lett. 62B, 413 (1976).

64. M.J. Jakobson, G.R. Burleson, J.R. Calarco, M.D. Cooper, D.C. Hagerman, I. Halpern, R.H. Jeppeson, K.F. Johnson, L.D. Knutson, R.E. Marrs, H.O. Meyer and R.P. Redwine, Phys. Rev. Lett. 38, 1201 (1977).

65. L.R.B. Elton, Phys. Rev. 158, 970 (1967).